DISS. ETH NO. 24751

Resistive Multiplexed Micromegas Detectors to Search for Dark Sector Physics and Test the Weak Equivalence Principle for Anti-Matter at CERN

A thesis submitted to attain the degree of

DOCTOR OF SCIENCES of ETH ZURICH

(Dr. sc. ETH Zurich)

presented by

Dipanwita Banerjee

M.Sc in Physics, University of Sussex

born on 21.11.1989

citizen of

INDIA

accepted on the recommendation of

Supervisor: A. Rubbia
Co-Supervisor: P. Crivelli, G. Dissertori

2017

I would like to dedicate this thesis to my late grandfather who would have been extremely happy to see me finish this work.

Abstract

In questa tesi vengono presentati gli esperimenti NA64 e GBAR che si pongono l'obiettivo di rispondere a due domande fondamentali ancora senza risposta nella fisica moderna: l'esistenza della materia oscura e l'asimmetria tra materia e antimateria. NA64 un esperimento svolto al CERN che ha come obiettivo la ricerca di un nuovo bosone gauge dato da una simmetria $U'(1)$, A' (anche detto fotone oscuro) che potrebbe mediare l'interazione tra materia oscura e materia ordinaria tramite una nuova forza debole. L'esperimento sensibile a un intervallo ancora inesplorato di valori del mixing γ-A', $10^{-5} < \epsilon < 10^{-3}$ e della massa del fotone oscuro $M_{A'} \leqslant 100$ MeV. I risultati del primo test beam sono riportati in questa tesi e sono presentati i nuovi limiti sul parametro di mixing γ-A' , questi risultati escludono l'esistenza di un A' con massa $\leqslant 100$ MeV nel caso di decadimento invisibile in grado di giustificare l'anomalia $(g\text{-}2)_\mu$. GBAR un esperimento situato presso l'accelleratore di antiprotoni al CERN che si pone l'obiettivo di misurare la caduta libera di un atomo di Anti-idrogeno con una precisione relativa dell' 1 % nella sua prima fase per testare in maniera diretta il principio di equivalenza per l'antimateria. L'esperimento user il fascio di particelle proveniente da ELENA per produrre ioni $\overline{\mathrm{H}}^+$ tramite linterazione con positronio, successivamente raffreddati a temperature ~ 10 μK ed infine rilever gli atomi $\overline{\mathrm{H}}$ dopo il photo-detaching di uno dei due positroni. Il segnale di detezione dato dallannichilazione del antiprotone rilevato tramite le tracce dei pioni prodotti nella reazione. L'esperimento attualmente in fase di preparazione al CERN con in programma un run di prova nel 2018. Per entrambi gli esperimenti un tracking preciso essenziale - NA64 richiede la ricostruzione precisa del momento delle particelle nel fascio per ridurre il background dovuto alle particelle a bassa energia presenti nello stesso. In GBAR un tracking preciso invece richiesto per individuare le tracce dei pioni prodotti durante l'annichilazione di $\overline{\mathrm{H}}$ e ricostruire cos con precisione il vertice di interazione nonch ridurre il background dovuto ai cosmici. In entrambi gli esperimenti presentati Micromegas resistive con multiplexing in XY sono state scelte some soluzione al tracking. L'uso di moduli per tracking con multiplexing non era mai stato testato in ambienti ad alta intensit in passato per via delle possibili disambuigit causate dalle propriet del multiplexing. I primi risultati delle performance di questi moduli sono stati testati presso CERN SPS con un fascio di elettroni aventi una quantit di moto pari a 100 GeV/c e ad un'intensit di 3.3×10^5 $e^-/sec/cm^2$. A queste intensit il fattore 5 di multiplexing utilizzato per i moduli introduce un livello di disambuiguit pari al 50 %. I risultati qui ottenuti provano che utilizzando le informazione sulla dimensione e la carica totale integrata di ciascun cluster il livello di disambuigit pu essere ridotto sotto il 2%. Le performance attese dei moduli Micromegas in GBAR sono inoltre presentate utilizzando la simulazione di annichilazione di $\overline{\mathrm{H}}$ utilizzando Geant4, tenendo conto dei parametri iniziali dell'atomo, l'accetanza della geometria e la risoluzione intrinseca dei moduli. Sono infine presentate la risoluzione della riconstruzione del vertice di annichilamento e la stima di rigezione del background.

Abstract

The experiments NA64 and GBAR aiming to explore the still unanswered questions in physics of the existence of dark matter and the matter- antimatter asymmetry, respectively, are presented in the scope of this thesis. NA64 is an experiment at CERN searching for a new $U'(1)$ gauge boson, A' (dark photon) which may mediate the interaction of dark matter with ordinary matter via a very weak force. The experiment is sensitive to the still unexplored area of γ-A' mixing strength $10^{-5} < \epsilon < 10^{-3}$ and masses $M_{A'} \leqslant 100$ MeV. The results from the first beam run are reported and new limits were set on the γ-A' mixing strength and the results exclude the invisibly decaying A' with a mass $\leqslant 100$ MeV as an explanation for the $(g\text{-}2)_\mu$ anomaly. GBAR is an experiment set up at the AD hall at CERN aiming to measure the free-fall of anti-hydrogen with a relative precision of 1 % in the first phase for a direct test of the equivalence principle for anti-matter. The experiment plans to use the ELENA anti-proton beam to produce $\overline{\mathrm{H}}^+$ ions from its interaction with positronium, cool the ions down to ~ 10 μK temperature and eventually detect the free-fall of $\overline{\mathrm{H}}$ after photo-detaching the excess positron from the ion. The signal of detection is given by its annihilation producing pion tracks. The experiment is being set up at CERN and is expected to start a commissioning run in 2018. For both experiments a tracker is essential - NA64 requires precise tracking of the incoming particles to reconstruct their momentum and suppress background from the low energy beam tail. In GBAR tracking is required to track the pion tracks and reconstruct the vertex of the $\overline{\mathrm{H}}$ annihilation and reject cosmic ray background. Multiplexed XY Resistive Micromegas modules chosen for the tracking requirements of both the experiments are presented. The use of multiplexed modules in high intensity environments was not explored so far, due to the effect of ambiguities in the reconstruction of the hit point caused by the multiplexing feature. The first performance results of multiplexed modules tested at the CERN SPS 100 GeV/c electron beam at intensities up to 3.3×10^5 $e^-/sec/cm^2$ is reported. At these rates, a factor 5 multiplexing introduces more than 50 % level of ambiguity. The results prove that by using the additional information of cluster size and integrated charge of the induced XY signal clusters the ambiguities can be reduced to a level below 2%. The expected performances of the GBAR Micromegas tracker is also summarized from the simulation of $\overline{\mathrm{H}}$ annihilation done with Geant4, taking into account the initial parameters of the atom, geometric acceptance and intrinsic resolution of tracker modules. The resolution of vertex reconstruction and estimation of the background rejection is also presented.

Contents

Chapter 1

Motivation

One of the main triumphs in the field of science and knowledge was a theory, developed in stages, through the works of various scientists along the latter half of the 20th century that explains nearly everything that rule our daily lives - from the fundamental structure of matter and energy to reactions that power the sun, from understanding the first moments of our universe's existence to the building blocks of our being. Physicist Robert Oerter called it "The Theory of Almost Everything" in his book named the same [1], but it is more commonly called the "Standard Model of Elementary Particles". Even though the Standard Model has been successful in explaining almost everything, it falls short in being a complete theory of fundamental forces and fails to explain some phenomena.

Observing the luminous matter in the Universe - stars, galaxies, cluster of galaxies and the hot gas in and between them, we learn how normal matter (made of atomic nuclei and electrons) interacts with light, which is an integral part of how we see the universe. Another lesson is that of the gravitational interactions. By observing the motion of visible matter relative to its surrounding and studying their gravitational interactions, we came across the greatest surprise that normal matter alone is not enough to account for the gravitational effects of these large structures. Observation of stars in spinning galaxies rotating at roughly the same speed, no matter their distance from the galactic centre is in contradiction with Kepler's law. Such behaviour could only be explained if huge amounts of invisible matter filled the entire galaxy and beyond [2]. Additionally, observation of gravitational lensing [3] [4] and data from cosmic microwave background [5] gave strong evidence for the existence of Dark Matter ([6]). The challenge to explain these hints presents one of the strongest motivations for the existence of new physics beyond the Standard Model (SM).

In addition to the puzzle of dark matter existence, the matter-antimatter assymetry presents another perplexing observation. As per the model of Big Bang equal amounts of matter and antimatter is expected in the first stages of the Universe. However, non-existence of primordial antimatter in the current Universe [7] points to our missing knowledge regarding some fundamental properties of antimatter. The Einstein Weak Equivalence principle (WEP) states that the trajectory of a test particle is independent of its composition and internal structure when it is only submitted to gravitational forces [8]. No direct tests of this fundamental principle have been done with antimatter which is further motivated by the recent observations of the acceleration of the expansion of the Universe [9]. This observation led to question the fundamental gravitation theory. Explaining the observations with the introduction of dark energy leads to difficult questions, since it appears as repulsive gravity.

All these facts question our basic understanding of very fundamental questions in physics which motivated various beyond the SM searches hoping to explain these phenomena.

The work of this thesis involved participating in two such experiments addressing these puzzles of the universe. NA64, an experiment at the CERN SPS beamline, is searching for dark matter candidates (A') in sub-GeV mass range and GBAR aims to test the gravitational behaviour of anti-hydrogen at rest as a direct test of the Equivalence Principle for antimatter. Both these experiments required development of tracking systems for their searches which was the main subject of this thesis. The work also included data taking for the NA64 beam time and participation in the publication of its first results. The motivations, principles and expected results from the experiments are presented in Chapters 2 - 3. The tracking detectors and their principle of operation is presented in Chapter 4. Detailed description of the experiments, simulation results and beam time data and analysis are presented in Chapters 5 - 8.

Chapter 2

NA64 - Search for invisible decays of sub-GeV dark photons in missing energy events

2.1 Introduction

Dark Matter still remains a great puzzle despite the intensive searches and efforts at the LHC and non-accelerator experiments [10]. Though various Dark Matter (DM) models have been ruled out by stringent constraints obtained on DM coupling to SM particles, little is known about the origin and dynamics of the dark sector itself. Several models of dark matter suggest the existence of dark sectors consisting of $SU(3)_C \times SU(2)_L \times U(1)_Y$ singlet fields. The difficulty in the searches arise because these sectors of particles do not interact with ordinary matter directly but could couple to it via gravity. In addition to gravity, however, there might be another very weak interaction between ordinary and dark matter mediated by $U'(1)$ gauge bosons, A' (dark photons), mixing with our photons. In a class of models the corresponding dark gauge boson could be light, having sub-GeV masses, and have the $\gamma - A'$ coupling strength, ϵ, lying in the experimentally accessible and theoretically interesting region where $\epsilon << 1$. This motivated high intensity frontier experiments to search for dark forces and other portals between the visible and dark sectors (Review available in [11] [12]).

An additional motivation for A' searches is provided by the 3.6 σ discrepancy between the predicted and experimental values for the anomalous magnetic moment $(g-2)_\mu$ of the muon, which could be explained by the presence of a sub-GeV A' with the coupling strength $\epsilon \sim 10^{-3}$. Loop effects of particles under both Dark and Standard Model $U(1)$ interactions, with a typical 1-loop value, $\epsilon = \mathrm{e}g_D/16\pi^2$ [14], where g_D is the coupling constant of the $U(1)_D$ gauge interactions, could give rise to such small values of ϵ. Sub-GeV mass A', with $M_{A'} \sim \sqrt{\epsilon} M_Z$, can be generated in several physics scenarios. Thus, if $U(1)_D$ is embedded in a Grand Unifed Theory (GUT), the mixing can be generated by a one (two)-loop interaction and naturally result in values of $\epsilon \sim 10^{-3}$-10^{-1} (10^{-5}-10^{-3}) [13]-[15].

One of the typical decay channel of A' could be visible decays to Standard Model leptons, l = e, μ or hadrons, which could be used to detect it. Stringent constraints on the mass of A', $M_{A'}$, have been put by previous beam dump, fixed target, collider, and rare meson decay experiments excluding, in particular, the parameter region favored by the $(g-2)_\mu$ anomaly [12]. However, in presence of light dark states with masses $< M_{A'}/2$, the A' could

predominantly decay invisibly into those particles provided that $g_D > \epsilon e$. Such A' model covering the parameter space explaining the $(g-2)_\mu$ anomaly was not yet excluded and remain unexplored. If such A' mediators exist, their invisible decays, $A' \rightarrow invisible$ could be searched for in missing energy events. NA64 was motivated to probe this region and potentially completely explore the still favored parameter space by $(g-2)_\mu$ and also cover a much larger region with enough accumulated statistics. It was designed as a hermetic general purpose detector to search for dark sector physics in missing energy events from electrons, hadrons, and muons scattering off nuclei.

2.2 Principle of the Experiment

NA64 is an experiment at the CERN SPS approved in March 2016 with the goal to search for $A' \rightarrow invisible$ decay with an electron beam. It is a fixed target experiment combining the active beam dump technique with missing energy measurement searching for invisible decays of massive A' produced in the reaction:

$$e^- Z \rightarrow e^- Z A' \tag{2.1}$$

of electrons scattering off a nuclei of charge Z, with a mixing strength $10^{-5} < \epsilon < 10^{-3}$ and masses $M_{A'}$ in the sub-GeV range [19].

The Standard model Langrangian is extended by the Dark Sector [23] as :

$$\mathcal{L} = \mathcal{L}_{SM} - \frac{1}{4} F'_{\mu\nu} F'^{\mu\nu} + \frac{\epsilon}{2} F'_{\mu\nu} F^{\mu\nu} + \frac{M^2_{A'}}{2} A'_\mu A'^\mu + i\overline{\chi}\gamma^\mu \delta_\mu \chi - m_\chi \overline{\chi}\chi - e_D \overline{\chi}\gamma^\mu A'_\mu \chi \tag{2.2}$$

where A'_μ is the massive vector field of spontaneously broken $U'(1)$ gauge group, $F'_{\mu\nu} = \delta_\mu A'_\nu$-$\delta_\nu A'_\mu$, and ϵ is the kinetic mixing parameter. The Dirac spinor fields, χ, are the Dark Matter fermions coupled to A'_μ by dark portal coupling constant e_D. The mixing term $\frac{\epsilon}{2} F'_{\mu\nu} F^{\mu\nu}$ results in the interaction of $A's$ with ordinary matter as [16] [17] [18].

$$\mathcal{L}_{int} = -\frac{\epsilon}{2} F_{\mu\nu} A'^{\mu\nu} \tag{2.3}$$

Therefore, any source of photons could produce a kinematically permitted massive A' state according to the mixings. For example, the interaction of a high energy electron beam in a heavy target as shown in Figure 2.1 can be the source of A' and this is exploited in the NA64 experiment. For the invisible search calculations the invisible decay mode is considered predominant, i.e., $\Gamma(A' \rightarrow e^+e^-) << \Gamma(A' \rightarrow \overline{\chi}\chi)$ assuming $M_{A'} > 2M_\chi$ where M_χ is the mass of the dark matter particles. The A' production cross-section illustrated in Figure 2.1 was calculated in the Weizsäcker-Williams (WW) approximation, which is used to describe electro-production processes for small angle scattering of charged particles where the virtual photon emitted by the scattering particle appears to be near the mass shell [20] [21], as:

$$\frac{d\sigma}{dx dcos\theta_{A'}} = \frac{8Z^2\alpha^3_{QED}\epsilon^2 E_0^2 x}{U^2} \frac{\zeta}{Z^2} [(1 - x + \frac{x^2}{2}) - \frac{x(1-x)M^2_{A'} E_0^2 x \theta^2_{A'}}{U^2}] \tag{2.4}$$

where $x = E_{A'}/E_0$, E_0 is the incoming electron beam energy, $E_{A'}$ is the A' energy, $\theta_{A'}$ is the lab frame angle between the emitted A' and the incoming electron and Z is the atomic number of the target nucleus and the rate of decay of $A' \rightarrow \overline{\chi}\chi$ is given by:

$$\Gamma(A' \rightarrow \overline{\chi}\chi) = \frac{\alpha_D}{3} M_{A'} (1 + \frac{2m^2_\chi}{M^2_{A'}}) \sqrt{1 - \frac{4m^2_\chi}{M^2_{A'}}} \tag{2.5}$$

Figure 2.1: NA64 Logo illustrating the A' production in the reaction $e^-Z \rightarrow eZA'$, with the subsequent invisible decay of A' as $A' \rightarrow \overline{\chi}\chi$.

. The function

$$U = E_0^2 x\theta_{A'}^2 + M_{A'}^2 \frac{1-x}{x} + m_e^2 x \tag{2.6}$$

determines the virtuality of the intermediate electron, where m_e is the mass of the electron. The effective flux of photons is given by

$$\zeta = \int_{t_{min}}^{t_{max}} dt \frac{t - t_{min}}{t^2} G_2(t) \tag{2.7}$$

where t = -q^2, $|\vec{q}| = U/(2E_0(1-x))$, $t_{min} \sim |\vec{q}|^2$, $t_{max} = M_{A'}^2$, and G_2(t) = $G_{2,el}(t) + G_{2,in}(t)$ is the sum of elastic and inelastic electric form factor [20]. x and $\theta_{A'}$ dependence of t_{min} is neglected in the numerical integration of 2.7.

For $M_{A'} \leqslant 1$ GeV and $E_0 \leqslant 100$ GeV/c, when $M_{A'}/E_0 << 1$ the approximation of collinear A' emission is justified. The cross-section integration over x and $\theta_{A'}$ gives

$$\sigma_{tot} \sim \frac{4}{3} \frac{\alpha^3 \epsilon^2 \zeta}{M_{A'}^2} log(\delta^{-1}) \tag{2.8}$$

where $\delta = \max(M_{A'}^2/E_0^2, m_e^2/M_{A'}^2)$ is the infrared cut-off of the cross-section, which regulates either soft intermediate electron singularity or validation of WW approximation [20]. The NA64 experiment aimed to exploit this decay channel and was setup at the CERN SPS H4 e^- beamline. The schematic of the experiment is shown in Figure 2.2. The 100 GeV/c electron beam entering the setup is dumped against an electromagnetic calorimeter (ECAL), which is a sandwich of lead and scintillators, to produce massive A' through scattering off the heavy nuclei. In case of a A' production, a fraction of the energy will be deposited in the ECAL and the rest will be carried away by the A' without any interaction downstream of the ECAL. Detailed description of the experimental setup is given in Section 5.1. The signature for a signal will be missing energy in the ECAL and no activity in the VETO and the hadronic calorimeter modules (HCAL) which requires precise identification of the incoming particle and its momentum as is done upstream the ECAL (indicated in Figure 2.2).

In order to estimate the performance of the experiment a Monte Carlo simulation of the electromagnetic shower development in the ECAL was performed with Geant4. First the total and differential cross-sections of the A' production were calculated as a function of the electron energy E_0 (Eq 2.4). Next the A' emission was randomly generated at each step of the electron propagation in the ECAL target and the values for x, $cos\theta$ and the azimuthal angle

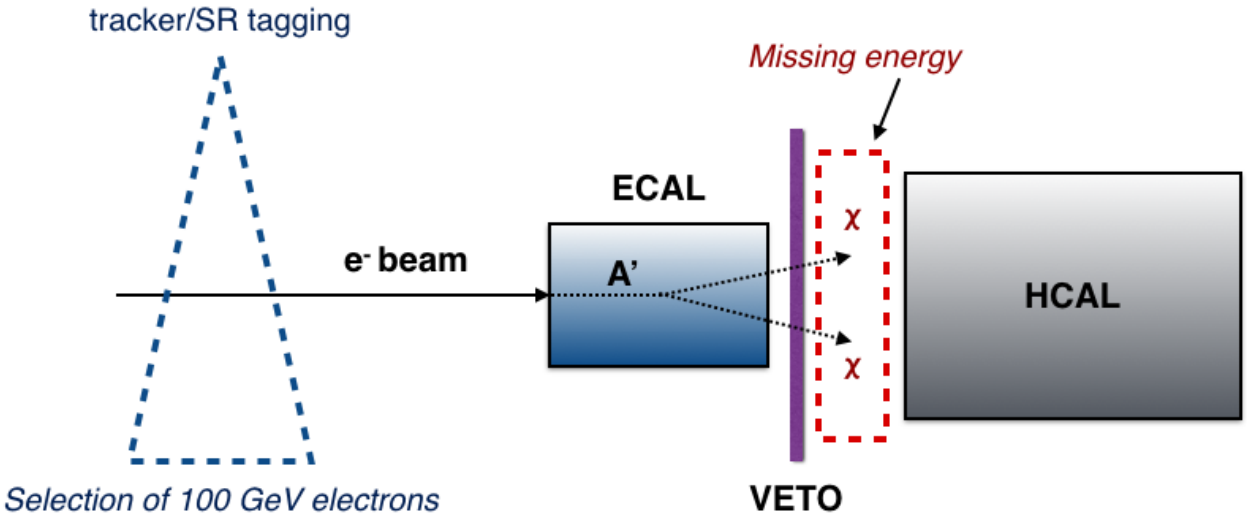

Figure 2.2: Schematic of the NA64 experimental setup.

$\phi_{A'}$ were generated for the accepted emissions. Finally the 4-momentum of the recoil electron was calculated. Figure 2.3 shows the A' emission spectra for masses $M_{A'} = 10$ MeV and 500 MeV as an example representing the missing energy spectra in the detector. From the estimation of the A' emission spectra as a function of the missing energy in the detector, the expected sensitivity of the experiment can be estimated given the missing energy threshold.

2.3 Expected Results

To estimate the scope of the search for NA64 two possible outcomes were considered: 1) Observation of an excess of signal events consistent with the reaction 2.1, 2) non observation of an excess of signal events.

2.3.1 Extraction of $M_{A'}$ and ϵ from missing energy spectrum in case of observation of signal events

In order to estimate the sensitivity of NA64 to derive parameters $M_{A'}$ and ϵ, a Geant4 based Monte Carlo simulation was performed considering values $M_{A'} = 20$ and 200 MeV and mixing strength $\epsilon \sim 10^{-3}$ [23]. Two possibilities a) observing $\leqslant 100$ signal events, b) observing larger number of signal events, were considered for the estimation.

The distribution of the observed number of signal events, n, follows a Poisson spectrum as :

$$P(n, n_{A'}) = \frac{n_{A'}^n}{n!} e^{-n_{A'}} \tag{2.9}$$

where $n_{A'}$ is the average number of signal events from the target, depending mainly on the mixing strength, ϵ, $M_{A'}$, energy of the incoming electron, E_0 and the number of electrons on target, n_{eot} and is given by [24]:

$$n_{A'} = n_{eot} \frac{\rho N_A}{A_{Pb}} \epsilon_{eff}(M_{A'}) \sum_{i}^{T} n(E_0, E_e, l) \sigma_{tot} \Delta l_i \tag{2.10}$$

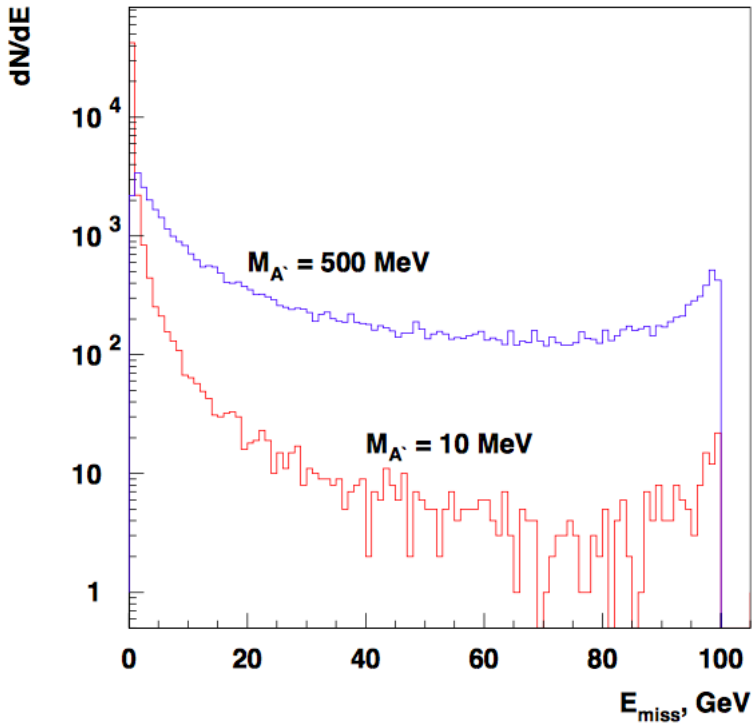

Figure 2.3: The A' emission spectra from the interaction of a 100 GeV/c e^- beam in the Pb target calculated for $M_{A'}$ = 10 MeV and 500 MeV. The spectra are normalized to about the same number of events. Taken from [23]

where ρ is the density of the Pb target, N_A is the Avogadro's number, A_{Pb} is the atomic mass of Pb, ϵ_{eff} is the overall signal efficiency, $n(E_0, E_e, l)$ is the number of $e^{\pm}$ with energy E_e and at depth l (in radiation lengths) in the electromagnetic shower within the target of total thickness, T and σ_{tot} is given by Eq. 2.8. Summing 2.10 over the missing energy spectrum in the ECAL (Figure 2.3), $n_{A'}$ can be approximated as [23]:

$$n_{A'} = \frac{k.n_{eot}}{10^{12}}(\frac{\epsilon}{10^{-5}})^2(\frac{10\text{MeV}}{M_{A'}})^2 \tag{2.11}$$

where parameter k depends weakly on $M_{A'}$. The Poisson distribution can be approximated by a Normal distribution for $n_{A'} >> 1$, thus giving the number of signal events at 1σ confidence level for a given ϵ and $M_{A'}$ as

$$n_{A'} - \sqrt{n_{A'}} \leq n \leq n_{A'} + \sqrt{n_{A'}} \tag{2.12}$$

Thus using 2.11 and 2.12 one can estimate the ratio $\frac{\epsilon^2}{M_{A'}^2}$ from the data.

In case of observation of more signal events, $n_{A'} \geqslant 10^3$, and $\sim 10^{12}$ n_{eot} with $M_{A'} \leqslant 50$ MeV, a more precise measurement of the correlated parameters ϵ and $M_{A'}$ is possible based on Equation 2.8 and dependence of the missing energy spectrum on $M_{A'}$. Two cases with $E_{miss} > 0.5\text{E}_0$ and $E_{miss} > 0.2\text{E}_0$ were checked for comparison. The E_{miss} distribution was compared between the "observed" number of events and the simulated spectra for each point of (ϵ,$M_{A'}$). The Kolmogorov and χ^2 test used for the compatibility test gave similar results and the allowed regions with probabilities expressed in terms of the corresponding standard deviations was obtained. The one standard deviation ellipse contours for the best fit

parameters for different E_{miss} thresholds are shown in Figure 2.4. For $n_{eot} = 10^{12}$ collected events the best fit parameters are found to be $M_{A'} = 21.6$ MeV and $\epsilon = 1.1 \times 10^{-3}$, which would be possible in a few months running time. It should be noted that the precision on $M_{A'}$ and ϵ for a given n_{eot} drops with increasing values of $M_{A'}$.

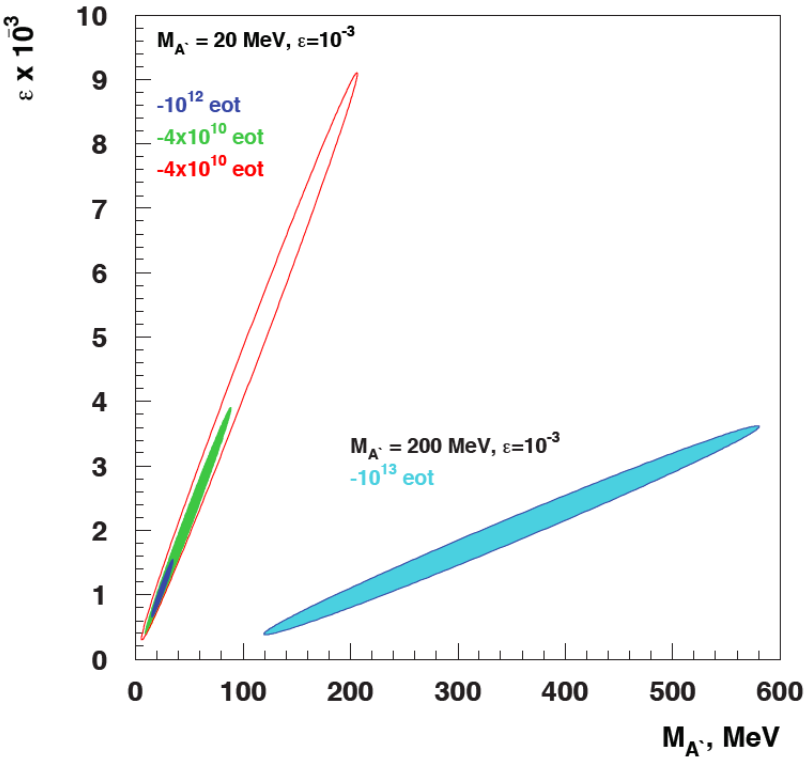

Figure 2.4: The fitted $\chi^2 = 1$ contours in the ϵ vs $M_{A'}$ plane for invisibly decaying A' obtained from the E_{miss} spectra for $M_{A'} = 20$ MeV and $\epsilon = 10^{-3}$ with missing energy $E_{miss} > 0.2E_0$ for 4 $\times$ 10^{10} (green area) and 10^{12} (blue area) n_{eot}, respectively. The red contour is calculated for $E_{miss} > 0.5E_0$ and 4 $\times$ 10^{10} n_{eot}. The fitted $\chi^2 = 1$ contour for $M_{A'} = 200$ MeV, $\epsilon \sim 10^{-3}$, $E_{miss} > 0.5E_0$ and $n_{eot} \sim 10^{13}$ is also shown for comparison. Taken from [23].

2.3.2 Expected Sensitivity in case of non observation of signal events

For the case of non-observation of an excess of signal events, NA64 will be able to set bounds on the (ϵ,$M_{A'}$) parameter space. The expected bounds were estimated with Geant4 MC simulation [23] of A' yield in NA64 assuming no background events are observed for the given n_{eot}. The acceptance of the detector is defined as $\eta_{acc} = n_{A'}(E_{miss} > 0.5E_0)/n^{tot}_{A'}$ where $n_{A'}(E_{miss} > 0.5E_0)$ is the number of signal events with $E_{miss} > 0.5E_0$ which was the chosen threshold for the experiment. The background extrapolations from data was used to calculate the overall sensitivity of the experiment with the signal Monte Carlo for different missing energy thresholds and the optimum cut of $E_{miss} = 0.5E_0$ was thus established taking into account the A' emission spectra for the selected threshold [25]. $n^{tot}_{A'}$ is the total number of events with a dark photon emission in the target.

The expected 90 % confidence level bounds on ($M_{A'}$, ϵ) parameter space can be obtained using Eq 2.10 and the relation $n^{90\%}_{A'} > n_{A'}$, where $n^{90\%}_{A'}$ =2.3 is the 90% CL upper limit for the

number of signal events without background. Figure 2.5 shows the expected bounds obtained for $n_{eot} = 10^9$, 10^{10}, 10^{11} and 10^{12} and $E_0 = 100$ GeV/c. All these calculations are based on the assumption that the invisible decay is the predominant channel for A'. A comparison of

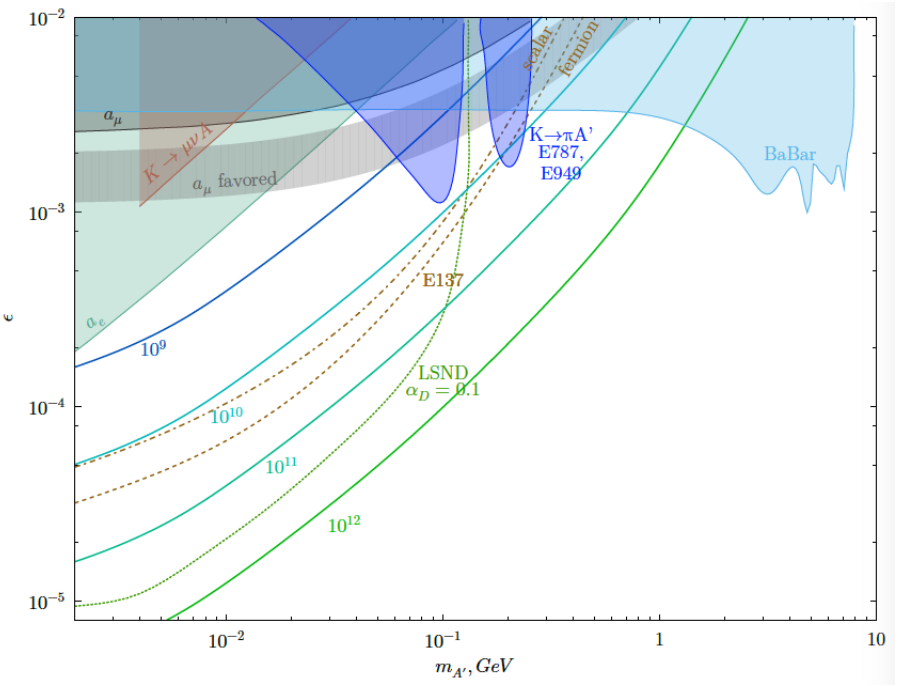

Figure 2.5: Expected exclusion region in the ($M_{A'}$, ϵ) plane from NA64 for 10^9, 10^{10}, 10^{11} and 10^{12} incident electrons of energy $E_0 = 100$ GeV/c taken from [23]. Direct constraints from BaBar [112], [113], E787+ E949 experiments [116], [114], as well as (g-2)$_\mu$ favored area are also shown [115]. Indirect constraints (95% C.L) for dark photons A' decaying invisibly to a pair of light DM χ, extracted from the SLAC E137 [117] for a Dirac fermion or complex scalar (broken brown) DM and from the LSND experiments [118] (green dotted) under assumption $\alpha_D = 0.1$ are also shown. For more limits obtained from indirect searches and planned measurements see e.g. Refs. [119], [120]

the expected sensitivity calculated as above with the one evaluated by Izaguirre et al., [112] (IKST- Izaguirre, Krnjaic, Schuster, Toro) for the case of W-Sc ECAL and 10^9 eot is shown in Figure 2.6. For comparison the beam energy $E_0 = 10$ GeV/c, $E_{miss} > 0.9E_0$ and $n_{eot} = 10^9$ and 10^{12} was considered. Results with a Pb-Sc ECAL, $E_{miss} > 0.5E_0$ and $E_0 = 100$ GeV/c is also presented for comparison.

Since the signature for the invisible search is missing energy, the main sources of background for this search come from

1. electrons in the low energy tail of the beam mistaken as a high energy one depositing all its energy in the ECAL,

2. beam hadrons producing a low energy neutral pion in the very beginning of the ECAL and then escaping detection,

3. kaons in the beam decaying before the ECAL in a muon and two neutrinos that carry away an energy larger than the ECAL threshold and the muon being undetected in the HCAL,

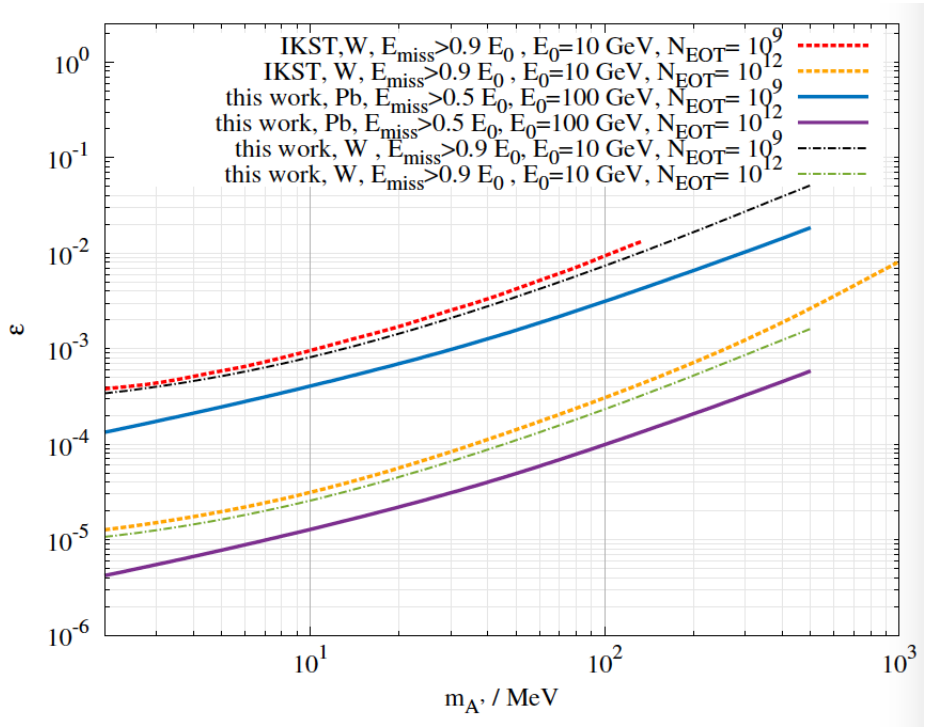

Figure 2.6: Comparison of the upper limits in ϵ vs $M_{A'}$ plane for invisibly decaying A' calculated for the W-ECAL target [122], $E_0 = 10$ GeV/c , and $E_{miss} > 0.9E_0$ by Izaguirre et al. [112] (IKST) and as presented above for 10^9 eot (red dashed and black dash-dotted), and 10^{12} eot (orange dashed and green dash-dotted), respectively. For comparison limits calculated for the Pb-Sc ECAL target, $E_0 = 100$ GeV/c , and $E_{miss} > 0.5E_0$ for 10^9 eot (blue solid) and 10^{12} eot (purple solid), respectively, are also shown. Taken from [23]

4. muons producing a low energy photon in the ECAL, which is absorbed in the calorimeter while the muon penetrates the rest of the detector without being detected.

Detailed description of all the expected background sources and their suppressions are presented in Section 5.2. When NA64 was first proposed, using synchrotron radiation tagging alone to suppress the low energy electron tail and hadron contamination by detecting the synchrotron radiation of the incoming particle was planned [37]. However, simulations showed (Section 6.1) that due to the bremsstrahlung contribution as a result of interaction of the particles with the detector material it is not possible to suppress these background at the level required. To successfully suppress the low energy tail background a spectrometer has therefore been proposed and implemented for NA64 to track the incoming particles and reconstruct their momentum in a magnetic field [39]. One of the aim of this thesis was to design and build an efficient spectrometer to identify and track the incoming particles at a high rate.

NA64 had two runs in 2016 focusing on the A' parameter space suggested for the $(g\text{-}2)_\mu$ anomaly. First results from the two weeks beam time in July' 2016 was published in [26] where most of the $(g\text{-}2)_\mu$ favored parameter space was excluded. The work of this thesis involved design, procurement and testing of the trackers along-with its software development for readout and analysis, simulation and analysis of synchrotron radiation detection for particle identification, participation in the experiment beam time for data taking, analysis of the data (Chapter 6) and publication of results. Ten times more statistic was also acquired during the October' 2016 beam time, analysis of which is ongoing.

Chapter 3

GBAR- Gravitational Behaviour of Antimatter at Rest

3.1 Introduction

Even though there is no compelling reason for a difference between the gravitational behaviour of matter and antimatter, studying antimatter systems to answer its yet unexplained properties regarding fundamental forces is an active field of research in physics today. From a theoretical point of view, models such as super-gravity may contain components inducing repulsive gravity (e.g., the seminal paper of Scherk [40]), thus violating the Weak Equivalence Principle (WEP). An extension of the standard model of particle physics, with terms directly violating the Lorentz and CPT symmetries (Kostelecky and Tasson [43]), could accommodate a very large difference between the inertial and gravitational masses of an antimatter particle. A model with negative masses for antiparticles was used to simulate the evolution of the Universe since the Big Bang (Benoit-Levy and Chardin [44]), resulting in predictions for cosmological observable in agreement with measurements. Such a model does not require the hypotheses of dark matter or dark energy, or the inflation episode, to describe the Universe. However, the equivalence principle has been indirectly tested by comparing particle-antiparticle properties, e.g comparison of the decay parameters of K0-$\overline{\text{K0}}$ in CP LEAR [45] or the simultaneous measurement of p-$\bar{p}$ cyclotron frequencies [42], a direct test of the equivalence principle, like measuring the free-fall of anti-atoms, is required. It is thus extremely interesting to test antimatter in a gravity field which serves as the motivation for GBAR that aims to measure the free-fall acceleration of neutral anti-hydrogen atoms in the terrestrial gravitational field, which is quoted as $\overline{g}$ in this paper.

Since the gravitational force is weak, shielding against electromagnetic influences to directly test free-fall of charged anti-particles (e.g positrons and antiprotons) have been a challenge in the past. On the other hand slowing anti-neutrinos to measure their gravitation or testing gravity on positronium and muonium is very difficult to undertake [47]. The simplest and most feasible anti-matter system seems therefore to be anti-hydrogen.

The Gravitational Behaviour of Antimatter at Rest (GBAR) is an experiment in preparation at CERN [48] with the goal to measure the gravitational acceleration $\overline{g}$ imparted to freely falling anti-hydrogen ($\overline{\text{H}}$) atoms, in order to perform a direct experimental test of the Weak Equivalence Principle with antimatter. The objective is to reach a relative precision on

$\overline{g}$ of 1% in a first stage, with the potential to reach a much higher precision of $10^{-3} - 10^{-5}$ using quantum gravitational states in a second stage [50].

3.2 Principle of the experiment

In order to measure directly the gravitational acceleration of anti-hydrogen atoms the key necessity is to obtain anti-atoms with less than 1 m/s velocity, i.e. to cool them to less than 20 μK to be able to observe a vertical free-fall. The laser cooling limit for neutral hydrogen is, due to the photon recoil, at 1.3 mK [49]. The proposed path gets around this limitation by producing an intermediate state, the antimatter counterpart of the H^- ion, i.e. $\overline{H}^+$, which consists of an antiproton, and two positrons, as suggested by Walz and Hänsch [51]. The ion can be cooled down to μK temperatures (i.e. m/s velocities) through interactions with positively charged ions since Coulomb repulsion prevents the annihilation of the $\overline{H}^+$ ions. The extra positron can then be laser detached in order to recover the neutral $\overline{H}$ atom and observe its free-fall as illustrated in Figure 3.1. The photodetachment process can be set up to

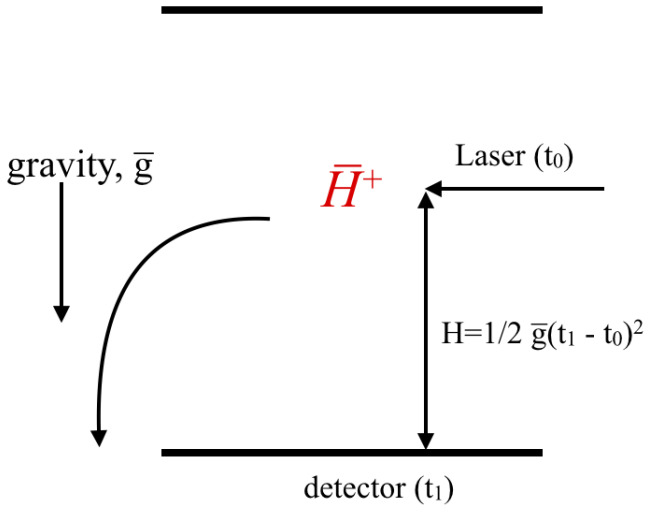

Figure 3.1: Scheme to photo-detach the excess positron from the trapped $\overline{H}^+$ ion to measure the free-fall of $\overline{H}$.

minimize momentum transfer in the vertical direction. The very low velocity of the atom leads to a quasi-vertical free-fall, much easier to detect than a horizontal deflection. The falling anti-atom annihilates on the vacuum vessel's wall, delivering a large signal used to measure the time of flight since the photo-detachment. Knowing the distance between the laser beam and the annihilation point provides a measurement of $\overline{g}$ from the classical formula as shown in Figure 3.1. The height is measured from the reconstruction of the vertex of annihilation of the $\overline{H}$ atom. The $\overline{H}$ annihilates on the detector plate producing pion tracks which are detected by trackers placed around the free-fall chamber. The trackers are also required for background rejection of cosmic rays which is the main source of background for the experiment. The work of this thesis included the design, construction and testing of the tracker modules to reach the required precision on the vertex reconstruction for the aimed relative precision on $\overline{g}$.

The $\overline{\mathrm{H}}^+$ ion is produced through two charge-exchange processes from interactions of $\overline{p}$ and $\overline{\mathrm{H}}$ with the same positronium target (Pérez and Rosowsky [52]) :

$$\mathrm{Ps} + \overline{\mathrm{p}} \rightarrow \overline{\mathrm{H}} + \mathrm{e}^- \tag{3.1}$$

$$\mathrm{Ps} + \overline{\mathrm{H}} \rightarrow \overline{\mathrm{H}}^+ + \mathrm{e}^- \tag{3.2}$$

Extensive calculations of cross-section and studies have been carried out for these two reactions (Merrison et al [53], Mitroy [54]) and a set of cross-sections have been obtained for both reactions as shown in Figures 3.2 3.3 [55]. From these calculations one can estimate for the expected number of low-energy anti-protons of 5×10^6 per burst from the ELENA beam-line at CERN, a high surface density ($\sim 10^{12}\mathrm{cm}^{-2}$) Ps is necessary for one $\overline{\mathrm{H}}^+$. Also since the binding energy of $\overline{\mathrm{H}}^+$ and the energy level of the third excited state of Ps is the same (0.76 eV), an enhancement in the cross-section is expected if Ps is excited.

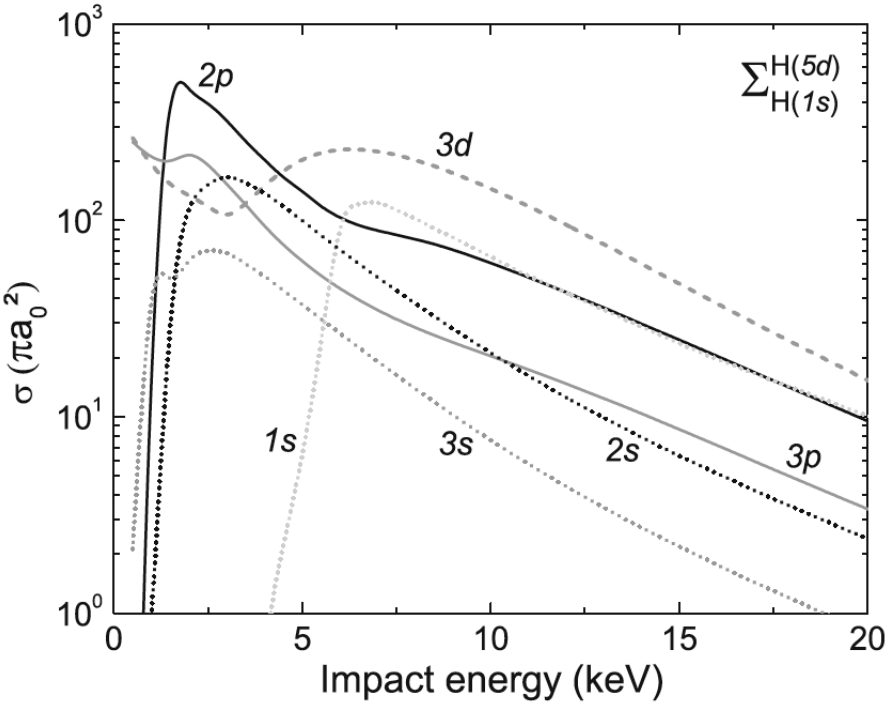

Figure 3.2: Antihydrogen ($\overline{H}$) production cross-sections from various state of positronium, Ps(1s) to Ps(3d) [55]

A future prospect comes from the expectation that $\overline{\mathrm{H}}$ will be reflected from a "annihilation plate" with nearly 90% probability if launched from few tens of micrometres above its surface. The phase space of these ultra-cold anti-atoms is comparable to that of ultra-cold neutrons made to bounce on a material surface at the ILL reactor, where quantum states were obtained in the potential composed of gravity and quantum reflection, leading to a spectrum of quantum states (Nesvizhevsky et al [56]). The spectroscopy of these "gravitational" levels should lead to orders of magnitude improvement on the error on $\overline{g}$ (Voronin et al [57]) and reach a relative precision $< 10^{-3}$ in the second phase.

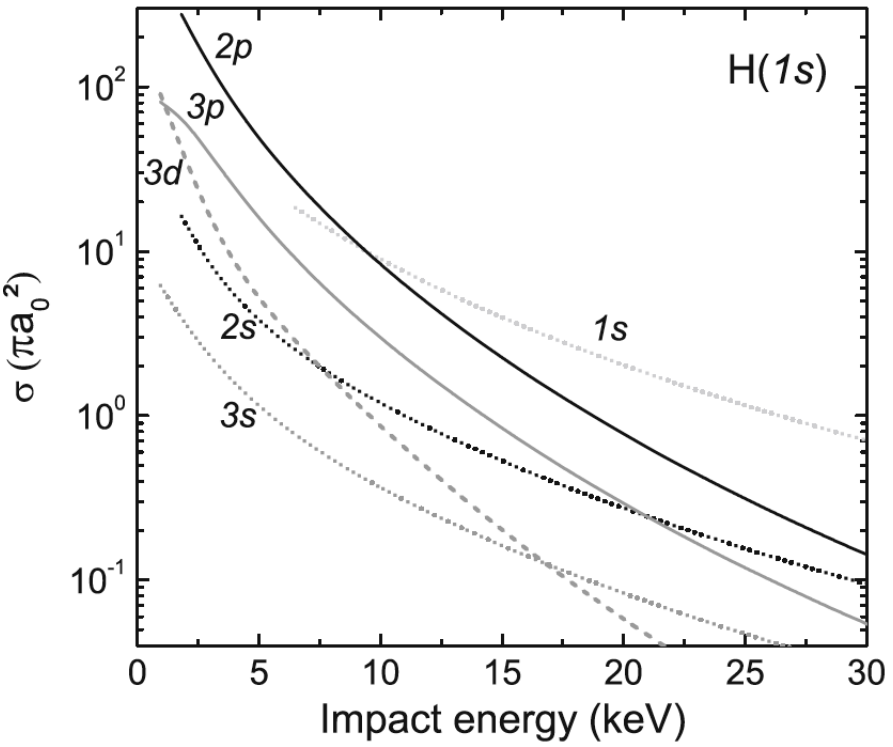

Figure 3.3: Antihydrogen ion ($\overline{H}^+$) production cross-sections from various state of positronium, Ps(1s) to Ps(3d) [55]

3.3 Statistical Precision on $\overline{g}$

The statistical precision on $\overline{g}$ is a function of its initial parameters and state. The photo-detachment of $\overline{\mathrm{H}}^+$ causes a recoil in the atom, which contributes predominantly to the horizontal velocity, due to: 1) the absorption of the laser, and 2) the positron emission. The recoil due to the absorption is given by

$$v_{abs} = \frac{p_\gamma}{m_H} \sim 0.2\mathrm{m/s} \tag{3.3}$$

where p_γ is given by the binding energy of $\overline{\mathrm{H}}^+$, $E_B = 0.76$ eV/c. In order to minimize the recoil on the ion due to the subsequent positron emission, the laser wavelength is set very close to that of the photo-detachment threshold. The recoil due to emission is given by

$$v_{emission} = \frac{\sqrt{2m_e E_c}}{m_H} \sim 1\mathrm{m/s} \tag{3.4}$$

where $E_c = E_\gamma$-$E_B = 15$ μeV is the photon energy above threshold for the chosen laser of the experiment. The subsequent $\overline{\mathrm{H}}$ annihilation on a plate placed at a given height, H, below is detected by tracking the pions from the annihilation with trackers placed around the free-fall chamber. This provides the stop signal used to measure the free fall time t and the vertex from the track reconstruction gives the point of annihilation in the free-fall chamber to extract $\overline{g}$ from the classical free-fall formulae:

$$H = v_0 t + \frac{1}{2} g t^2 \tag{3.5}$$

where v_0 is the unknown initial vertical velocity of the atom. The uncertainty on $\overline{g}$ is thus given by:

$$\frac{\Delta\overline{g}}{\overline{g}} = \sqrt{(2\Delta t/t)^2 + (\Delta H/H)^2} \tag{3.6}$$

where,

$$\begin{aligned}\frac{\Delta t}{t} &= \sqrt{(\Delta H/H)^2 + (\Delta v/v_H)^2} \\ &= \sqrt{(\Delta H/H)^2 + (\hbar/2mv_H\Delta H)^2}\end{aligned}$$

since

$$\begin{aligned}v_H &= \sqrt{2gH} \\ \Delta v &= \frac{\hbar}{2m\Delta H} \quad \text{From Heisenberg's uncertainty principle}\end{aligned}$$

with $\hbar$ being the reduced Planck constant, Δv being the vertical velocity dispersion, H the free-fall height, m being the mass of the anti-hydrogen atom and t the time of free-fall. Its possible to estimate an optimum size of the initial state for the minimum Δt as

$$\Delta H_{opt} = \sqrt{\frac{\hbar H}{mv_H}} \tag{3.7}$$

So for a free-fall height of 25 cm the $\Delta H_{opt} \sim 85$ μm. The ion is trapped in a Paul trap prior to the photo-detachment to cool it down to μK temperatures. Therefore, the dispersion in the free-fall height and the vertical velocity is characterized by the Paul trap oscillation frequency, ω, as

$$\Delta H = \sqrt{\hbar/2m\omega}, \quad \Delta v = \sqrt{\hbar\omega/2m} \tag{3.8}$$

The considered Paul trap frequency range for GBAR lies between 0.1 MHz $< \omega/2\pi <$ 1 MHz [58]. For example for an oscillation frequency $\omega/2\pi \sim 0.5$ MHz, $\Delta H \sim 0.1$ μm and $\Delta v \sim 0.3$ m/sec. Thus, if all annihilation occur on the bottom plate of the free-fall chamber the uncertainty on $\overline{g}$ is mainly dominated by the initial velocity dispersion and the relative precision is given by

$$\frac{\Delta\overline{g}}{\overline{g}} = \frac{2\Delta t}{t} = \frac{2\Delta v}{v_H} \tag{3.9}$$

for a single detected annihilation event ~ 0.3 for a free-fall height of 25 cm, and for a total number of, N_{tot}, $\overline{\mathrm{H}}$ annihilation detected the relative precision is given by

$$\frac{\Delta\overline{g}}{\overline{g}\sqrt{N_{tot}}} = \frac{2\Delta v}{v_H\sqrt{N_{tot}}} \tag{3.10}$$

However if the free-fall chamber has a small diameter such that the annihilation occurs on the side walls the resolution on the free-fall height effects the resolution on $\overline{g}$. Therefore, its important to optimize the geometry of the free-fall chamber to require a minimum number of events to reach the relative precision of 1 % taking into account all acceptance effects and initial parameters of the atom and have precise tracker modules to reconstruct the vertex of annihilation. A proposed solution to reach a much higher precision on $\overline{g}$ was to further reduce the dispersion on the vertical velocity, since the main uncertainty on $\overline{g}$ is predominantly due to the initial velocity dispersion of the atom. A scheme has been proposed to "shape" the

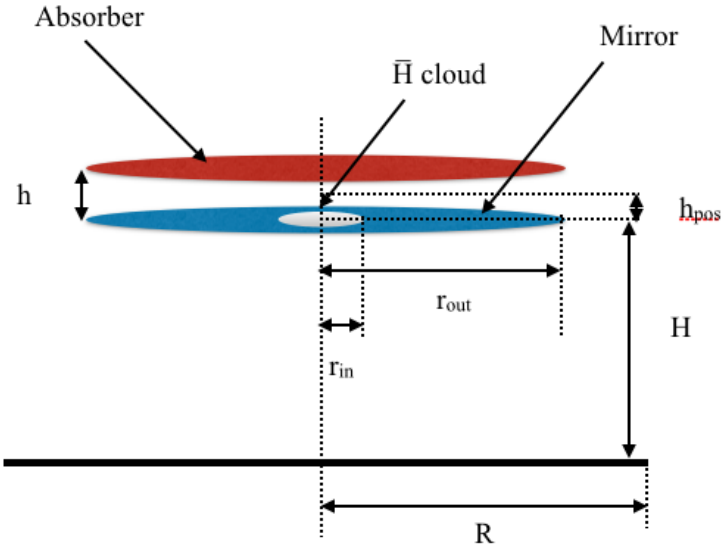

Figure 3.4: Proposed vertical velocity shaping device [59].

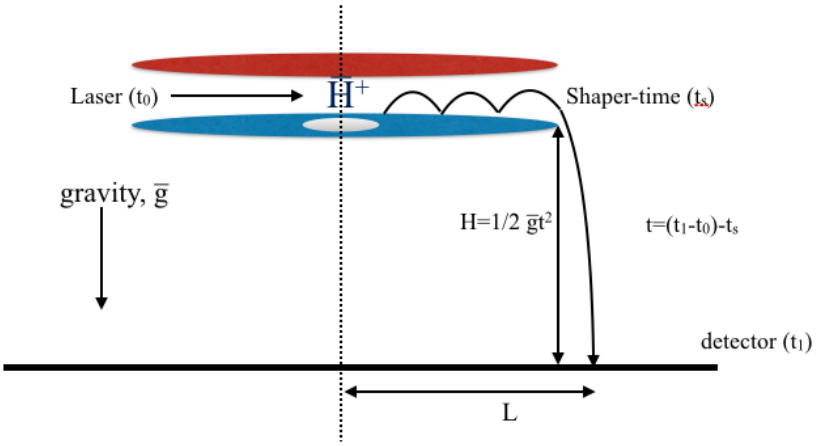

Figure 3.5: Principle of free-fall using shaper.

vertical velocity of the atom [59] using a disk with a mirror surface on the bottom and a rough top surface as shown in Fig. 3.4 similar to the experiments that observed gravitational quantum states of ultra-cold neutrons [60], to reach a much higher precision $< 10^{-3}$ in the second phase of the experiment. Due to the high efficiency of quantum reflection at small energies because of the Casimir interaction [61], atoms with sufficiently low vertical velocities will bounce off the bottom mirror without any effect on the horizontal velocity component if the mirror surface can be made flat, smooth and horizontal. This will allow the atoms to pass through the shaping device with a high probability and annihilate on the detection plate H m below as mentioned above. Atoms with higher vertical velocities will touch the rough top surface and annihilate. In order to estimate the expected resolution on $\overline{g}$ with this scheme classical trajectories of the atom are considered. As shown in Figure 3.4 a central opening of radius r_{in} is left at the centre as the shaper has to be coupled with the Paul trap (not shown in the Figure) which traps the $\overline{\mathrm{H}}^{+}$ ions before the photo-detachment. The losses due to the Paul trap acceptance are not included in this estimation. The outer radius of the shaper is taken as r_{out} with the height of the slit being h and the initial atom placed at a height h_{pos}

from the bottom mirror. In this approximation h_{pos} is taken as 0. Assuming the ideal case of $r_{in} \to 0$ and $r_{out} \to \infty$, and not taking into account losses due to imperfect quantum reflections, the fraction of atoms passing through the acceptance of the shaper is given by

$$\frac{N}{N_{tot}} \sim \frac{\Delta v_{shap}}{\Delta v}\sqrt{\frac{1}{2\pi}} \tag{3.11}$$

where N is the number of events passing through the shaper and $\Delta v_{shap} = \sqrt{2\overline{g}h}$ is the range of velocities accepted within the shaper of height h. The above equation is valid for the velocity selection $\Delta v_{shap} < \Delta v$, which gives a maximum value for h as

$$h < h_{max} = \frac{\Delta v^2}{2\overline{g}} \tag{3.12}$$

Given the dispersion of the vertical velocity ~ 0.3 m/sec, presented before due to the Paul trap frequency, the value for $h_{max} \sim 5$ mm.

For proper functioning of the shaper scheme, finite values for r_{in} and r_{out} need to be considered. The Paul trap is expected to introduce anisotropy between the horizontal and the vertical components of the atom, described by the ratio e in the interval $2 < e < 4$ [62], as $\omega_{hor} = e\omega$, where ω is the frequency of operation for the vertical trap. Thus the horizontal dispersion obtained is

$$\Delta v_{hor} = \Delta v\sqrt{e}, \quad \Delta H_{hor} = \Delta H/\sqrt{e} \tag{3.13}$$

For optimum acceptance of the shaper and reduce losses at its entrance the radius r_{in} should be chosen such that the angular divergence fits the angular acceptance, so

$$\frac{h}{r_{in}} > \frac{\Delta v_{shap}}{\Delta v_{hor}}, \quad r_{in} < r_{in}^{max} = \frac{\Delta v\sqrt{eh}}{\sqrt{2\overline{g}}} = \sqrt{ehh_{max}} \tag{3.14}$$

In order to effectively select atoms with small vertical velocity, r_{out} should be large enough such that those atoms touch the rough top surface at least once. Therefore, the time, t_s, spent between the shaper should be at least two times larger than the time of free-fall through the height h, t_h, so

$$t_s = \frac{r_{out}}{v_{hor}} > 2t_h = 2\sqrt{\frac{2h}{\overline{g}}}$$
$$\to r_{out} > r_{out}^{min} = \frac{4v_{hor}\sqrt{h}}{\sqrt{2\overline{g}}}$$

where v_{hor} is the horizontal velocity of the atom.

In order to estimate the statistical uncertainty on $\overline{g}$ with this method the same consideration as in Eq 3.6 can be made with the uncertainty on the time of free-fall now given by

$$\left(\frac{\Delta t}{t}\right)_{shap} = \sqrt{(\frac{h}{2H})^2 + (\frac{\Delta v_{shap}}{v_H})^2} \tag{3.15}$$

With $\Delta v_{shap} = \sqrt{2\overline{g}h}$ and $v_H = \sqrt{2\overline{g}H}$ and $h << H$, the relative spread $(\Delta t/t)_{shap}$ can be written as

$$\left(\frac{\Delta t}{t}\right)_{shap} \sim \sqrt{\frac{h}{H}} \tag{3.16}$$

and the accuracy of

$$\Big(\frac{\Delta\overline{g}}{\overline{g}}\Big)_{shap} \sim 2\sqrt{\frac{h}{H}} \tag{3.17}$$

for each detected annihilation. Thus using Eq 3.11 we get the relative precision on $\overline{g}$ with respect to the detected annihilation events as

$$\Big(\frac{\Delta\overline{g}}{\overline{g}\sqrt{N}}\Big)_{shap} = 2\sqrt{\frac{h}{H}}\sqrt{\frac{\Delta v\sqrt{2\pi}}{N_{tot}\Delta v_{shap}}} = \Big(\frac{2\pi h\Delta v^2}{\overline{g}H^2N_{tot}^2}\Big)^{1/4} \tag{3.18}$$

To estimate the improvement in the resolution on $\overline{g}$ with respect to the case without the shaper Eq 3.10 is compared with Eq 3.18 and the improvement is given by the ratio

$$\Big(\frac{2\pi h\Delta v^2}{\overline{g}H^2N_{tot}^2}\Big)^{1/4} / \Big(\frac{2\Delta v}{v_H\sqrt{N_{tot}}}\Big) = \Big(\frac{2\pi h}{h_{max}}\Big)^{1/4} \tag{3.19}$$

Thus the best accuracy is achieved for smaller slit sizes as will be presented in Chapter 8. From the above equation it is clear that for the shaping device to work optimally, the slit height h should be smaller than $h_{max}/2\pi = 0.8$ mm and thus with this scheme even though the acceptance of the $\overline{\mathrm{H}}$ annihilation decreases the improvement in the velocity dispersion helps achieve much higher relative precision on $\overline{g}$. It will also be possible to achieve the same relative precision with much lower statistics.

For example for a slit height of $h = 0.1$ mm, free fall of $H = 25$ cm, the anisotropy of the Paul trap described by e =3, r_{in} should be < 1.2 mm, r_{out} should be > 9 mm resulting in a relative precision of $\Delta\overline{g}/\overline{g} \sim 0.03$ for a single annihilation detection and an acceptance of the shaper ~ 6 %. Therefore, with this scheme for ~ 1000 $\overline{\mathrm{H}}^+$ trapped ions a relative precision of ~ 0.4 % can be expected with the shaper as opposed to ~ 1 % without it.

Setup	No. of $\overline{H}^+$ ions	Main Limitation	$\sigma_{d\overline{g}/\overline{g}}$	Relative precision
Without Shaper	1000	Δv = 0.3 m/sec	0.3	1 %
With Shaper, h = 0.1 mm	10	Δv = 0.04 m/sec	0.03	1%

Table 3.1: Summary of achievable relative precision on $\overline{g}$ with the main limitation of the vertical velocity dispersion, Δv, for 1000 $\overline{H}^+$ ions with and without the shaper. $\sigma_{d\overline{g}/\overline{g}}$ gives the relative precision for one detected event.

It should be noted that a calculation of the reflection probability as a function of the free-fall height of antihydrogen atoms on perfect mirror and mirrors made of realistic material as silicon and amorphous silica of different thickness [63] as shown in Figure 3.6 shows that for a free-fall height of ~ 0.1 mm the reflection probability ~ 90 %. Thus, to further improve the statistical precision on $\overline{g}$ as well as enhance the reflection probability on the bottom mirror the slit height can be made smaller.

In order to measure $\overline{g}$ with this scheme, the knowledge of the time spent by the atom between the shaper, t_s, is crucial to correct for the free-fall time. In the above calculations it was assumed that the knowledge of the time spent in the shaper is accurate, however, that is not true. The start time, t_0, is given by the laser shot for photo-detachment and the

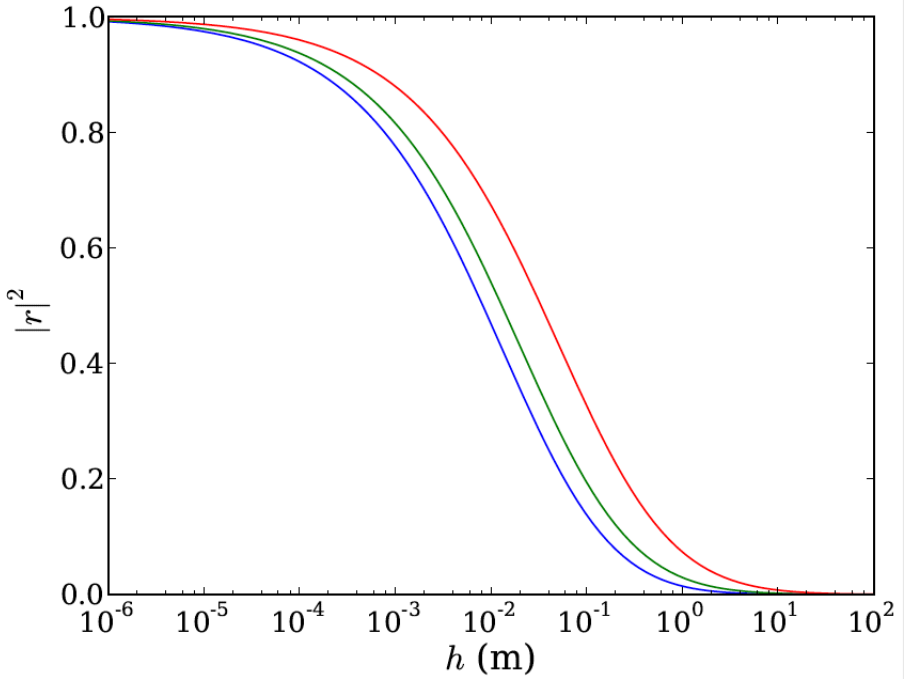

Figure 3.6: Probability of Quantum Reflection, $|r|^2$ of $\overline{H}$ as a function of the free fall height on perfect (blue), silicon (green) and silica (red) mirrors. [63]

annihilation will give the stop time, t_1. Thus, the total time of flight (t_1-t_0) = (time of free-fall (t) + time in the shaper (t_s)) can be extracted. The measurement of $\overline{g}$ thus requires the knowledge of the horizontal velocity to reconstruct the time spent by the atom in the shaper, $t_s = r_{out}/v_{hor}$, to get the actual time of free-fall, t. This sets a limit on the necessary resolution on the vertex of the $\overline{\mathrm{H}}$ annihilation on the detection plate as $v_{hor} = L/(t_1 - t_0)$ where L is the distance on the detection plate and $t_1 - t_0$ is the total time of flight as shown in Figure 3.5. The distance L is calculated from the reconstructed vertex position obtained from tracking the pions from $\overline{\mathrm{H}}$ annihilation on the free-fall cylinder. Therefore, its important to check and estimate the required and feasible resolution on the vertex reconstruction with simulation to not limit the resolution on $\overline{g}$.

Tracking modules placed around the free-fall cylinder is equipped with this task of vertex reconstruction. Detailed simulation of the above scheme was also required to further validate the estimations with simulation results. Part of this thesis, focused on the development of the Geant4 simulation in order to simulate the free-fall of the $\overline{\mathrm{H}}$ atom taking into account all the initial parameters (temperature, position, timing resolutions etc) with and without the shaper scheme and tracking the pions with the subsequent reconstruction of $\overline{g}$. The simulation results were used to estimate the expected resolution of tracking as well as it served as a guide to estimate the free-fall geometry and the required number of $\overline{\mathrm{H}}^+$ ions to reach the relative precision of 1% on $\overline{g}$. Detailed description of the simulation and the results are presented in Chapter 8.

Thus as explained above both NA64 and GBAR required development of trackers for background rejection of low energy tail of the beam for NA64 and signal detection and background rejection of cosmic rays for GBAR. The application of the trackers were quite

different in the two cases. For NA64 one required a highly efficient and precise detector capable of functioning at high rates to reach the sensitivity of the experiment and for GBAR even though the rate of signal is quite low one still requires a highly efficient and precise tracker to reject cosmic background events with high signal efficiency. For both these applications Multiplexed Resistive XY Micromegas modules were chosen due to their robust and multipurpose application capabilities. Detailed description of the detectors are presented in the following Chapter.

Chapter 4

Micromegas Detectors

In the past years, a lot of effort has been invested in the development of Microstrip Gas detectors for particle tracking in various experiments (e.g [64]). Among those Micromegas (MICRO-MEsh GASeous Structure)[65], has found many applications in particle [66], nuclear [67] and astrophysics [68] for the detection of ionising particles. This high-gain gas detector combines excellent accuracy, robustness, high rate capabilities, good timing resolution and low material budget. Furthermore, this technology found new applications eg., fire detectors [69] and muon tomography of volcanoes and pyramids [70].

4.1 Basic Principle of Operation

The working principle of all gas detectors, like the Micromegas, is to detect the hit position of particles by amplifying the ionization charge created by their passage in a gas volume. Inelastic collisions between the incident particles and gas molecules lead to excitation of the medium and ionization creating primary ionized particles, the number of which depends on the nature and energy of the radiation as well as the gas. Table 4.1 [71] shows the ionization potential ω_i and the differential energy loss, $(dE/dx)_{min}$, of some commonly used gases at NTP (Normal Temperature and Pressure) from which one can estimate the number of primary ions, N_p, produced from an incoming radiation of energy E_{in} as $N_p = \frac{E_{in}}{\omega_i}$ (assuming all energy is deposited in the gas volume) or that from an incident MIP (Minimum ionizing particle) as $N_p = \frac{(dE/dx)_{min}}{\omega_i}$/cm. The primary charge generated by ionizing radiations in the

Gas	ω_i eV/e^-	$(dE/dx)_{min}$ keV/cm
He	41.3	0.32
Ar	26	2.53
Xe	22	6.87
CH_4	30	1.61
iC_4H_{10}	26	5.67
CO_2	34	3.35

Table 4.1: Ionization potential and Differential energy loss for some commonly used gases in Gas Detectors

gas volume is collected on electrodes by means of an electric field that attracts the electrons towards the anode and the ions towards the cathode.

The choice of gas for an ionization chamber is very important. The motion of the electrons through the gas, its drift velocity and diffusion depend strongly on the inelastic collision with the gas molecules arising from its rotational and vibrational levels. The gas should not contain any electronegative component as an electronegative molecule tends to form negative ions by capturing the electrons [72]. This results in both positive and negative charge carriers as ions and thus gas multiplication will only begin at much larger voltages. Moreover, as soon as there is charge amplification, both the positive and negative ions give rise to multiplication resulting in an avalanche that never stops growing, ending in a discharge. Since oxygen is electronegative, air is not a good working gas for such chambers.

An obvious choice for the gas filling is a noble gas. A noble gas is not electronegative. It also has the advantage that the collisions of the electrons with the gas atoms are elastic below the ionisation threshold [73]. Since noble gas molecules are single atoms, there are no rotation or vibration states that can absorb the electron energy during the collisions. As a result, avalanche multiplication occurs at a lower voltage in a noble gas than in other gases. Of all the noble gases, argon is the least expensive and therefore is the choice for mostly all ionization chambers. Thus as explained the largest gains are expected with pure noble gases. However, using Argon alone is not always the practice because the multiplication process in these gases is not stable as explained below.

The cross-sections for ionization and excitation have roughly the same order of magnitude at electron energies beyond the inelastic thresholds. Therefore, a comparable number of ionization and excitation occur. In noble gases, the excited states, which mainly concerns outer shell electrons, directly transition to the ground state via the emission of photons [74] with an energy in the UV range [75]. The UV photons can release new electrons from the gas molecules or from the detector electrodes by the photo-electric effect [76]. The new electrons initiate secondary avalanches, leading to detector instability and eventually to detector breakdown. The fate of the UV photons is thus very important for the detector stability and partly determines the maximum gas gain. It is desirable to stop them as early as possible. Molecular gases, e.g., CO_2, CF_4, have absorption bands in the UV range [77] [78] and are well suited for this task. They are generally mixed with noble gases to stabilize the avalanche process (so-called quenching gases or quenchers). Various quenchers mixed with Ar, Kr and Xe have been studied and are reported in [79] [80].

Adding polyatomic gases also helps achieve large drift velocities due to their large inelastic cross-sections at moderate energies. This causes a reduction of the total electron scattering cross-section as well as the electron energy which results in an increase of the electron drift velocity. Drift velocity for some commonly used Argon gas mixtures at NTP have been computed with the MAGBOLTZ program as shown in Figure 4.1 [81].

The electrodes are connected to sensitive electronics for signal processing. The number of primary electrons from X-rays or minimum ionizing particles is too small to be detected by the electronics and has to be increased in the gas by electron multiplication. The multiplication factor is called the gas gain. Electron multiplication is based on the mechanism of electron avalanche. At increasing electric fields, the energy distribution of the drifting electrons extend beyond the thresholds of inelastic collisions, resulting in excitation and ionization of the gas molecules. In the case of an ionization, one electron produces an electron-ion pair and the two electrons, in turn, can cause further ionization. The number of

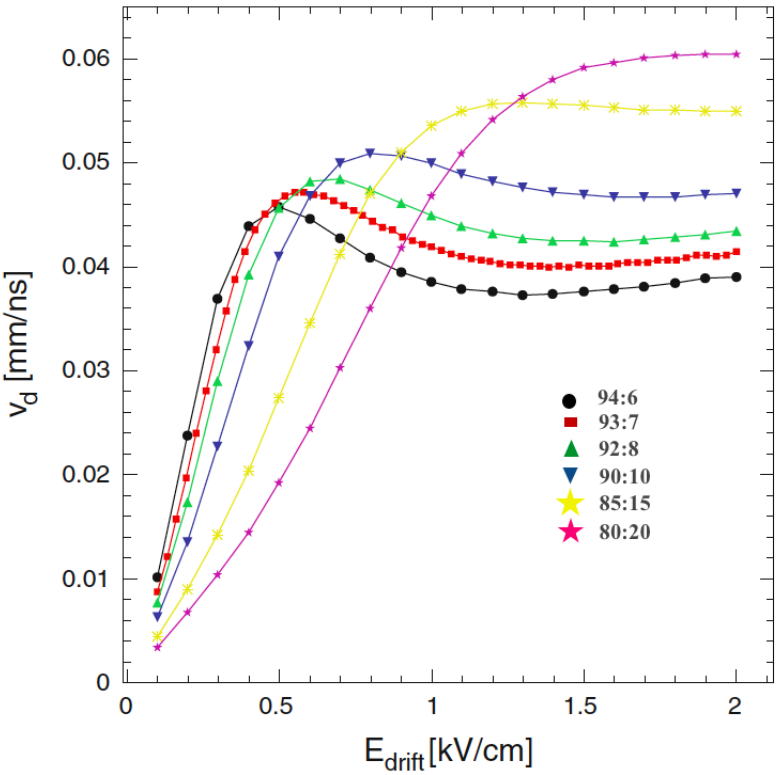

Figure 4.1: Electron drift velocity as a function of the electric drift field for various Ar:CO_2 gas mixtures at 20° C and 1.013 bar, computed with MAGBOLTZ [81].

electrons hence grows with time until all electrons are collected at the anode. At a given gas pressure, the gain is determined mainly by the gas composition and the electric field strength.

The main difference of Micromegas chambers compared to standard gas detectors is that they have a two stage gas volume, defined by a drift region of a few mm and an amplification gap separated by a thin metal grid (micro-mesh) placed a few 100 μm from the readout strips as shown in Figure 4.2. This two stage amplification allows for a high gain of $\sim 10^4$ and a fast signal of $\sim$ 100 ns, defined by the drift distance and the velocity, with good spatial resolution of a few hundred microns (depending on the strip pitch $\sigma \sim \frac{strip_{pitch}}{\sqrt{12}}$) due to the localization of the ionization cloud avalanche. The ionized charge is collected on the readout strips which is read and amplified by the readout electronics to give the signal information of hit. Thus Micromegas detectors prove to be a highly efficient and low material budget tracking detector.

4.2 Improvements to Micromegas technology

Various developments to this detector have continued since its first conception to make it more efficient. One such development to this technology was the introduction of resistive strips for spark protection in high flux environment and genetic multiplexing to connect multiple strips to each readout channel thus reducing the required number of channels as is a requirement of various experiments requiring large scale tracking detectors. The two technologies are explained in detail in the following sections.

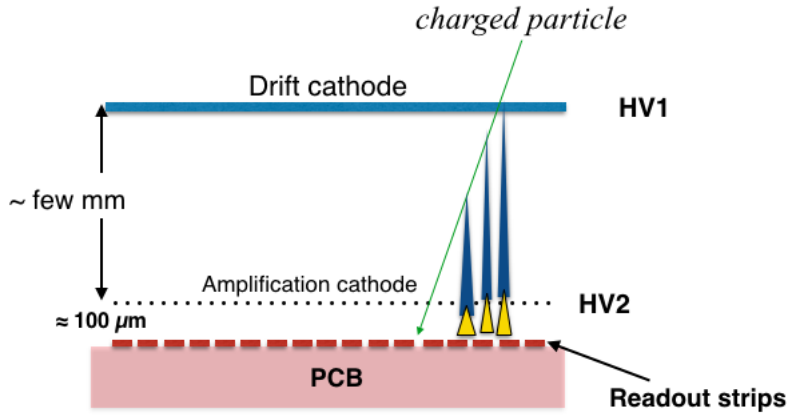

Figure 4.2: Sketch of the Micromegas chambers

4.2.1 Resitive Layer

The specific properties of Micromegas chambers, with a very thin amplification region, makes them particularly vulnerable to sparking. Sparks occur when the total number of electrons in the avalanche reaches values of a few 10^7 (Raether limit [82]). High detection efficiency requires high gas gain of the order of 10^4 which in a high flux beam environment increases the risk of sparking. Sparks may damage the detector and readout electronics and/or lead to large dead times as a result of HV breakdown. This called for the development of spark-resistant Micromegas modules. Introduction of a resistive anode (strips), by adding a continuous RC circuit on top of the readout strip plane, leads to spreading of the charge. A layer of resistive strips on top of the readout strips will thus slow down the spark development and reduce the drop in voltage and hence the dead time [83]. The resistive strips are connected to the ground through a resistor. They are not directly above the standard strips but a thin insulating layer is between them and the readout strips. In this configuration, sparks are neutralized through the resistive strips to the ground. The principle of operation of Micromegas is thus slightly modified. The signal is not read directly by the copper strips anymore. The electrons (and thus charges) are collected on the resistive strips and the electrical signal is generated via a capacitive coupling between the resistive and the readout strips. The layer in between plays the role of the insulator in a standard capacitor. Figure 4.3 shows the equivalent circuit [84] of Resistive Micromegas. R1 is the resistance between the

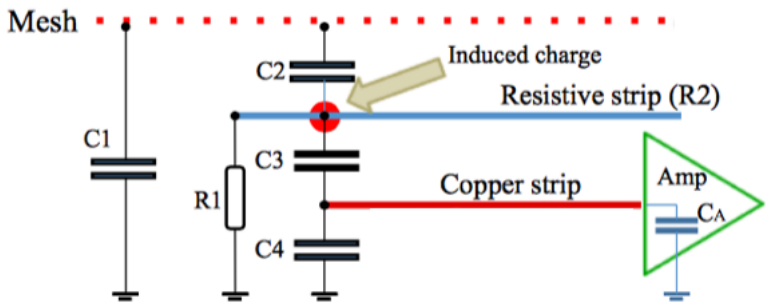

Figure 4.3: Electrical equivalent circuit of a resistive Micromegas taken from [84]

resistive strip and detector ground. C1 is the capacitance between the mesh and the detector ground. C2 and C3 are the capacitances between the resistive strips and the mesh, and the resistive and readout strips respectively. Their values depend on the spread of the charge on the resistive strips, the relative distances of the resistive strips to the readout strips and to the mesh, and on the value of the dielectric constant of the insulating material between the resistive strips and the readout strips. A higher resistivity results in a smaller spread of the charge and therefore smaller capacities C2 and C3. Their ratio, however, remains constant. C4 is the capacitance between the readout strips and the detector ground. CA represents the input capacitance of the pre-amplifier. Resistive micromegas chambers with different resistivity values were successfully tested and the results showing stable operation of the chambers at high rates are presented in [84].

Figure 4.4 shows the general schematic for a 2D resistive Micromegas module. The Y strips are placed below the Resistive strips (R-strips) and perpendicular to it. The X strips follow the Y strips and are placed parallel to the R-strips. Each layer is separated by an insulating layer. Prototypes with different widths of R-strips were studied by the MAMMA collaboration in context of R & D work to obtain a detector able to deal with the HL-LHC conditions [85]. The results from the study showed the optimum scheme of operation is with similar width X and R strips and thinner Y strips to compensate the weaker capacitive coupling to the X strips. The Micromegas modules designed for the NA64 and GBAR experiment benefited from all these previous studies to produce an efficient and precise tracker capable of handling the high flux NA64 beam as well be efficient for the low signal rate of GBAR.

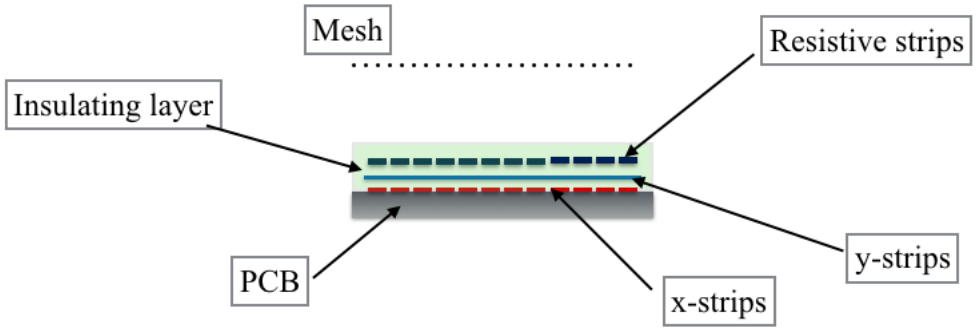

Figure 4.4: General schematic for a 2D Resistive Micromegas module showing the arrangement of the readout strips with the R-strips

4.2.2 Multiplexing

Due to the large scale of tracking detectors in most experiments and the requirement of excellent spatial resolution with small strip pitch the number of readout channels often get too high. In order to make this more cost efficient without compromising on the spatial resolution an innovative technique for the readout was proposed by Sebastien Procureur et al [86] to connect multiple strips to each readout channel thus reducing the required number of channels. The term "genetic multiplexing" was coined to name the method of grouping several readout strips to a single electronic channel, as a means to reduce the size and the cost of the electronics, which is a desired advantage of various experiments (eg. in [87]). In Micromegas detectors, and more generally in any MPGD, a particle usually leaves a signal on several neighboring strips. The main idea is to exploit this feature of strip detectors. For a

case that two neighboring strips i and i+1 are connected to two given channels a and b, and each of these channels is in turn connected to several other strips, the connection is made in such a way that there is only one set of two consecutive strips for a given set of two channels. Therefore if a signal is recorded only on channels a and b, it is almost certain that it results from the passage of a particle close to strips i and i +1. It can be generalized to the case where a signal is recorded on k neighboring strips, where k>2. The term genetic multiplexing was chosen for the analogy with DNA and genes of uniquely coding the position of the particle in the detector by the sequence of fired channels.

Though the idea of genetic multiplexing is relatively simple, constructing an optimal channel-strip connection is not trivial. Given a detector with n strips, to be read by p channels, the connection should be made such that no two consecutive strips are connected to the same channel and any unordered doublet (or k-uplet in case of a signal being recorded on k strips) of channel numbers should appear only once. The theoretical maximum number of readout strips that can be read by p electronic channels is thus given by the combinatorial formula of the maximum number of unordered doublets as [88]

$$n_{max} = \frac{p \times (p-1)}{2} + 1 \quad \text{p=odd} \tag{4.1}$$

$$n_{max} = \frac{p \times (p-2)}{2} + 2 \quad \text{p=even} \tag{4.2}$$

However this grouping may lead to fake combinations of "ghost" clusters especially in high flux beam when particle pile-up is more likely or for large cluster sizes when the signal spread give rise to smaller fake clusters. Also grouping several strips to one channel leads to larger detector capacitance, especially for larger modules, and hence limits the S/N ratio for the signal. Hence, this technology was only tested for cosmic ray events [89] until now. A solution to limit this level of ambiguity by using additional information such as the induced charge spread was proposed in [86] but its proof of principle was never tested. In this thesis we present the first results of performance of a Multiplexed Resistive XY Micromegas module multiplexed by a factor of 5 in a high flux beam in context of the NA64 experiment using a "cleaning" algorithm of these fake combinations by exploiting the additional information of cluster size and integrated charge of signal clusters. Detailed description of the NA64 experiment alongwith the description of the multiplexed modules, the cleaning algorithm and the results from the NA64 beam time are presented in Chapters 5 6.

Chapter 5

NA64- Experimental Setup and Design Considerations

5.1 Experimental setup

NA64 is a fixed target experiment searching for dark photons from the interaction of electrons dumped against an active target (ECAL). Detailed setup of the experiment is shown in Figure 5.2. The 100 GeV/c electron beam entering the setup is triggered by the co-incidence of scintillators S1-S3. The signature of the experiment being missing energy downstream of the ECAL requires precise knowledge of the incoming beam and a completely hermetic detector. The experiment employs the H4 beamline at the CERN SPS as shown in Figure 5.1, using the 100 GeV/c electron beam at a maximal beam intensity of 3.3×10^5 e^-/sec/cm^2. The tracker modules (MM1-4) as shown in Figure 5.2 track the incoming beam deflected under the integral magnetic field of $\sim$ 7 T.m over two 2 m MBPL magnets to precisely reconstruct the incoming beam momentum. Four Multiplexed Resistive Micromegas detectors were designed and built for this purpose. In order to identify the incoming electron and suppress beam contamination of pions, kaons and muons, which is a source of background for the experiment, synchrotron radiation of the deflected beam was detected by BGO crystals and Pb-Sc sandwich calorimeters. Design, procurement, software development and efficient functioning of the tracker modules was one of the main aims of this thesis. The analysis of the synchrotron radiation detection and its validation with Monte Carlo was also part of the work of this thesis. All other sub-detectors including the scintillators, Veto, ECAL and HCAL modules were designed and procured by our experiment collaborators. Detailed description of the experimental setup and the main consideration that guided the design of the sub-detectors is presented below.

5.1.1 The SPS H4 Secondary Beam

NA64 is set up at the H4 beam line of the CERN SPS produced at the target T2 with an adjustable beam momentum from 10 up to 300 GeV/c, transported to the experiment in an evacuated beam line. The H4 electron beam is the best suited beam of the SPS beamlines at high energies with the lowest contamination from particles other than electrons (expected to be within a few times 10^{-2}), better defined beam spot and divergence and highest intensity electron flux. As seen from the production yield of particles as a function of their energy in Figure 5.3 [35], the typical maximal beam intensity for electrons at $\sim$ 100 GeV/c, is of the order of $3{\times}10^6$ e^- for one typical SPS spill with 10^{12} protons on target. Because of the very

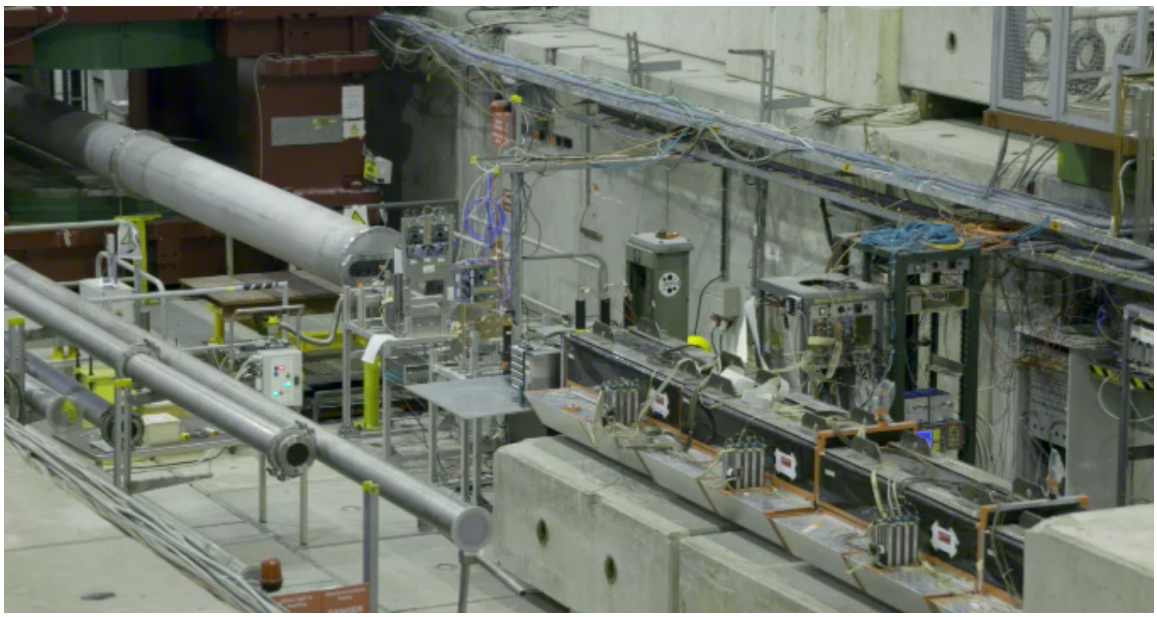

Figure 5.1: NA64 setup at the CERN H4 beamline

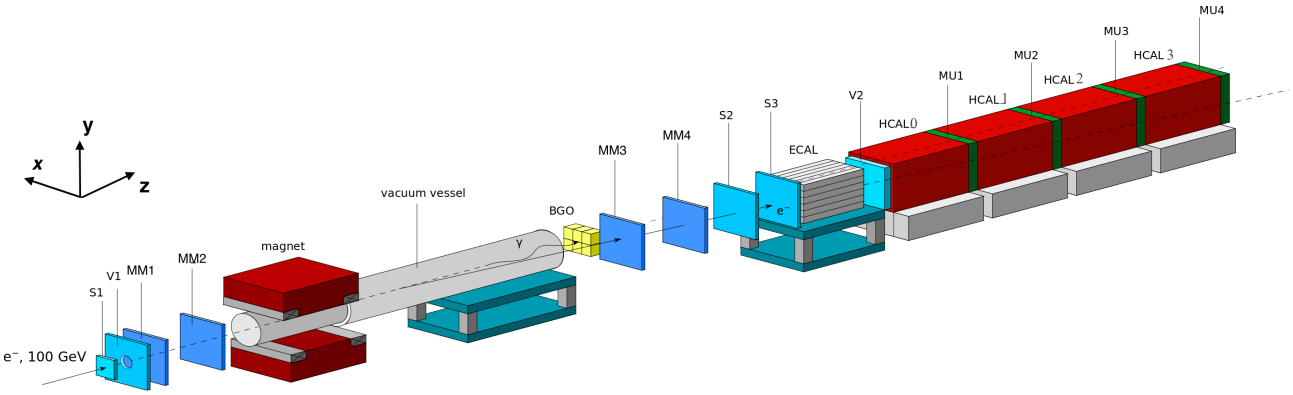

Figure 5.2: NA64 detailed setup showing all sub-detectors (taken from [26]).

high statistics required in NA64 the beam was successfully tuned to reach a intensity $\sim 5 \times 10^6$ e^- per spill with almost 4×10^{12} protons on target. A typical SPS cycle for Fixed Target (FT) operation lasts 14.8 s, including 4.8 s spill duration with the maximal number of FT cycles ~ 4 per minute. However, this number can vary from 1 to 2 per minute. The beam size at the entrance of the experiment was tuned to be ~ 2 cm diameter resulting in a maximal beam intensity of 3.3×10^5 $e^-/sec/cm^2$.

5.1.2 Trigger Scintillators

The experimental setup shown in Fig. 5.2 is equipped with scintillating counters S1-S3, read-out by PMTs, to trigger on the incoming beam that measure the time of the incoming particles with a resolution, σ_t, ~ 1 ns and an efficiency ~ 99 % [36]. The dimension of the scintillator counters are S1 - 42 mm diameter, 2 mm thick; S2 - 25 mm diameter, 2 mm thick; S3 - 32 mm diameter, 2 mm thick. A veto counter V1 160×160 mm^2, with a 40 mm diameter hole and a thickness of 20 mm is placed after S1 to veto on any halo beam particle. Thus the logic used to reject pile-up events is S1 $\times$ S2 $\times$ S3 $\times$ $\overline{\text{V1}}$.

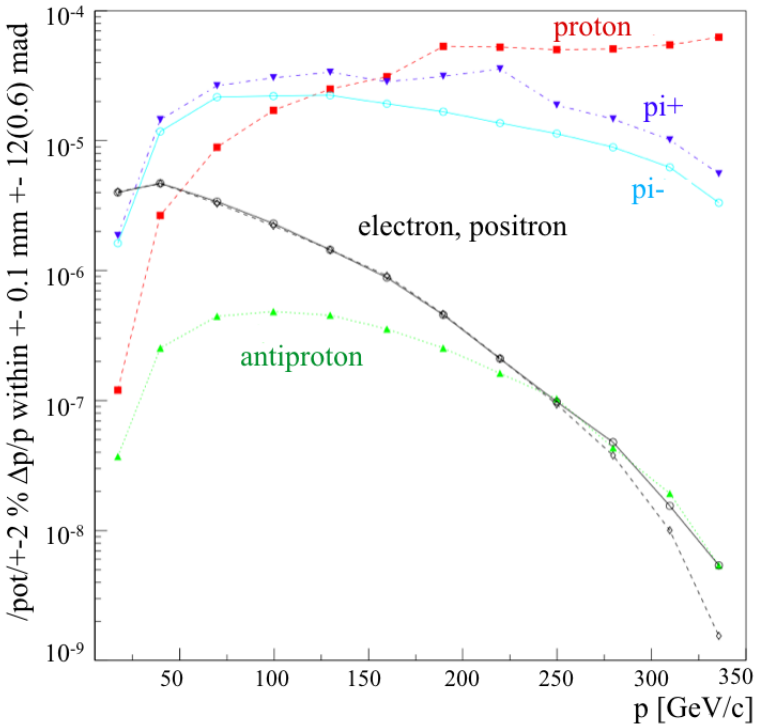

Figure 5.3: Production yield of particles as a function of their energy at the H4 beam line at the CERN SPS per proton on target at 400 GeV/c. Taken from [35]

5.1.2.1 Particle Spectrometer

Particle identification and precise tracking of the incoming momentum is crucial for the NA64 search. This particle identification and spectrometer system includes two dipole magnets ~ 2 m long, Micromegas trackers and BGO/PbSc calorimeters as synchrotron radiation detectors (SRD). The components included here was the responsibility of the ETH, Zurich group (except the magnet) and was the major part of the work of this thesis.

5.1.3 Dipole magnet (MBPL)

The 2 m long dipole magnets (MBPL) used to track the incoming beam was provided by CERN and had the maximum working field ~ 3.8 T.m over 2 m as illustrated in Figure 5.4. During the NA64 July' 2016 run the magnet system was upgraded from one to two such magnets as opposed to the case during the 2015 test beam time as is explained in the following Section. This resulted in an integral field of ~ 7 T.m thus causing ~ 35 cm deflection at the point of the ECAL ~ 15 m from the end of the magnet.

5.1.4 The BGO and fine-granularity Pb-Sc SRD detectors

A charged particle in a magnetic field moves in a circular motion emitting photons along its trajectory [99]. The total power S emitted per unit length by a relativistic charged particle of energy E with mass M and with bending radius R in a magnetic field B perpendicular to its velocity is given by:

$$S = \frac{q^2 c}{6\pi} \frac{1}{(Mc^2)^4} \frac{E^4}{R^2} \tag{5.1}$$

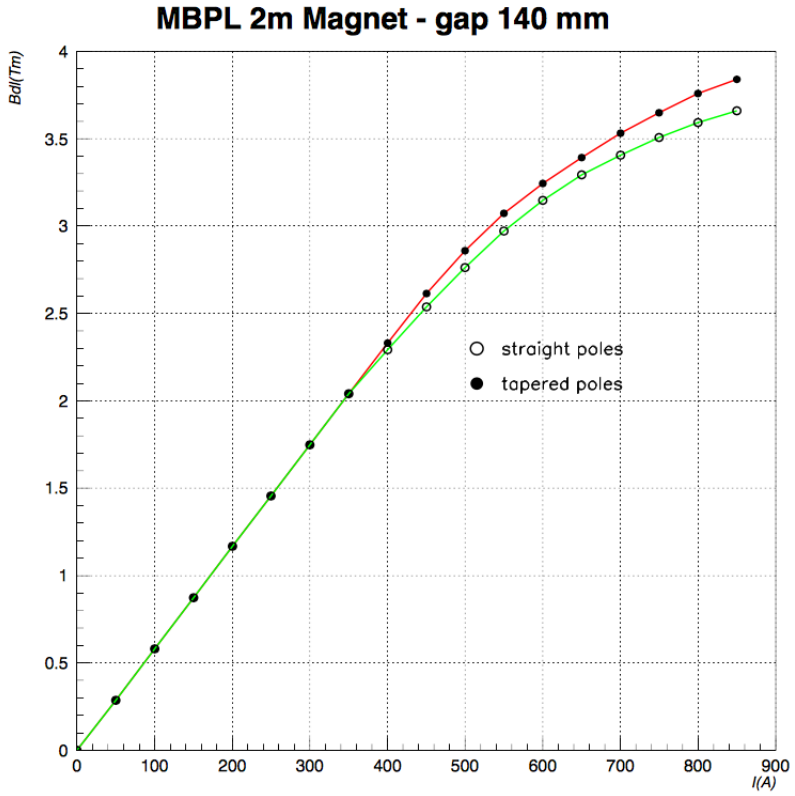

Figure 5.4: Magnetic Field as a function of the magnet current for a 2 m MBPL magnet. Taken from [35]

where q is the charge of the particle and c is the speed of light. Since the emission angle of the synchrotron photons is proportional to the inverse of the Lorentz factor γ, the photons are emitted tangentially to the particle trajectory.

The total emitted power scales inversely with the fourth power of the charged particle mass. Therefore, synchrotron radiation emitted by heavy charged particles is orders of magnitude less than light ones and can be used to suppress them. Two types of detectors were tested and used during the NA64 beam time to measure the synchrotron radiation of the incoming beam in order to suppress beam contamination from particles other than electrons as indicated in Figure 5.2. Eight hexagonal BGO crystals ($Bi_4Ge_3O_{12}$), 55 mm in diameter and 200 mm height, were arranged in rows of four by four in an aluminum box as shows in Figure 5.5. Each crystal is wrapped in a Teflon tape to limit any optical photon escape and is glued to a ETL 9954 PMT. The density of the BGO crystal is 7.13 g/cm^3 with a large atomic number due to Bismuth, Z=83, thus having a large probability of photoelectric absorption of gamma rays per unit volume [27]. The light yield of 8500 photoelectrons/MeV coupled to the quantum efficiency of the PMTs and the light collection efficiency gives an energy resolution $\sim 17\ \%/\sqrt{\mathrm{E(MeV)}}$. For a typical synchrotron radiation signal ~ 20 MeV, this results in a resolution ~ 3.8 %. In spite of the excellent energy resolution of the BGO, the main limitation of the crystals was the long decay time of 300 ns which degrades its performance at high intensities of the beam. This required upgrading the synchrotron radiation detector with a fine-granularity sandwich detector of lead and scintillator layers as shown in Figure 5.6, specially developed to detect synchrotron radiation from electrons with energy $\geqslant 50$ GeV/c. The SRD structure was finalized after careful simulation of the detector response. Three

modules, 6 cm × 8 cm each, were arranged resulting in a transverse size of 18 cm × 8 cm. The structure included 250 layers of lead (Pb), 120 layers being 0.1 mm thick and 130 layers being 0.2 mm thick, and 1.1 mm thick scintillators read out by 1 mm diameter wavelength shifting (WLS) fibers, BCF91a. The photosensors were green extended PMTs with the light yield of 20 photoelectrons/MeV.

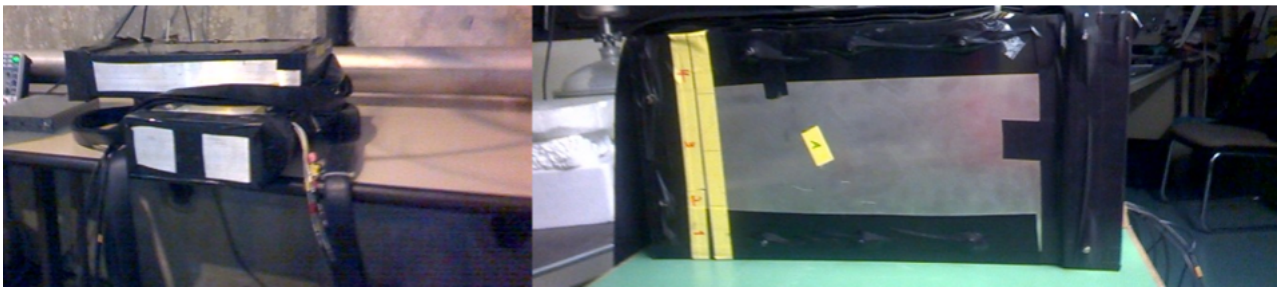

Figure 5.5: BGO modules in the aluminum box

Figure 5.6: PbSc sandwich calorimeters for synchrotron radiation detection in the beam line placed in the beamline

From Equation 5.1 it is clear that heavy charged particles like $\mu^{+/-}$ and $\pi^{+/-}$, which has about 200 e^- mass, radiate $\sim 10^9$ times less than an electron. However, this is true for ideal vacuum, unlike a real experimental setup where interactions of hadrons in vacuum windows, residual gas, beam counters etc, limit the suppression factor due to emission of secondary particles with enough kinetic energy (several MeVs) that mimics the synchrotron radiation of an electron. This was checked during the beam time and validated with Monte Carlo simulation. The suppression factor $< 10^{-3}$ obtained from the data and simulation is presented in Section 6.1.

The synchrotron radiation also scales according to the fourth power of the particle energy. Therefore, it should also be possible to measure the incoming energy of the electron from the detected synchrotron radiation as was proposed in the original proposal of NA64 [37]. However interaction of the incoming electron with the material such as beam windows, scintillators etc. or the residual gas can lead to emission of bremsstrahlung photons that can overwhelm the synchrotron radiation spectrum making it impossible to suppress the low energy electrons as was seen from the data and simulation results in the scope of this thesis. The experimental setup was simulated with Geant4 with the quoted magnetic field and the energy detected at the point of the synchrotron radiation detectors was checked. Figure 5.7 shows the true expected synchrotron radiation spectrum for different energies of the incoming electrons simulated with Geant4 and Figure 5.8 shows the actual detected energy including the bremmstrahlung contribution $\sim$ 11 m downstream of the magnet. This was also observed during the test beam time of 2015 when the BGO crystals were saturated due to this high energy contributions. During the first test beam time of 2015 only one magnet was used.

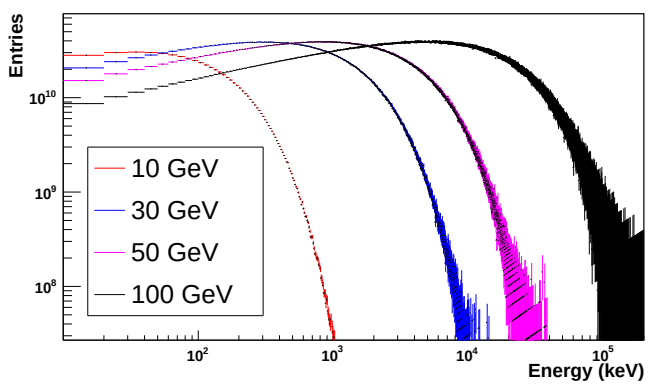

Figure 5.7: True spectrum of synchrotron radiation simulated with Geant4 for different energies of the incoming electron

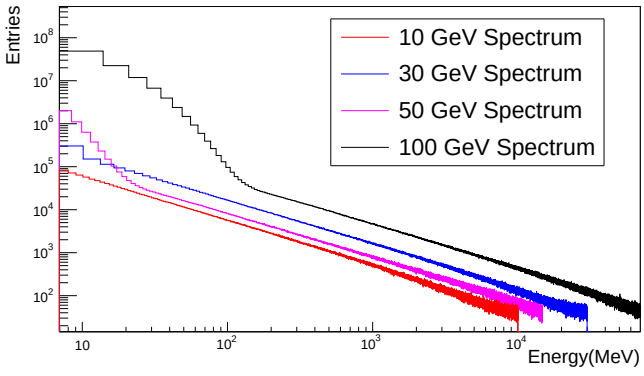

Figure 5.8: True detected energy including the bremsstrahlung photon contribution simulated with Geant4 for different energies of the incoming electron

With one magnet the deflection of the beam 11 m downstream is $\sim$ 17 cm and at high intensity it was observed an additional flux of photons coming from the beam-line was blinding the crystals closest to the primary beam axis leaving them inefficient to reject the background and also the saturation of the crystal nearest to the deflected beam suggested that some halo from the beam was able to hit this crystal. Therefore, it was proposed to increase the deflection of the beam, so the synchrotron radiation detectors could be placed in the gap between the primary and deflected beam free of any beam contribution that is prone to saturate the crystals. Indeed, it was checked with simulation that using two magnets, the deflection of the beam 11 m downstream is $\sim$ 28 cm. Figure 5.9 shows the spot of bremmstrahlung photons coming from the beam interaction 11 m downstream. As expected one spot at X = 0 comes from the bremmstrahlung contribution of the primary beam and the one at X = -280 mm comes from the bremmstrahlung contribution of the deflected beam in the beam windows. Figure 5.10 shows the synchrotron radiation spatial distribution at the same plane. Due to the uniformity of spatial spread of the synchrotron radiation it is possible to place the BGOs and PbSc detectors in the gap with low bremmstrahlung contribution and detect synchrotron radiation efficiently without getting saturated due to the primary beam. The synchrotron radiation and bremmstrahlung contribution detected on the synchrotron radiation detectors was also checked for the one magnet and two magnet configurations and

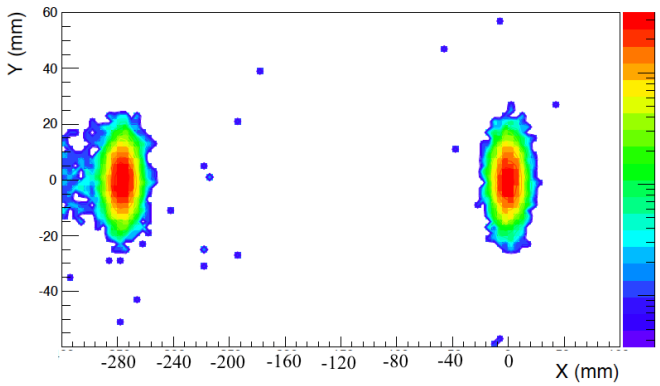

Figure 5.9: Spot of bremmstrahlung photons 14 m downstream at X = 0 due to the primary beam interactions and at X = -340 mm due to the deflected beam interactions

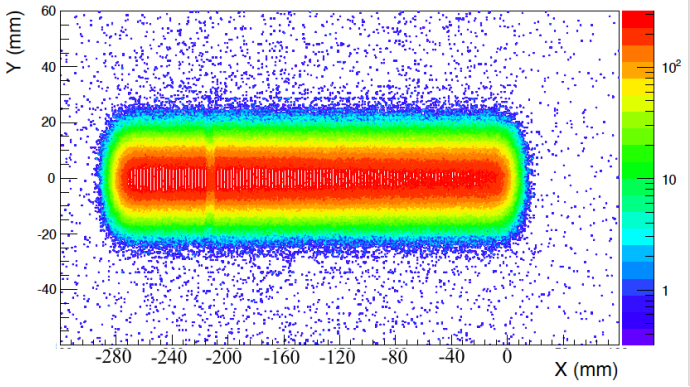

Figure 5.10: Spatial distribution of the synchrotron radiation 14 m downstream

as seen in Figure 5.11 the bremmstrahlung contribution reduces substantially with the two magnet configuration. With this configuration it was possible to reach a hadron suppression $< 10^{-3}$ with a electron detection efficiency $\sim$ 97 % during the 2016 beam time as is presented in detail in Section 6.1 as opposed to a electron detection efficiency $\sim$ 55 % for the one magnet case. Thus the simulation studies performed and analyzing the data from the first test beam time in 2015 helped finalize the two magnet geometry for the 2016 beam time, and two 2 m magnet was used as mentioned before. Since reconstruction of the incoming electron energy is not possible with synchrotron radiation detection as explained above at the level required by the experiment, the experimental setup was equipped with a tracker to track the incoming particles.

5.1.5 Micromegas Trackers

Any charged particle with momentum p entering a magnetic field, B, is deflected under the field, with the motion of the charged particle described by the equation $p = qBr$ where q is the charge of the particle and r is its radius of curvature. Four Multiplexed XY Resistive Micromegas detectors (MM1-MM4) provides the XY projection of hits of the incoming particle to reconstruct its radius of curvature under the known integral magnetic field $\sim$ 7 T.m over two 2 m long magnets. Two modules were placed before the magnet $\sim$ 1 m apart and two downstream $\sim$ 12 m from the end of the magnet before the ECAL. MM3 and MM4 were placed $\sim$ 2 m from each other (see Figure 5.2). Schematic of the Micromegas detectors used for the NA64 experiment is shown in Figure 5.12. The modules used have a drift gap of 5 mm separated from the amplification gap by a Nickel electro-formed micro-mesh. The drift cathode is made of a copper mesh and the amplification gap of 128 μm is defined by photo-resistive pillars 300 μm in diameter, equally spaced by 5 mm. The amplification mesh is formed of 400 wires (per inch) with an aperture size $\sim$ 45μm and wire diameter $\sim$ 18μm. The thickness of the mesh is $\sim$ 29μm. The gas chambers are filled with a mixture of Ar-CO_2 (93-7 %).

The secondary electrons from the ionization of the gas by the primary incident particle drift towards the micro-mesh under the electric field of the drift cathode, $\sim$ 0.6 kV/cm, wherein it enters the amplification region producing an avalanche of secondary electrons under the high

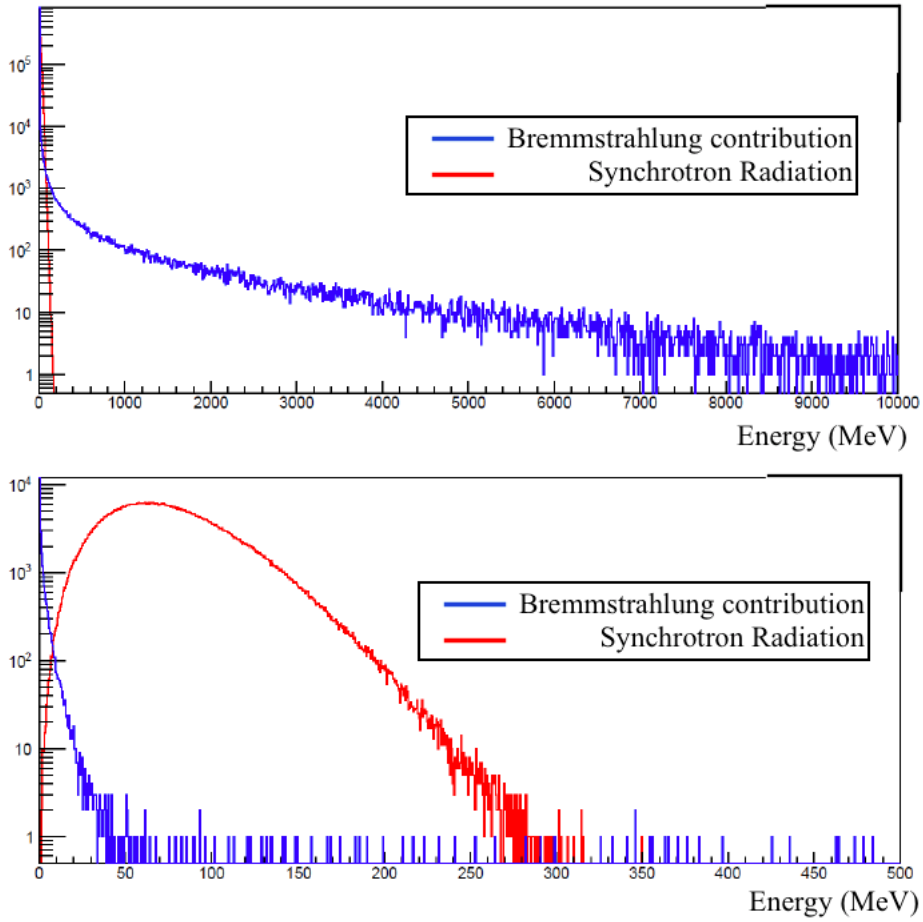

Figure 5.11: Comparison of detected energy/event due to bremsstrahlung and synchrotron contribution in the BGO crystals for single magnet (plot on the top) and double magnet geometry (plot on the bottom) from MC simulation with 100 GeV/c e^- as primaries. The range in the second plot is adjusted to highlight the high bremsstrahlung suppression in this second geometry

amplification field $\sim$ 50 kV/cm. The choice of gas for these modules was a mixture of Argon (noble gas) and CO_2 (93-7 %). The CO_2 serves as the quencher as is described in Section 4. The electrons from the avalanche produce the signal induced on the readout strips which are read by the front-end chips. Several resistive micromegas chambers with two-dimensional readout have been tested in the context of the R & D work for the ATLAS Muon System upgrade [90]. The results from this R&D work [91] on several 2D Micromegas chambers with spark protection guided our design of the strip widths and pitch for the NA64 modules. The resistive detectors used were produced at the CERN EP-DT-EF workshop and the readout strips are multiplexed by a factor 5. The resistive strips (R strips) of resistance 1 $M\Omega$ are placed parallel to the X-strips as shown in the left picture of Figure:5.12. The R and X strips have the same width of 200 μm with the Y strips placed after the R strips and perpendicular to it with a width of 50 μm. The pitch of all the strip layers is 250 μm.

The multiplexing of the modules by a factor 5 was done based on the multiplexing algorithm described in Section 4. The Micromegas modules used have an active area of 8 cm $\times$ 8 cm, with 320 strips each for the X and Y co-ordinates given the strip pitch. For the readout a 128 channel APV chip (decribed in Section 5.1.9) [92] is used, same as the ones used for the COMPASS GEM and Micromegas detectors [93]. The maximum number of strips that

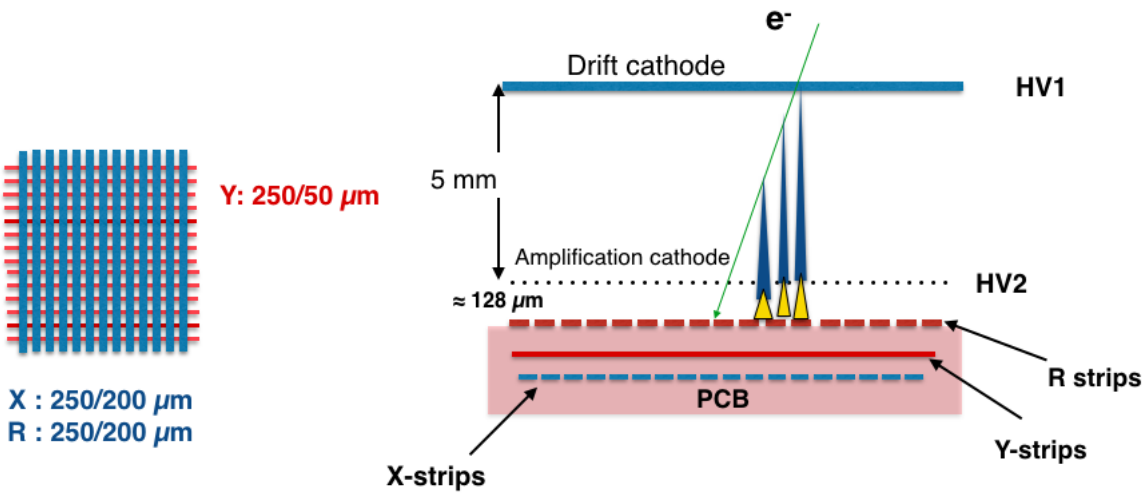

Figure 5.12: Left: Dimensions of the strips used in the Micromegas modules. Pitch of the strip layers used was 250 μm. Right: Principle of operation of a Micromegas Detector.

can be multiplexed to be read by the 128 channel APV chip theoretically is $\sim$ 8066 as per Eq 4.2. For the NA64 modules this multiplexing factor was reduced to 5, to limit ambiguities expected at high intensities and to read a total of 640 strips, on both X and Y plane, with 128 readout channels, having one chip/detector for the readout. The 320 readout strips per plane requires 64 electronic channels to be read. The multiplexing formula used to obtain the channel-strip ($c(s)$) mapping per plane where $c(s)$ is the channel corresponding to strip s is:

$$c(s) = \text{mod}(s \times (\text{floor}(s/p) \times m + 1), p) \tag{5.2}$$

where p is the number of electronic channels = 64, m=6 and mod and floor are the modulo and the rounding down functions. m gives the maximum cluster size which does not lead to repetition of at least two consecutive strip connections. The above equation is, however, only valid when p and $m + 1$ does not share a common prime factor. Figure 5.13 shows one of the Micromegas module setup at the CERN SPS H4 beam line.

In order to estimate the low energy beam tail rejection with Micromegas tracking, simulations were performed with Geant4 to estimate the resolution of momentum reconstruction and background suppression. Due to the unknown level of the low energy tail of the beam it is not possible to perform a precise and detailed simulation of this background suppression. However, based on the conversations with Ilias Efthymiopoulos of CERN SPS, the values $\sigma_{div} \sim 0.3$ mrad for the spread in the beam divergence and a beam diameter of 2 cm was used for the simulation. The values agreed with the observations during the beam time. A 100 GeV/c beam with a low energy tail as shown in Figure 5.14 (left) was simulated with the entire beam setup except the Veto and HCALs and the reconstructed momentum was checked as a function of the particle energy at the point of the ECAL. In this simulation the interaction of the particle with the ECAL was not included to save computation time. This helped estimate the level at which the reconstructed momentum matches the energy of the particle entering the ECAL. Figure 5.14 (right) shows the reconstructed momentum as a function of the true particle energy at the point of entrance to the ECAL. 10^{10} events were simulated and as seen the reconstructed momentum matched well with the particle energy with no background events with Reconstructed momentum $>$ 50 GeV/c and ECAL energy $<$

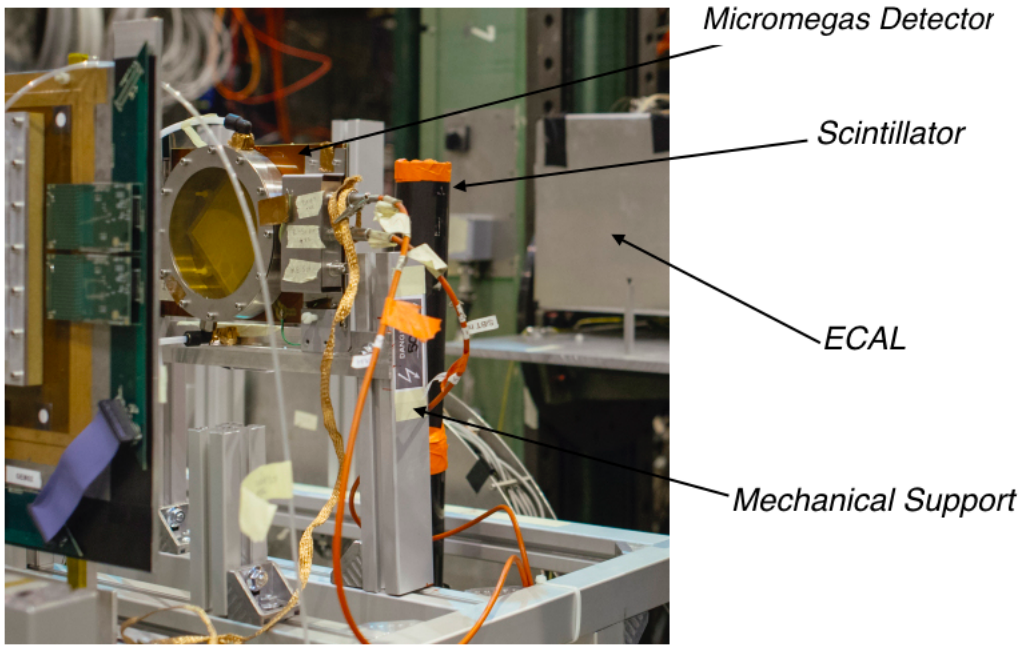

Figure 5.13: Micromegas detector placed in the CERN SPS H4 Beam line.

50 GeV/c, given the threshold of the experiment is set at $E_{miss} > 50$ GeV/c. Thus the background suppression of the low energy tail with momentum reconstruction was checked at a level $< 10^{-10}$. Accumulating more statistics required much longer simulation times and was not practical. The resolution of the reconstructed momentum was also checked with

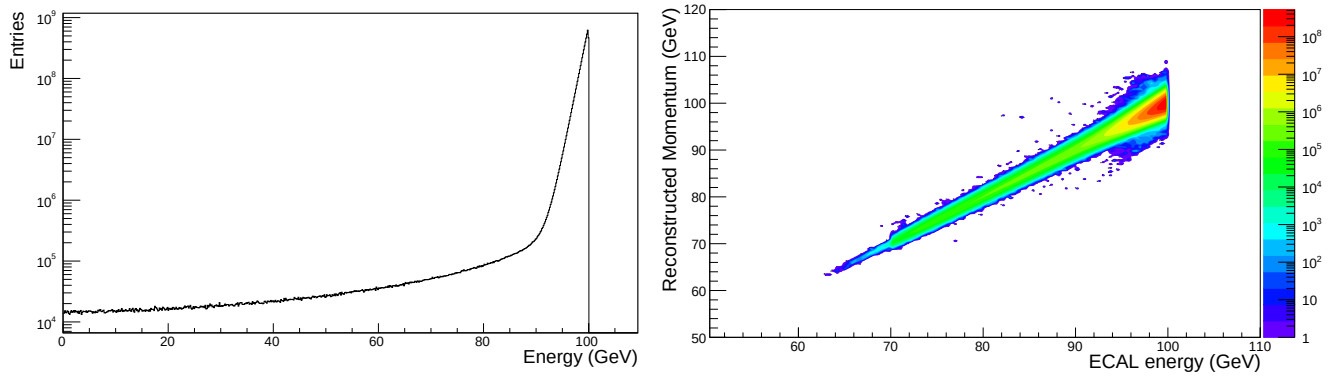

Figure 5.14: Left: Primary Energy spectrum for the simulated beam energy to estimate background suppression of the low energy tail with tracking. Right: Reconstructed momentum as a function of the particle energy at the point of the ECAL. No background events with Reconstructed Momentum > 50 GeV/c and ECAL energy < 50 GeV/c at a level $< 10^{-10}$

simulation and a resolution ~ 1 % for a 100 GeV/c beam was achieved which agreed well with the data from the 2016 beam time as is presented in Section 6.2.

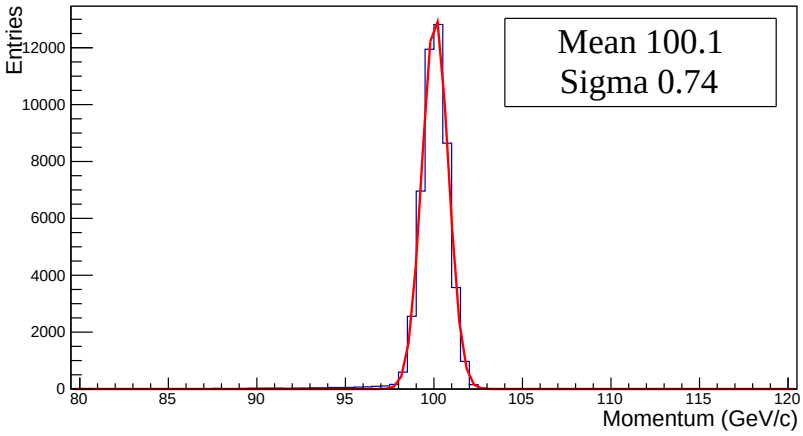

Figure 5.15: Reconstructed momentum for a 100 GeV/c beam with simulation. Resolution ∼ 0.7 GeV/c ∼ 1 % for a 100 GeV/c beam

5.1.5.1 Gain Calibration

Micromegas trackers are characterized by their gain defined as the total number of electrons produced after amplification, per single incident electron in the gas volume as G = $\frac{N_{total}}{N_{prim}}$, where N_{prim} is the number of electrons liberated from ionisation of Argon in the drift region and N_{total} is the total number of electrons after the amplification. The gain is thus a function of the amplification voltage and the modules were first tested to estimate their optimum working voltages in a gas mixture of Ar-CO_2 (93-7 %). In order to characterize the gain the total current on the Resistive strips was measured with a radioactive Fe source in the laboratory for different amplification voltage. The number of primary electrons is directly related to the nature of the gas and the energy of the incoming particle, E_x =5.9 keV for ^{55}Fe, as $N_{prim} = \frac{E_x}{\omega_i} = 223$ e^-, where $\omega_i = 26.5$ eV/e^- is the ionization potential of Ar-CO_2 (93-7 %) [104]. Figure 5.16 shows the setup used for the calibration, wherein the drift and the R-strips (Resistive strips) were connected to a high voltage of polarity negative and positive respectively through a RC filter and the mesh was grounded through a resistance. The readout strips were grounded through the readout chip attached as shown. The mesh signal was monitored via a oscilloscope connected through a preamplifier powered by a timing amplifier. The integration time of the signal was selected given the signal rise time which is a function of the drift distance and the drift velocity of the ionising particle as $t_d = d/v_d$ where $d = 5$ mm is the drift distance and $v_d = 5$ cm/μsec [103] is the drift velocity. Thus the rise time comes out to be ∼ 100 ns. The drift voltage and the R-strips were powered using the N471A power supply from CAEN which was also used to monitor the current on the connected channels. The drift voltage was set at -300 V and the total current on the R-strips was read on the power supply for different amplification voltage applied. So the gain of each detector was calculated by measuring the total current on the strips taking into account the rate of interaction which was measured to be, $r \sim 14$ kHz as

$$G = \frac{I}{r \times q \times N_{prim}} \tag{5.3}$$

where I is the measured current on the R-strips for the given voltage, q is the electron charge and $N_{prim} = 223$ e^- is the estimated number of primary electrons due to the source. The gain obtained as a function of the amplification voltage is shown in Fig. 5.17 for one module. The

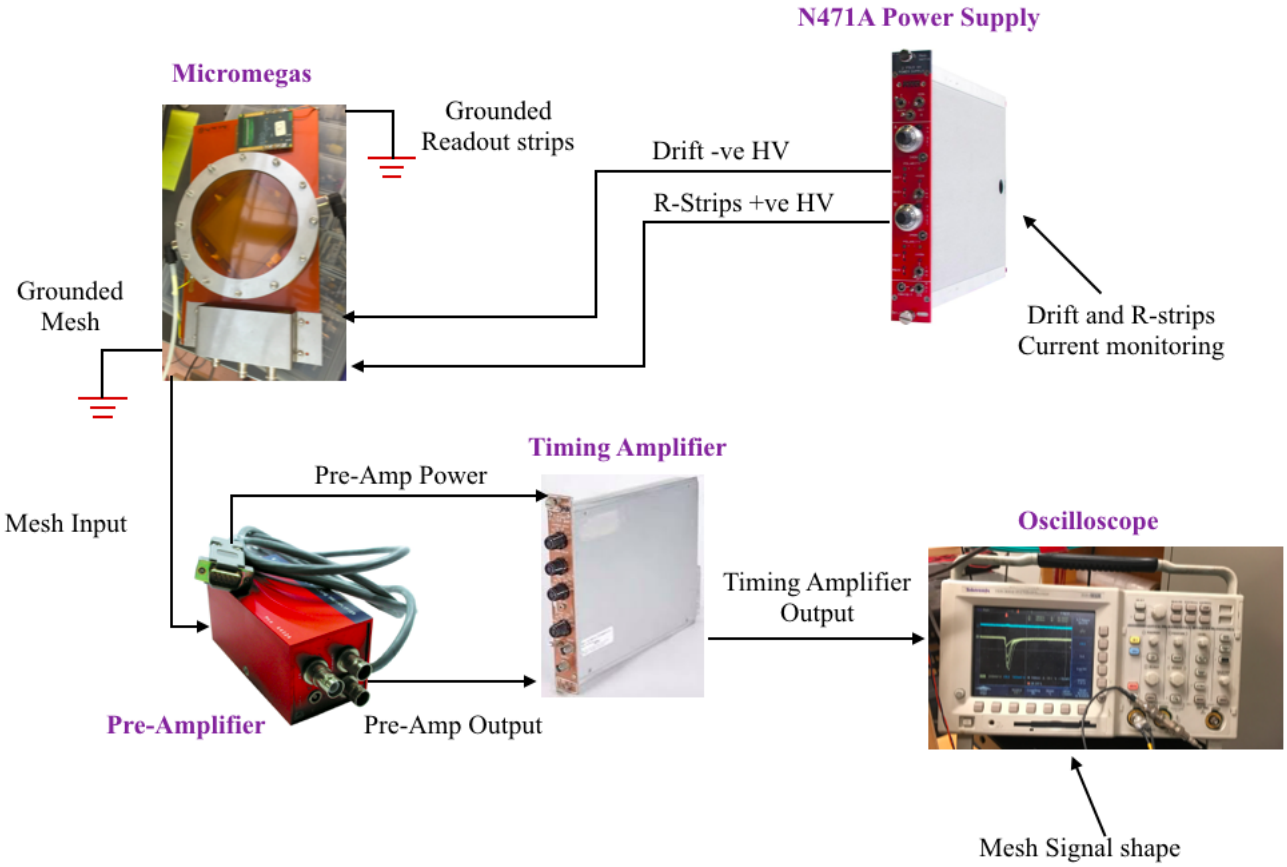

Figure 5.16: Laboratory setup for the gain calibration of the Micromegas modules

amplification voltage was kept below the spontaneous breakdown voltage limit observed of 560 V and the typical gain achieved is about 3×10^4. The spontaneous breakdown occurs mostly because of the streamer mechanism in gas detectors discussed in detail in [105] [106]. After calibrating the gain of the detector the signal reconstruction from the strips was tested with the APV25 chips and the the readout software was integrated with the common NA64 DAQ.

5.1.5.2 Signal Cluster Reconstruction

The Micromegas modules are read by the APV25 readout chips as described below. When the trigger from the experiment is received, the chips output for each channel three analog charge samples separated by 25 ns. Those signals are digitized by the ADC and are read by the common DAQ [107] of the experiment.

The pedestal distribution of the electronic channels, obtained from the average of the three charge samples/channel, are recorded in absence of the beam in the latch-all mode of the ADC. The noise is defined as the RMS fluctuation (sigma) of each channel around its pedestal. The latency is set such that the three samples lie on the rising edge of the signal with the third sample closest to the peak. A hit on a strip is defined when the third sample is at least three sigma above the pedestal level.The maximum of the three samples is then recorded as the charge information of the hit strip. When a charged particle enters the detector it is expected to leave a signal on consecutive strips due to its drift in the gas and

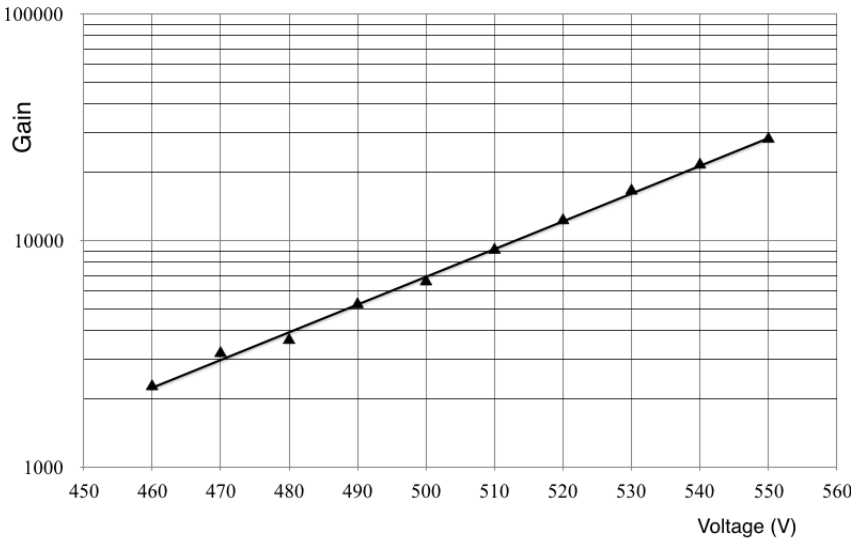

Figure 5.17: Gain of a Micromegas module as a function of the amplification voltage

the consequent charge spread. A signal cluster is defined when at least two neighboring strips are hit. To reconstruct the position of a signal cluster the electronic channels are mapped to the multiplexed strips. The hit position on each plane (X and Y) is calculated from the weighted average of the detected charge on the strips:

$$pos = \frac{\sum_{i=0}^{n}(q_i \times strip_i)}{\sum_{i=0}^{n}(q_i)} \tag{5.4}$$

where n is the number of strips in the cluster, $strip_i$ is the i-th strip of the X or Y plane cluster and q_i is the charge on the i-th strip.

5.1.5.3 Time Calculation

The timing calculation is based on the method used for the GEM detectors in the COMPASS experiment [94]. As mentioned above the APV25 chips reading the Micromegas detectors output three analog charge samples ($A0$, $A1$, $A2$) for each channel on receiving the trigger. The latency is adjusted such that the three samples, saved in case of a trigger, sit on the rising edge of the signal for most of the time. With precise knowledge of the signal shape it is possible to thus calculate the time the particle crossed the strip with respect to the trigger and the timing information of the strips in the signal cluster help reconstruct the cluster time. Figure 5.18 shows an example of a signal sampled by the APV. To be able to describe the signal independently from its amplitude, the samples are normalized to the third sample A2 of a hit as:

$$r_{02} = \frac{A0}{A2} \quad \text{and} \quad r_{12} = \frac{A1}{A2} \tag{5.5}$$

Figure 5.19 shows an example of the plot of A0/A2 vs A1/A2 for a correct latency setting, obtained during the beam time, with the expected values of A0/A2 < A1/A2 < 1. These experimental ratios can be described well by the function [124]

$$r(t) = \frac{r_0}{(1 + exp(\frac{t-t_0}{\tau}))} \tag{5.6}$$

where r is either r_{02} or r_{12}. The three parameters defining the function are r_0 that gives the

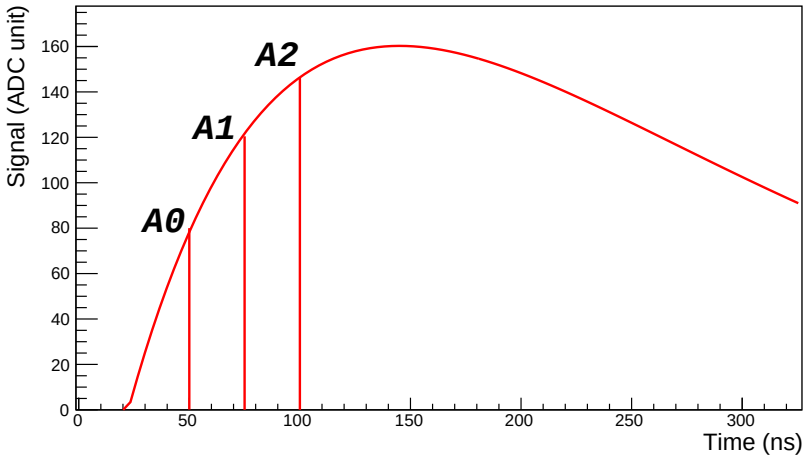

Figure 5.18: Shape of signal sampled by a APV chip indicating the three samples 25 ns apart

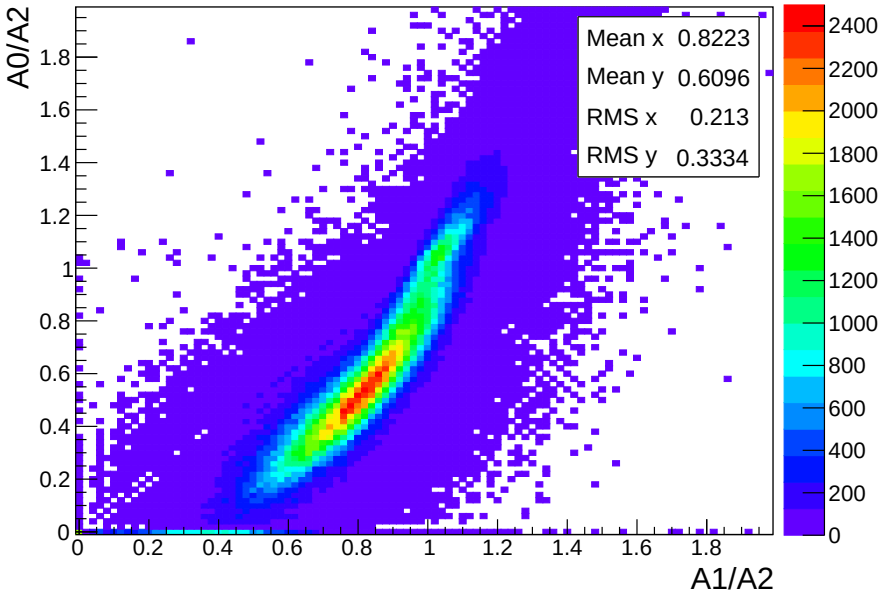

Figure 5.19: Ratio A0/A2 vs A1/A2 obtained during the beam time for a correct latency setting, with A0/A2 < A1/A2 < 1.

limit of the function for t $\rightarrow \infty$, t_0 is the time when the function reaches $r_0/2$ and τ describes the slope at t_0. With these definitions τ will always be negative. These parameters have to be fitted to the experimental data of calibration runs and then used to reconstruct the time of hits.

5.1.5.4 Time Calibration

The functions describing ratios r_{02} or r_{12} are used, as usually the third sample has the largest amplitude and thus times reconstructed with it will have a smaller error. To be able to describe the function of Eq 5.6 over a longer time, data from latency scan runs is used for the

calibration. Data for latencies shifted by ± 75 ns with respect to the original setting was used. For calibration, beam intensity $\sim 10^4$ e$^-$/sec/cm^2 was used. The three parameters t_0, r_0 and the slope τ along-with the covariance matrix 5.7, are found by fitting with Eq.5.6 the latency scan (Figure 5.20).

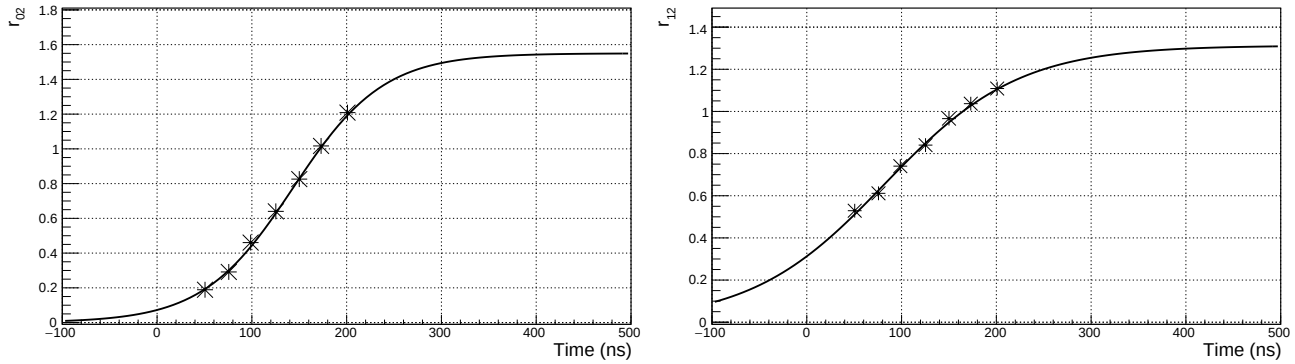

Figure 5.20: Ratio r_{02} and r_{12} as a function of the time from the mean of the fitted Gaussian of the ratios for different latency settings

$$\Sigma = \begin{bmatrix} cov_{\tau,\tau} & cov_{\tau,t_0} & cov_{\tau,r_0} \\ cov_{t_0,\tau} & cov_{t_0,t_0} & cov_{t_0,r_0} \\ cov_{r_0,\tau} & cov_{r_0,t_0} & cov_{r_0,r_0} \end{bmatrix} \tag{5.7}$$

5.1.5.5 Time Reconstruction

From the knowledge of the parameters and the inversion of Eq. 5.6 the strip hit time can thus be calculated for each ratio as:

$$t(r) = t_0 + \tau ln(\frac{r_0}{r} - 1) \tag{5.8}$$

where r is the ratio for the event (r_{02} or r_{12}). The error on the reconstructed time σ_t is given by the error on the ratio, σ_r which is a function of the amplitudes used in the ratio, and the error on the fit parameters as :

$$\sigma_t^2 = J. \begin{bmatrix} \sigma_r^2 & 0 \\ 0 & \Sigma \end{bmatrix} J^T \tag{5.9}$$

where

$$J = (\frac{\delta t(r)}{\delta r} \quad \frac{\delta t(r)}{\delta \tau} \quad \frac{\delta t(r)}{\delta t_0} \quad \frac{\delta t(r)}{\delta r_0}) = (\frac{\tau r_0}{r^2(\frac{r_0}{r} - 1)} \quad ln(\frac{r_0}{r} - 1) \quad 1 \quad \frac{\tau}{r(\frac{r_0}{r} - 1)})$$

$$\sigma_{r_{02,12}} = (\sigma_n + \frac{1}{\sqrt{12}}) \frac{\sqrt{A(0,1)^2 + A2^2}}{A2^2}$$

σ_n is the σ of the pedestals of the channel reading the strip in the signal cluster. The additional $1/\sqrt{12}$ factor comes from the standard deviation of a standard uniform distribution on the strip connected to the channel. The calculations give two times per hit strip, t_{02}^i and t_{12}^i, from the two ratios r_{02}^i and r_{12}^i with the corresponding parameters and errors for the i-th strip in the cluster. The errors on the individual ratio's time $\sigma_{t_{02,12}}^i$ (for the i-th strip) is calculated for all hit strips in the cluster and the cluster time is reconstructed as

$$t = \frac{\Sigma_{i=0}^n (\frac{(t_{02}^i)}{(\sigma_{t_{02}}^i)^2} + \frac{(t_{12}^i)}{(\sigma_{t_{12}}^i)^2})}{\Sigma_{i=0}^n (\frac{1}{(\sigma_{t_{02}}^i)^2} + \frac{1}{(\sigma_{t_{12}}^i)^2})} \tag{5.10}$$

where n is the number of strips in the event cluster. Some of the strip's time may not be reconstructed, for example, if the ratio is greater than r_0 which would cause a negative argument of the logarithm. These times are not considered. But as one cluster usually consists of several hit strips, all reconstructed clusters end up with a valid time information.

5.1.6 ECAL

The $A' \rightarrow invisible$ search requires not only a precise knowledge of the incoming beam but also an accurate measurement of the missing energy from the incoming beam's interaction. The electromagnetic calorimeter is crucial to determine precisely the deposited energy from the interaction of the incoming beam in the active target and hence calculate the missing energy downstream. A shashlik ECAL as shown in Fig 5.21, with a sandwich of Lead (Pb) and Scintillator (Sc) plates was chosen for its radiation hardness, good energy resolution, and uniformity of response. The ECAL module consists of 36 cells, arranged in a 6 $\times$ 6 matrix, with each cell being 38.2 $\times$ 38.2 $\times$ 490 mm^3, consisting of 150 layers of 1.5 mm Pb + 1.5 mm Sc, resulting in a total thickness of $\sim$ 40 radiation lengths (X_0). Each cell is longitudinally subdivided into the preshower section (PS) $\sim 4X_0$ and the main ECAL $\sim 36X_0$. An unique feature of the ECAL is the spiral arrangement of the wavelength shifting fibers (WLS) to avoid energy leak. The basic performance of the ECAL was evaluated using Geant4

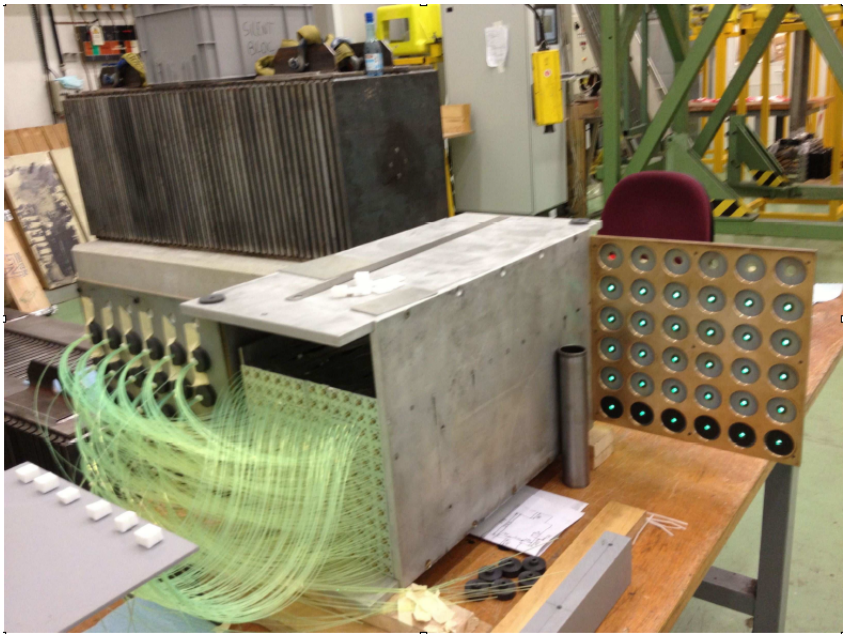

Figure 5.21: Shashlik ECAL with the spiral WLS fibers read out at the back of the detector with photomultipliers

simulation [126]. The ECAL energy resolution was checked for various absorption plate thickness keeping the scintillator thickness constant at 1.5 mm. Figure 5.22 shows the energy resolution for different beam energies and plate thickness. The results were parameterized with the relation $\Delta E/E = a/\sqrt{E} + b$ and the fit results show for the selected Pb thickness of 1.5 mm a resolution $\sim 15\%/\sqrt{E}$ is expected [29]. The ECAL energy resolution obtained with simulation was also validated with the data. The energy resolution $\sim$ 2.5 GeV/c of the ECAL obtained with the beam data shown in Figure 5.23 agrees well with the simulated value.

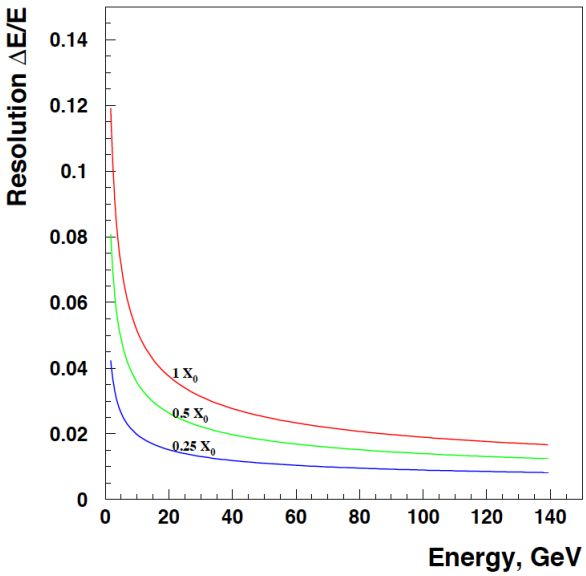

Figure 5.22: Simulated energy resolution (FWHM) as a function of the incident energy for a ECAL module, for different absorber plate thicknesses in units of radiation length, X_0, keeping the scintillator plate thickness constant at 1.5 mm. Only contributions from sampling fluctuations and energy leakage are included [37]

5.1.7 HCAL

The longitudinal hermeticity of the experimental setup is enhanced by using HCAL modules to detect charged and neutral hadrons and subsequently provide a measurement of the missing energy, not detected in the ECAL, after proper tagging of the incoming particle with the tracker and SRD modules. The HCAL is important also because the VETO cannot reject neutral hadronic final states. The HCAL comprises of four modules as shown in Figure 5.24, each consisting of 9 cells arranged in 3 × 3 matrix with a transverse dimension of 194 × 192 mm^2/cell and weighing ∼ 3500 kg/module. Each cell consists of 48 layers of 25 mm Pb + 4 mm Sc, resulting in a total of 7 interaction lengths (λ_{int}). Kyraray Y11 WLS fibers, that provide the light read-out, embedded in round grooves in the scintillator plates are collected together in a single optical connector from the 9 cells and read out by a single photomultiplier (PMT FEU-84). The longitudinal segmentation of the counter into 4 sections ensures good timing uniformity of light collection from the observed particle shower. The front-end electronics alongwith the 9 PMTs/ module are placed at the rear end of the HCAL in a box. Light Emitting Diodes (LEDs) mounted on the same box monitor the HCAL cells' response. Since the signal is characterized by "No Interaction" in the HCAL and Veto the zero energy threshold had to be checked for the detectors. In order to estimate the zero energy event threshold for the HCAL modules the energy leak distribution in the first HCAL module, HCAL0, was checked for a 100 GeV/c e^- beam with Monte Carlo and data. Figure 5.25 shows the comparison of data and Monte Carlo, which are in good agreement with each other, and as seen for a zero energy threshold set at ∼ 1 GeV/c, i.e., $E_{HCAL} < E_{th} = 1$ GeV/c the efficiency for the 100 GeV/c electrons is ∼ 100 %. Thus the HCAL energy threshold was set at 1 GeV/c for zero energy events.

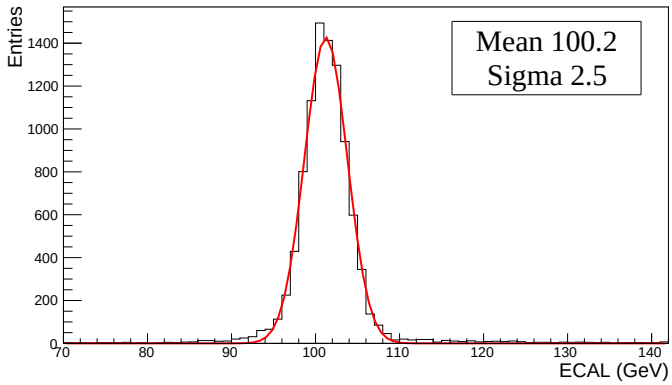

Figure 5.23: Energy distribution in the ECAL obtained from the beam data for a 100 GeV/c beam. The black histogram is data and the red line is a fitted Gaussian function with parameters "Sigma" and "Mean".

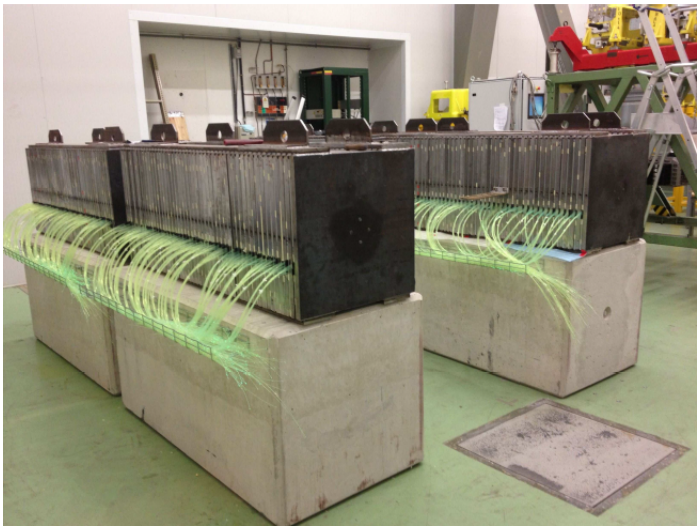

Figure 5.24: HCAL modules with spiral WLS fiber passing laterally through read out at the side of the module with PMTs

5.1.8 VETO

The main task of the veto counters placed after the ECAL is the precise measurement of time and energy deposition of particles escaping the ECAL to measure coincidence with the real electron event and reject background events from hadronic and pile-up events. The veto counters consists of three plastic scintillators, 4.5 cm thick, 17 cm wide and 51 cm long each, covering a total area $\sim 51 \times 51$ cm^2. The counters have a high light yield $\sim 10^2$ photoelectrons/MeV of deposited energy and the typical inefficiency measured for MIP detection is conservatively $\leqslant 10^{-4}$. The counters are arranged for optimal rejection of charged particles escaping the ECAL and are viewed at both ends by XP2020Q photomultipliers. The performance of the VETO was also studied and the data collected was compared with Monte Carlo simulations to establish its performance and estimate its zero energy threshold. A Muon beam was simulated and its energy deposition in the VETO was checked. In order to establish the Veto performance from data a 100 GeV/c hadron beam was tuned and the beam was triggered by the co-incidence of the Scintillators S1-S3. The energy distribution of the first module of the HCAL (HCAL0) was checked and events with energy in the range 1

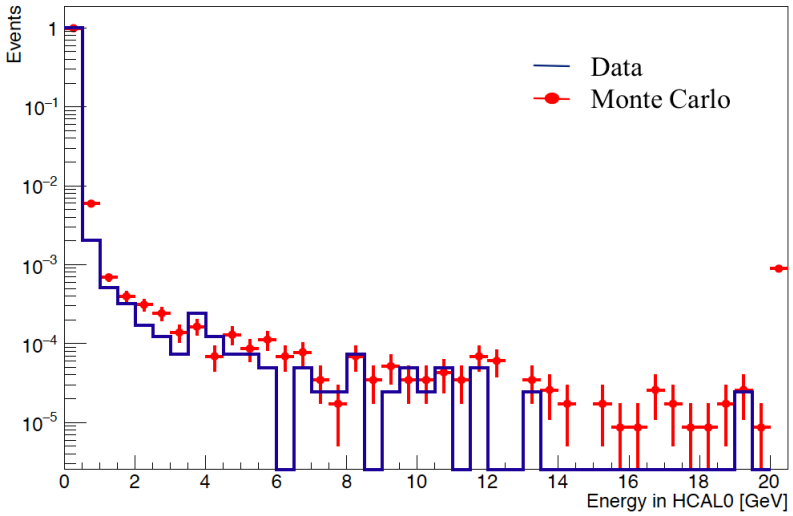

Figure 5.25: Comparison of energy leak distribution in the first module of the HCAL, HCAL0, for a 100 GeV/c electron beam with Monte Carlo and data [30]

GeV/c $< E_{HCAL0} <$ 3.5 GeV/c was selected as Muon events. Figure 5.26 shows a clear correlation of the Muon events between HCAL0 and HCAL1. Figure 5.28 shows the Muon spectrum in the Veto for Monte Carlo (left) and data (right), obtained with the simple cut mentioned above for the HCAL0 energy, which are in fair agreement with each other. In order to estimate the zero energy threshold of the VETO the energy leak spectrum for a 100 GeV/c electron beam was checked from data without any cut. Figure 5.28 shows the energy leak spectrum obtained for a beam intensity of $\sim 2 \times 10^5$ e^-/sec/cm^2. The zero energy threshold for the Veto was chosen to be $E_{th} \sim 1$ MIP (Minimum Ionizing Particle) ~ 10 MeV from the plot and as seen the signal efficiency for this cut is ~ 99 %.

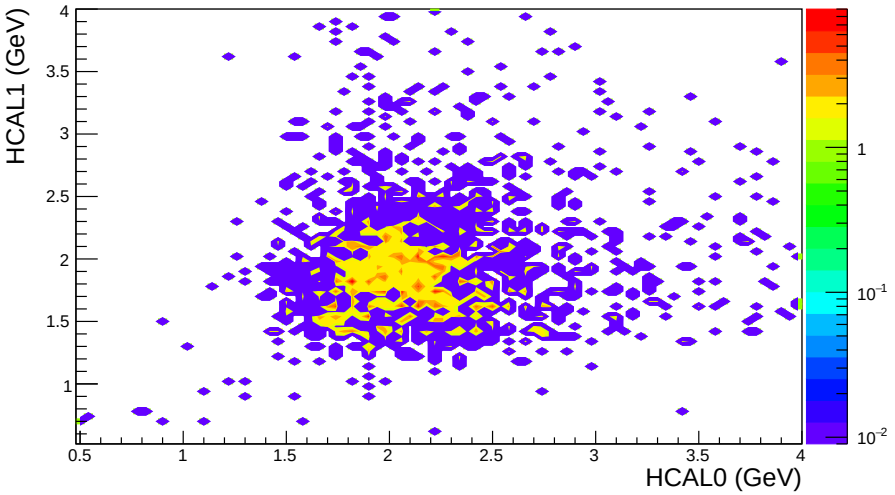

Figure 5.26: Energy in HCAL1 vs HCAL0 for a 100 GeV/c hadron beam showing clear correlation for Muon events

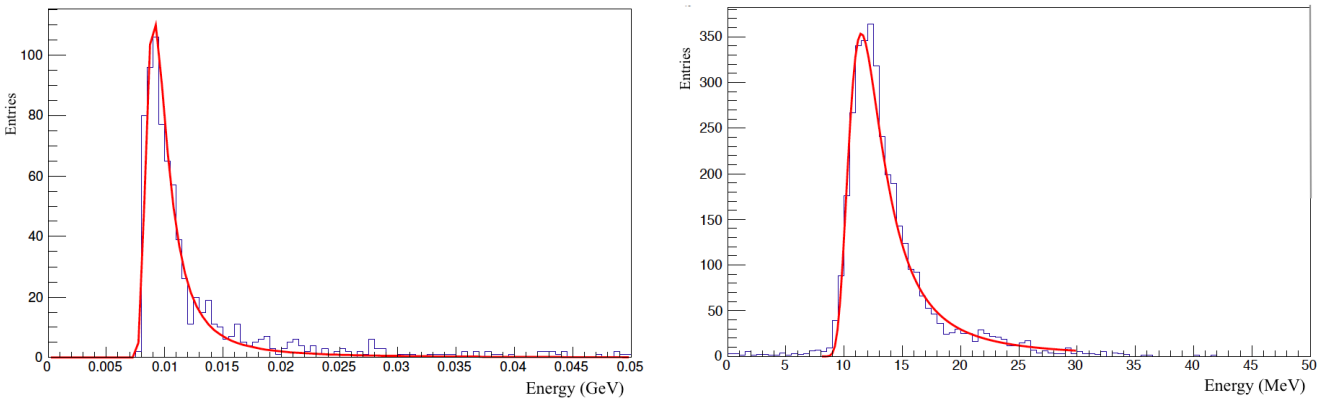

Figure 5.27: Muon Spectrum in the VETO for Monte Carlo (left) and data (right) in fair agreement with each other [31]

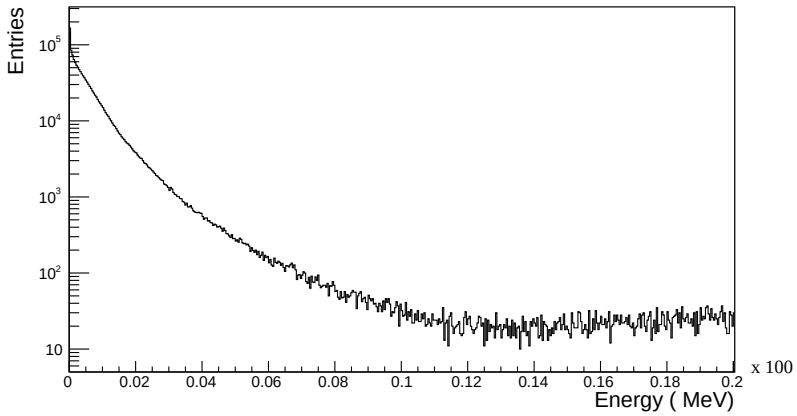

Figure 5.28: Energy leak spectrum in the VETO for a 100 GeV/c electron beam of intensity $\sim 2 \times 10^5$ $e^-/sec/cm^2$ from data.

5.1.9 Readout Electronics

The DAQ used for NA64 is a downscaled version of the COMPASS DAQ system [32]. The detector frontends are connected to the readout modules, GeSiCA (Gem Silicon Control and Acquisition) for the Micromegas modules and CATCH (Compass Accumulate Transfer and Cache Hardware) for all other detectors. The main tasks of the modules are the fast readout of the front-end boards and local sub-event building at a processing speed of up to 160 MB/s. In parallel, the modules also distribute the trigger and time synchronization signals from the Trigger Control System (TCS) to the front-end boards. Before the start of data taking, the readout modules initialize all front-end cards with the initialization data provided via VME. The CATCH, developed at the University of Freiburg, is the general readout module used nearly by all detectors, supporting a wide range of frontend electronics. In contrast, the GeSiCA module is optimised for the reaodut of APV25 frontend chip that are used by the Micromegas modules same as the ones used for the COMPASS GEM detectors [94].

The APV25 is an analogue pipeline ASIC intended for read-out of strip detectors originally developed for the CMS strip-detectors [33] [34]. It has 128 readout channels, each consisting of a 50 nanosecond CR-RC type shaping amplifier, a 192 cell deep pipeline and a pulse shape

processing stage which can implement a deconvolution operation to achieve the single bunch crossing resolution necessary at high luminosity. The pipeline is used to store the amplifier outputs, sampled at 40 MHz frequency, while external trigger decisions are taken. Data of four APV chips are digitized by two ADCs (2 chip/ADC for upstream and downstream case) which are then buffered and merged by the GeSiCAs [94]. The ADC module offers two modes of operation, the latch-all mode and the sparse mode. In the latch-all mode, the amplitudes of all channels which are sampled three times (25 ns apart) are transmitted. This limits the possible trigger rate to approximately 1 kHz due to the large amount of data. To reach higher trigger rates the sparse mode is used. Here, only data for channels which are above a certain threshold are transmitted to the GeSiCA by the ADC module. Therefore the latch-all mode is used to record pedestals of the channels and the sparse-mode is used for data and thus a data acquisition rate $\sim$ 10 kHz is achieved.

The data formatted according to the general COMPASS data format by the readout driver modules [95] are transmitted through optical fibers to high performance readout buffer PCs (ROB). The S-Link protocol [96], developed at CERN, for fast point to point connections is used. This takes place either via a single S-Link, or by combining up to four readout modules (CATCH or GeSiCA) by means of a S-Link multiplexer. The master event building system consists of the readout buffer PCs and event builder PCs. One readout buffer hosts four spill-buffers. A spill-buffer is a 512 MB RAM module which can store the data of more than one spill. A special software combines the information of the spill-buffers and transfers it via a Gigabit switch to the event builder PCs for further processing. On these computers (commercial PCs) the information of each event coming from all different ROBs is combined to the full event. From the event builders, the final events are transferred to the central data recording, where they are written to mass storage media. A detailed schematic of the DAQ is shown in Figure 5.29.

5.2 Background

The signal for the $A' \rightarrow invisible$ channel requires an event coincident in time in the scintillators S1-S3, a fraction of the incoming beam energy, $f\mathrm{E}_0$, to be detected in the ECAL and no interaction (missing energy) thereafter. The threshold set for the experiment was $f=$ $0.5\mathrm{E}_0$ where E_0 is the incoming beam energy, taking into account the A' yield spectrum as a function of the missing energy as shown in Figure 2.3. Therefore, the signature for the signal is:

$$S_{A'} = S1 \times S2 \times S3 \times ECAL(E_{ECAL} < 0.5E_0) \times \overline{V2 \times HCAL} \tag{5.11}$$

The threshold for the zero energy event for the HCAL was chosen to be $<$ 1 GeV/c. Thus the signal box was $E_{ECAL} < 50$ GeV/c and $E_{HCAL} < 1$ GeV/c. The background sources for the above signature can be classified as physical or beam-related. The goal of the detector design was to reduce the background below the physical background level. Full detector simulation to investigate the backgrounds down to a level $\leqslant 10^{-10}$ was difficult due to the requirement of huge statistics that would lead to large amount of computer time. Consequently, the following backgrounds, identified as the most dangerous, were considered and evaluated with reasonable statistics and numerical calculations. All the identified background sources and their suppression were included in the proposal of NA64 [37].

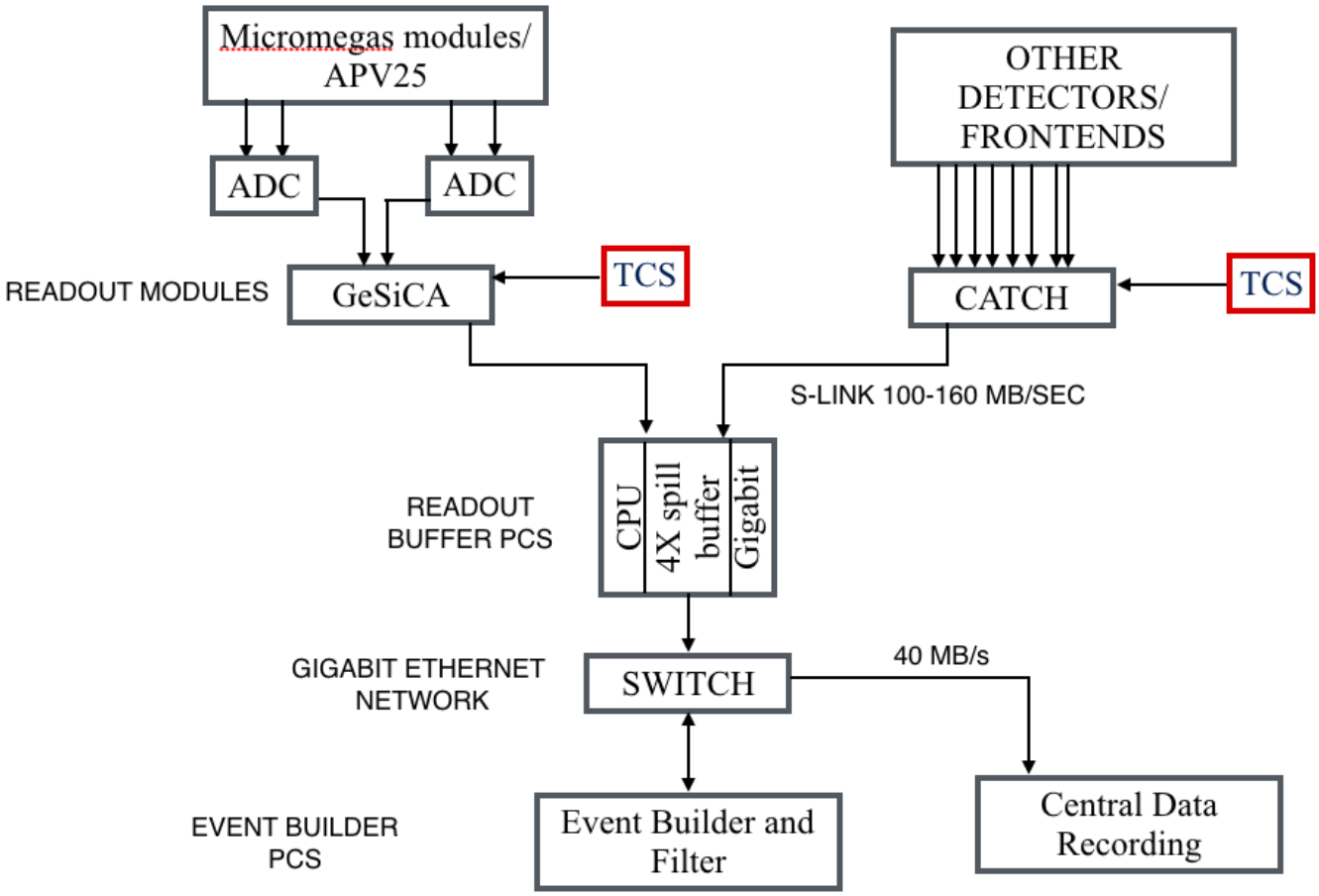

Figure 5.29: General schematic for the NA64 DAQ.

5.2.1 Physical Background

- Energy leak of the primary electron can occur due to the bremmstrahlung process

$$e^- Z \to e^- Z \gamma \tag{5.12}$$

when the maximum of the energy is carried by the emitted photon while the final state electron with energy, $E_e \sim 0.1E_0$, is absorbed in the ECAL. If the photon punches through the rest of the detector without interactions or is absorbed in a photo-nuclear reaction in the ECAL, resulting in an energetic leading secondary punch-through neutron, the event would mimic the signal of 5.11. Since the total thickness of the ECAL is $\sim 40X_0$, and the primary interaction vertex is within a few X_0s, the probability for a photon to punch through without interactions is extremely rare .

- Since the signature of the search is missing energy the hermeticity of the detector is crucial. Interaction of the incoming electron on the target emitting a hard photon, depositing the rest of its energy in the ECAL and the probability of the photon to induce a photo-nuclear reaction accompanied by the emission of a leading neutral particle that leaves the detector undetected can be a source of the background. An undetected electroproduced hard hadron (h) from the reaction $e^-A \to e^-hX$ can also cause a fake signature. Ensuring the hermeticity of the HCAL modules is necessary to suppress such background. The spectrum of energy in the first HCAL module obtained

during the beam time for a 100 GeV/c hadron beam as shown in Figure 5.30 shows the obtained energy resolution, $\sigma_E/E = 0.6/\sqrt{E(GeV)}$ +0.037 . The peak at the lower energy is due to punch-through of pions with the obtained punch-through probability $\sim 10^{-3}$ for the first module. The zero energy detection inefficiency due to e.g pile up effects is estimated to be below 10% for a 3.3×10^5 e^-/sec/cm^2 intensity for a zero energy HCAL threshold set at 1 GeV/c. For larger thickness of the HCAL (four modules in the case of NA64), the pion punch-through probability is, therefore, negligible. To estimate the HCAL non-hermeticity for high energy neutral hadrons with simulation 2×10^5 neutrons with energy 100 GeV/c was simulated with Geant4 to check their energy distributions in three consecutive HCAL modules of lateral size 20 cm $\times$ 20 cm. Figure 5.31 shows the distribution of energy for the neutrons (right). The 0 GeV peak for the HCAL1 module for neutrons corresponds to the punch-through cases wherein the particle penetrates the HCAL1 without interaction. The peak disappears for larger HCAL thickness as expected, however, there is still zero energy deposition events. Only events from the low energy tail of the deposited energy, shown in Figure 5.32 (left), was checked to save on computational time and to estimate the non-hermeticity of the HCAL for neutrons. Figure 5.32 (right) shows the tail of the obtained energy distribution in HCAL3 from about 5×10^6 neutrons, fitted with a polynomial function (shown in red) to obtain the extrapolated results for the low energy part of the spectrum. For the chosen threshold of the experiment of 1 GeV/c the number of events with energy $<$ E_{th}=1 GeV/c is $\sim 10^{-9}$ with respect to the total number of events. Multiplying by a factor of 10^{-4} for the probability of a single leading hadron production/electron in the ECAL, the overall resulting level of the background comes to $\leqslant 10^{-12}$.

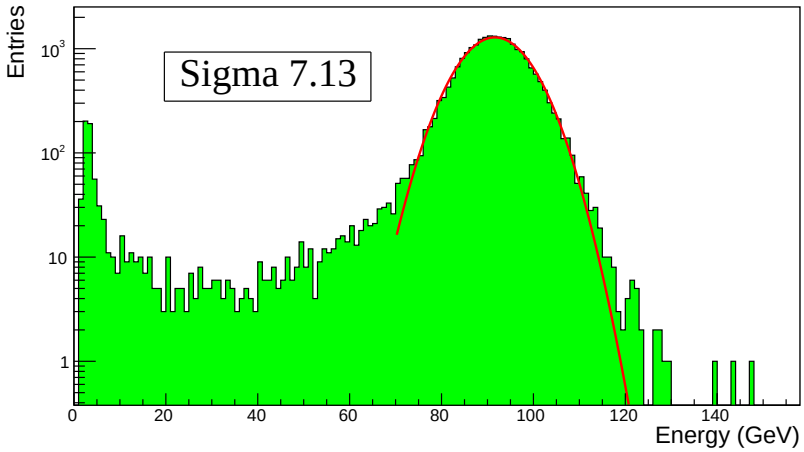

Figure 5.30: Energy deposited on the first module of the HCAL from a 100 GeV/c hadron beam from the 2016 beam time. The fitted gaussian gives the energy resolution $\sim$ 7 GeV/c for a 100 GeV/c beam.

5.2.2 Beam Background

- One of the most dangerous background for the search is the low energy tail of the primary electron beam which is a result of primary beam interaction with passive material in the beam line, e.g., entrance windows, residual gas etc and pion or muon decays in flight in the beam line. A high precision full beam line simulation would be necessary to predict the true level of these background events. However the level of this

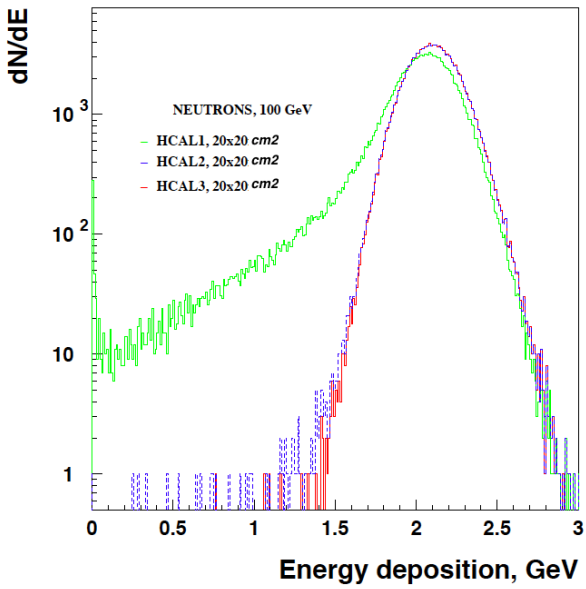

Figure 5.31: Energy distribution by 2 × 10^5 neutrons with energy 100 GeV/c in three consecutive HCAL modules of lateral size 20 × 20 cm^2 obtained from Geant4. The peak at 0 GeV corresponds to punch-through particles. [37]

background with number of events N(E<E_{th}) with energy less than the chosen threshold of 0.5E_0 for a 100 GeV/c beam is expected to be $< 10^{-2}$. The spectrometer with Micromegas trackers (MM1-4) placed in the NA64 beam line, equipped with reconstructing the incoming momenta of the beam particles deflected under the magnetic field, is used to further suppress this background to a negligible level. A detailed simulation of a 100 GeV/c beam with a low energy tail was performed and the momentum reconstruction was checked as a function of the deposited energy on the ECAL for $\sim 10^{10}$ simulated events as explained in Section 5.1.5. The background was successfully suppressed at a level $< 10^{-10}$ with tracking from simulation.

- Beam contamination and hadronic electroproduction in the ECAL can lead to hadronic backgrounds. Beam hadron contamination is suppressed by synchrotron radiation tagging of the incoming beam by the BGO and Pb-Sc detectors. The level of beam contamination as seen during the beam time is $\sim \pi/e < 10^{-2}$. This combined with the suppression factor with synchrotron radiation detection $\sim 10^{-3}$ and the probability of the pion to escape detection given the hermeticity of the HCAL results in this background level to be $< 10^{-12}$.

- Contamination of the primary beam with muons may also give rise to a fake signature when a beam muon produces a low energy photon in the ECAL as

$$\mu + Z \rightarrow \gamma + \mu + Z, \mu \rightarrow invisible \tag{5.13}$$

which is absorbed in the calorimeter while the muon escapes the rest of the detector undetected. Assuming the muon contamination in the beam to be $< 10^{-2}$, suppression due to the synchrotron radiation detection to be $\sim 10^{-3}$, probability of the muon crossing the veto V2 undetected to be at the level 10^{-4}, and the probability of the muon depositing energy in the HCAL below the threshold to be $< 10^{-4}$, the probability of the above event comes out to be $< 10^{-13}$

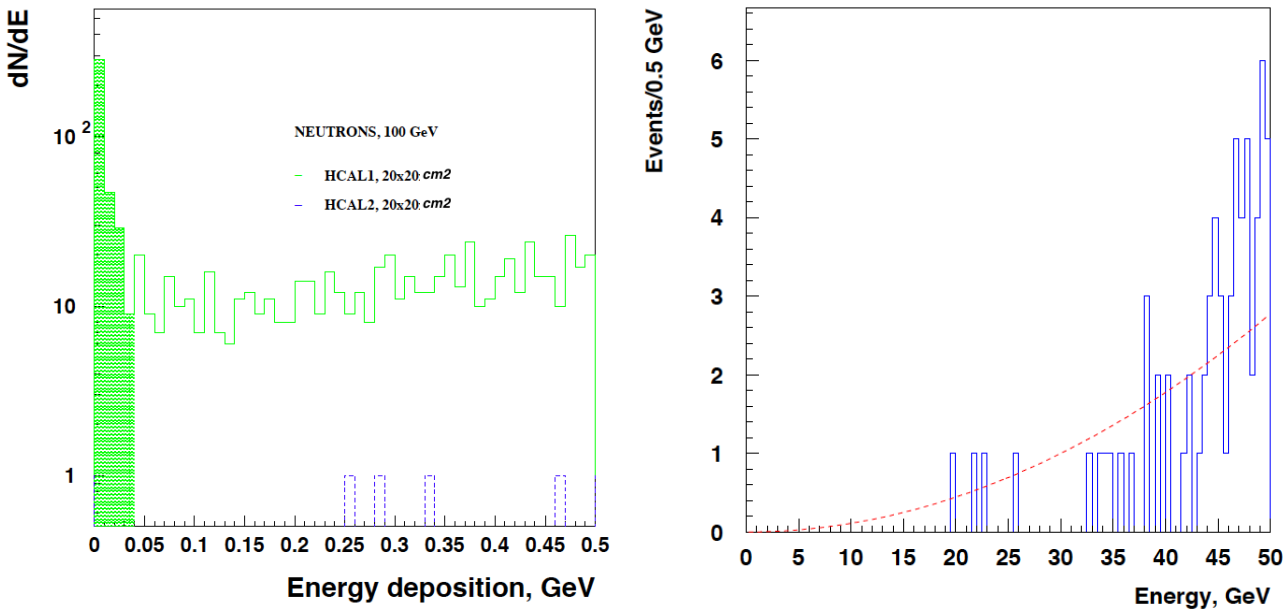

Figure 5.32: Low energy part of the energy deposition spectrum by 2×10^5 neutrons (left) with energy 100 GeV/c in three consecutive HCAL modules of lateral size 20×20 cm^2. The expected low energy tail distributions in HCAL3 from about 5×10^6 neutrons with primary energy of 100 GeV/c. The peak from the total energy deposition in normalized to 100 GeV/c. The dashed curve shows the polynomial fit to the distribution. [37]

- The ECAL signal duration ($\sim$ 100 ns) sets the limit on the accepted beam intensity, $\leqslant 1/\tau_{ECAL} \sim 10^6$ e$^-$/sec (to avoid significant loss of efficiency due to pile-up), which sets the statistical limit on the sensitivity of NA64. However, a e$^-$ pile-up removal algorithm can be implemented for high efficiency signal and energy reconstruction and the experiment can then be run at rates $\sim$ a few 10^6e$^-$/sec. Uncorrelated superposition of low energy, 50-70 GeV/c, electron with a 100 GeV/c pion (or muon) within the detector gate-time could result in a fake signature as the low energy electron could emit synchrotron radiation above the detection threshold and deflect under the magnetic field without reaching the ECAL, while the accompanying π (or μ) can decay in flight into eν (e$\nu\nu$) state with the decay electron energy $<$ the beam energy thus mimicking the signal signature. This background is beam related and as mentioned before the fraction of events with energy 50-70 GeV/c in a 100 GeV/c beam could be as large as 10^{-2}, the time resolution between e$^-$ and π (μ) events is of the order of ns and the fraction of π (or μ) contamination in the beam is $\leqslant 10^{-3}$ with the probability of decay to eν (e$\nu\nu$) $\sim 2 \times 10^{-7}$ (10^{-6}), resulting in the final level of the background to be $< 10^{-15}$ (10^{-14}) /electron for a beam intensity $\sim 10^6$ e$^-$/sec.

Thus the overall probability of a fake signature due to all the above mentioned background sources comes out to be $< 10^{-12}$. The two week beam run of NA64 in July' 2016 was dedicated for the search of $A' \rightarrow$ *invisible* decay channel. The analysis of the data for the beam run alongwith the simulation results to establish all detector response and optimization of selection cuts are presented in the following Chapter.

Chapter 6

Data Analysis and NA64 Results

The search for $A' \rightarrow invisible$ decay requires that the reaction 2.1 occurs within the first few radiation lengths, X_0, of the ECAL, depositing a fraction of the beam energy in the ECAL, while the remaining is carried by the A' which decays into weakly interacting dark matter particles (χs) that escapes the detector without any interaction in the Veto or HCAL. This results in the missing energy signature and the $A' \rightarrow invisible$ decay would appear as an excess of events above those expected from background sources with a single electromagnetic shower in the ECAL and zero energy deposition in the rest of the detector. To suppress any background and pile up events the signal signature requires

1. Time co-incidence of event between S1-S3 and the ECAL
2. Reconstructed momentum of the incoming particle with MM1-4 match the beam momentum
3. Synchrotron radiation detected in the SRD detectors matches that from an electron to suppress hadron and muon contamination
4. The lateral and longitudinal shower shape in the ECAL is consistent with that expected for a signal shower.
5. The missing energy is consistent with the threshold set for the experiment. The threshold selected for the fraction of energy, f, deposited in the ECAL was $f = 0.5E_0$ where E_0 is the beam energy = 100 GeV/c. Thus the selection criteria for the recoil electron is $E_e < 50$ GeV/c with the missing energy, $E_{miss} = E_{A'} = E_0\text{-}E_{ECAL} > 0.5E_0$. The threshold was optimized taking into account background extrapolation from data and the sensitivity of the experiment based on the A' emission spectra as a function of the missing energy.
6. No energy deposition in V2 and HCAL1-4. The threshold set for the zero energy events in the HCAL was < 1 GeV/c and Veto was < 10 MeV as explained in Section 5.1.

Before finalizing the cuts for the signal search, each detector performance and response was established either with Geant4 based Monte Carlo, test beam data or both. Background sources were also simulated to select cuts and estimate the reconstruction efficiency. 10 % of the data set was used for optimization of the cuts and the full sample was used to estimate the background. The following sections include detector performances, optimization of cuts, Monte Carlo simulations and results obtained from the July'2016 beam run. The work done on the spectrometer of the experiment including the synchrotron radiation detection and tracking of the incoming beam was the main contribution of this thesis.

6.1 Synchrotron Radiation Tagging

Electron identification is crucial for NA64 due to its missing energy signature, as beam contamination with hadrons or μ can lead to background sources mimicking the signal. The expected hadron contamination in the 100 GeV/c e^- beam at the H4 beamline at CERN is $\pi/e < 10^{-2}$. In order to identify the incoming electron and subsequently suppress the beam contamination synchrotron radiation tagging with BGO/Pb-Sc calorimeters is used with the incoming particle being deflected under the integral field $\sim$ 7 T.m over the two 2 m dipole magnets.

The synchrotron radiation detector was tested during the July' 2016 beam time and its performance cross-checked with Geant4 Monte Carlo simulation. During the beam time of NA64 the deflection of the 100 GeV/c beam at the point of the BGOs was $\sim$ 31 cm due to the magnetic field used. The two rows of BGO detectors were placed away from the deflected beam direction as shown in Figure 6.1. The distance of the BGOs from the deflected and undeflected beam axis was $\sim$ 9 cm each to minimize bremmstrahlung photons, neutrals produced upstream due to primary beam interaction with the dead material (vacuum windows, counters etc), and beam halo particles from hitting the BGOs and saturating the signal thus compromising the signal efficiency due to longer decay time of the BGOs as was observed during the first test beam time of 2015 expalined in Section 5.1.4. The crystals 3

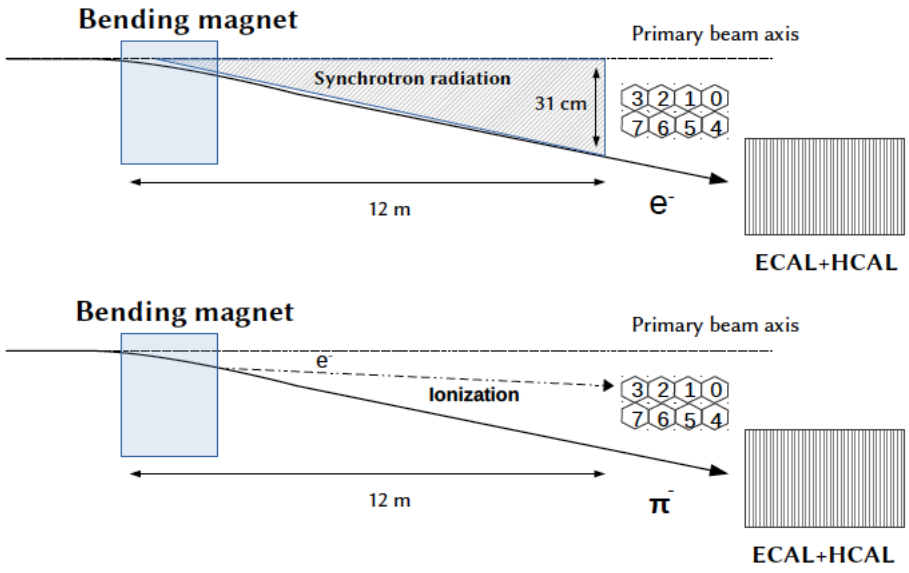

Figure 6.1: Arrangement of the BGO crystals during the July' 2016 beam time. Crystals 3 and 7 collect most of the synchrotron radiation. Crystals 0 and 4 used as a veto. Top: Event leaving a SR signal in the SRD. Bottom: SR- like signal in the SRD for a knock-on electron produced by pions. [101]

and 7 facing the beam, detect the majority of the synchrotron radiation, while the crystals 0 and 4 on the far end of the arrangement are only fired in case of a high energy deposition and thus can be used to veto such events. The remaining six crystals act as a shield from back scattered particles from the ECAL suppressing hadrons by an additional order of magnitude. Using the co-incidence of two BGO crystals it is possible to improve the electron tagging by rejecting knock-on electrons produced by incoming pions. Since the synchrotron spectrum is

homogenous, the radiation is expected along the entire arc described by the deflected beam radius, as opposed to electrons from hadron ionisation that will leave a signal on a single crystal.

In order to establish the performance of the detector and optimize the cuts, data from a 100 GeV/c π beam of intensity $\sim 3 \times 10^3$ π/sec/cm^2 was analysed for direct measurements of the suppression factor. Time co-incidence of the scitillators S1-S3 and an additional requirement of < 60 GeV/c energy deposition in the ECAL was set to ensure a pure π sample of $\sim 10^5$ collected events. A 100 GeV/c electron beam with a beam intensity $\sim 2 \times 10^4$ e$^-$/sec/cm^2 was also analyzed to establish the signal efficiency. Same time coincidence between S1-S3 as was used for the pion run was set with the additional requirement of the total energy deposition in the ECAL+HCAL to be > 90 GeV/c and sum of energy deposition in the HCAL modules to be < 20 GeV/c, to reduce pion contamination in the sample which was observed to be a few % in the beam as expected. Figure 6.2 shows the comparison of data and Monte Carlo (MC) of the synchrotron radiation spectrum for electron and pion beams. The comparison of the SR spectrum of electrons between the beam and simulation is used to calibrate the BGOs. As seen a very good agreement was achieved with this method. To check the suppression factor for pions and efficiency for electrons, 1% beam pile-up events

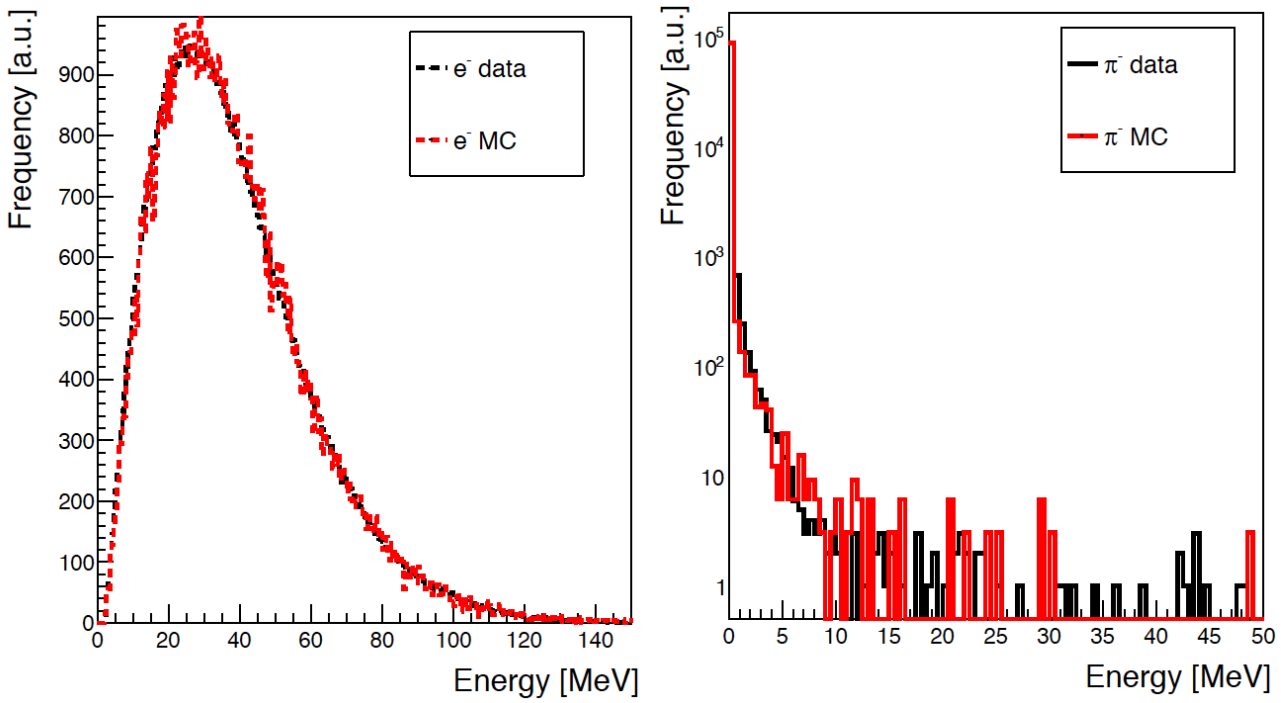

Figure 6.2: Comparison of the synchrotron radiation spectrum data and simulation (MC) for 100 GeV/c electrons (left) and pions (right).

was added to the simulated electron spectrum, as was predicted for the given beam intensity. The suppression and efficiency was checked as a function of: 1) The threshold set on the total energy deposited in the SRD, and 2) The threshold set on the time co-incident signals on both crystals 3 and 7 (multiplicity requirement). Figure 6.3 shows the efficiency for the electrons and the suppression factor for the pions as a function of a cut on the threshold energy deposited in the SRD. As seen, with the multiplicity requirement the drop in signal efficiency is quite small compared to without it while the suppression factor for pions improves substantially as would be expected due to the feature of the synchrotron radiation

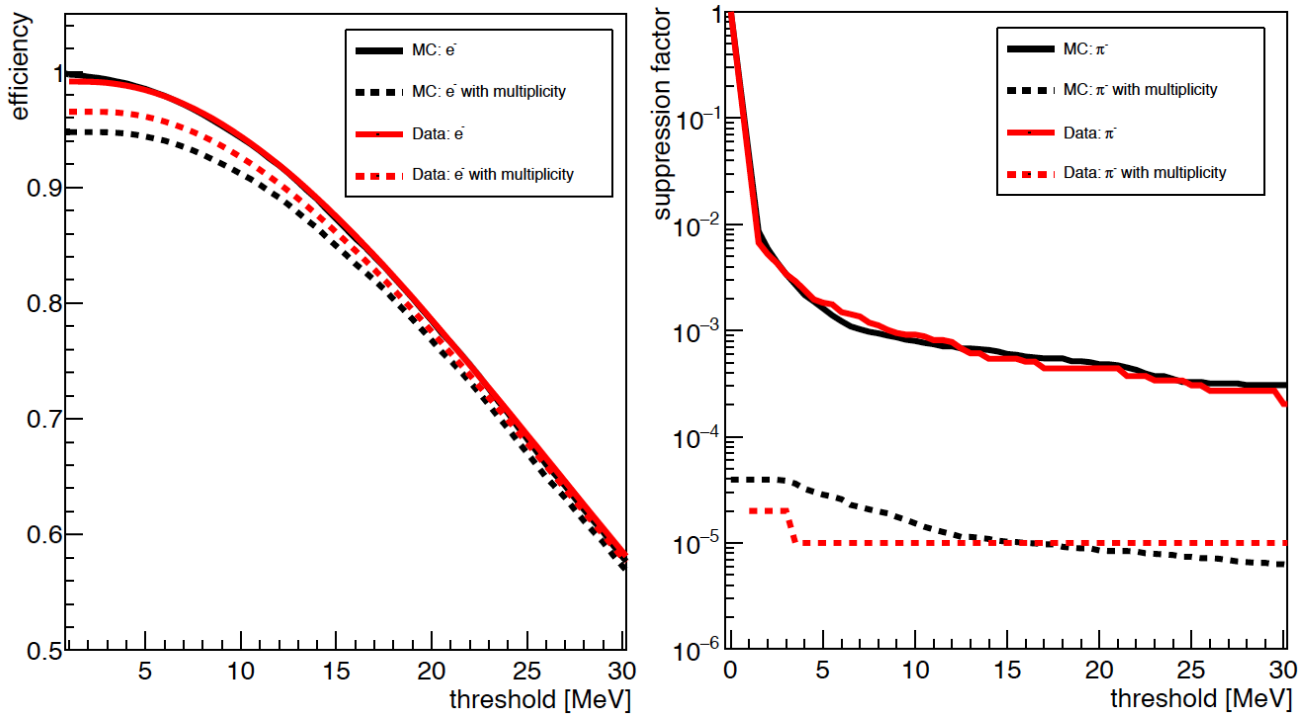

Figure 6.3: Left: Comparison between data and simulation of signal efficiency as a function of a cut on the threshold energy set on the total energy deposited in the crystals (3 and 7) and for multiplicity requirement. Right: Comparison between data and simulation of suppression factor as a function of a cut on the threshold energy set on the total energy deposited in the crystals (3 and 7) and for multiplicity requirement

spatial distribution unlike the electrons from hadron ionization. Thus with a cut on the total deposited energy of 10 MeV a suppression factor $< 10^{-3}$ is achieved with ~ 97 % signal efficiency. Exploiting the granularity of the detector, one can further suppress secondary electron events due to hadron ionization, achieving a pion suppression factor $< 10^{-5}$ with a signal efficiency ~ 95 %. In order to further improve the detector efficiency not being limited by pile-up effects due to the long decay time of BGOs, faster detectors as the Pb-Sc calorimeters, described before were also used during the July'2016 beam run with similar suppression factor of $< 10^{-3}$ as the BGOs.

6.2 Tracking with Micromegas modules

The Micromegas trackers required to precisely track the incoming beam deflected in the magnetic field to reconstruct their momentum and suppress background from the low energy tail of the beam were tested during the beam time of NA64 in July and October' 2016. The clustering and the cleaning algorithm for the multiplexed detectors were included in the data analysis and tested for the first time in a high intensity beam. The momentum reconstruction was performed with the Genfit software, a generic track reconstruction framework for nuclear and particle physics [102]. The efficiency and resolution of momentum reconstruction (Section 6.2.2) were checked for different beam intensities and it is shown that the detectors work well in high flux environment. The performance results are presented below.

6.2.1 Multiplexing ambiguity and correction

The Micromegas detectors were read by the 128 channel APV chips and the strips were multiplexed following the genetic multiplexing algorithm proposed in [86] and explained in Chapter 4. In this mapping construction there is only one set of two consecutive strips corresponding to a given set of two electronic channels. Therefore, as explained in Chapter 4 with 128 channels the maximum number of unordered doublets is $\sim$ 8066. Therefore, in principle 8066 strips could be read with 128 channels following the multiplexing scheme. For NA64 the number of strips/module was 640 with 320 strips each for the X and Y layer. Therefore the multiplexing map was constructed in such a way so as to read 320 strips by 64 channels, thus having a multiplexing factor of 5 to limit ambiguities at high intensities, following the above scheme. The multiplexing formula used to obtain the channel-strip ($c(s)$) mapping per plane where $c(s)$ is the channel corresponding to strip s is:

$$c(s) = \mathrm{mod}(s \times (\mathrm{floor}(s/p) \times m + 1), p) \tag{6.1}$$

where p is the number of electronic channels = 64, m=6 and mod and floor are the modulo and the rounding down functions. The above equation is, however, only valid when p and $m + 1$ does not share a common prime factor. m gives the maximum cluster size which does not lead to repetition of at least two consecutive strip connections. These repetitions result in "ghost" clusters which lead to ambiguities in the hit recognition. This ambiguity was controlled with additional knowledge of signal spread and integrated charge. These two parameters were found to be co-related as would be expected.

As mentioned above a signal is defined when two or more consecutive strips register a hit on receiving a trigger. Due to the multiplexing of the modules some ambiguities in the signal reconstruction are expected due to the loss of information. For example if two particles enter the detector at the same time different combinations of channels may arise giving "ghost" signal clusters or if a signal cluster has a large spread ($>$ 6 strips in this case) smaller "ghost" clusters with two or more strips may also arise due to the multiplexing feature. For example in our design, the $channel_{strip}$ combination for channels 0-7 are given by:

$$\begin{array}{ccccc}
0_0 & 0_{64} & 0_{128} & 0_{192} & 0_{256} \\
1_1 & 1_{119} & 1_{133} & 1_{219} & 1_{297} \\
2_2 & 2_{110} & 2_{138} & 2_{246} & 2_{274} \\
3_3 & 3_{101} & 3_{143} & 3_{209} & 3_{315} \\
4_4 & 4_{92} & 4_{148} & 4_{236} & 4_{292} \\
5_5 & 5_{83} & 5_{153} & 5_{199} & 5_{269} \\
6_6 & 6_{74} & 6_{158} & 6_{226} & 6_{310} \\
7_7 & 7_{65} & 7_{163} & 7_{253} & 7_{287}
\end{array}$$

So for a 7-strip wide signal cluster (not unlikely as seen from Figure:6.13 in the following Section) between strips 0-7, the connection of channels 0 and 7 to consecutive strips 64 and 65 will also give rise to this fake combination of "ghost" cluster.

One option to limit the ambiguities, therefore, is to reduce the multiplexing factor to suppress the probability of fake combinations. It should also be possible to optimize the mapping and the minium cluster size parameter, m, to reduce the level of ambiguities. A complementary solution is to use additional available information such as the signal spread as suggested in [86]. As part of the work of this thesis it is shown that one can substantially

suppress the "ghost" clusters by using the information from the integrated charge of the cluster and its size.

We compared all signal clusters on each plane that share the same readout channel and suppressed the clusters with smaller number of strips and integrated charge from that group on account that they are more likely results of fake combinations due to the multiplexing instead of real particle hits. Actual particle hits are expected to produce clusters with the largest integrated charge and size in terms of number of strips.

In order to estimate the level of ambiguity due to the spread of the signal cluster alone, we compared one particle hit events before and after the cleaning and plotted the Ambiguity probability (%) as a function of the flux. The level of ambiguity due to the signal spread is not a function of the beam flux and depends predominantly on the size of the signal cluster. Figure 6.4 (left) shows the % of events wrongly identified as having > 1 cluster for 1 particle hit events before the cleaning as a function of the beam flux. As expected there is no co-relation between this probability and the beam flux. However the ambiguity due to pile up

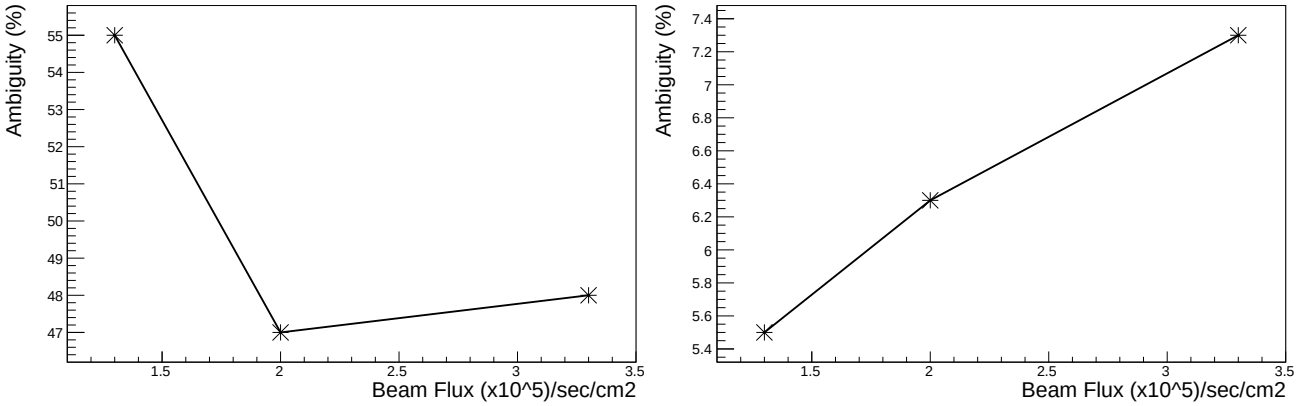

Figure 6.4: Probability of Ambiguity (%) due to cluster signal spread (left) estimated from 1 particle hit events and the Probability of Ambiguity (%) due to 2 particle pile up (right) estimated from 2 particle hit events before and after the cleaning for a multiplexing factor of 5

of particles depends on the beam flux. To estimate the probability of ambiguity due to particle pile up, we compared 2 particle hit events before and after the cleaning and plotted the Ambiguity probability (%) as a function of the flux. Figure 6.4 (right) shows the probability of ambiguity as a function of the flux. Almost 80 % of the 2 particle hit events gave > 2 signal clusters before the cleaning but since only 7-9 % of the total events (in a given run) actually had 2 particle hits (depending on the flux) the probability of ambiguity for a given run due to the pile up came out to be in the range 5-7 % for ~ 100 kHz/cm^2 beam flux.

To estimate the level at which a "ghost" cluster was selected instead of the true signal cluster, with the method described above, we compared the position of the signal clusters on MM 3 and MM 4 for a deflected beam under the magnetic field ~ 7 T.m. A parallel incoming track was selected within the beam spot using the position information from MM 1 and 2 such that its energy in the ECAL was in the range 100 GeV $\pm$ σ_{ECAL} where $\sigma_{ECAL} \sim 2$ GeV is the energy resolution of the ECAL. Figure 6.5 shows the distribution of the difference of cluster position on each projection between MM 3 and 4 for the same track candidate in an

event. The distribution has a flat background with less than 2 % of the events with a difference larger than $4\sigma_{MM}$, where σ_{MM} is the standard deviation of the distribution ~ 400 μm for the deflected beam. The resolution is limited mainly by the energy spread of the selected track. Systematic uncertainties due to orientation of the MM modules (along the rotational axes) are not taken into account for this estimation. The estimation gives an upper limit to the level of wrong cluster identification after the cleaning method due to the multiplexing ambiguities. Thus we present an efficient way to limit the level of ambiguity substantially from ~ 50 % to < 2 % chance of wrong cluster identification using the cluster size, integrated charge and channel information. With higher flux and pile up one can reduce the factor of multiplexing to limit the level of ambiguity further, depending on the acceptable level of ambiguities for the respective applications.

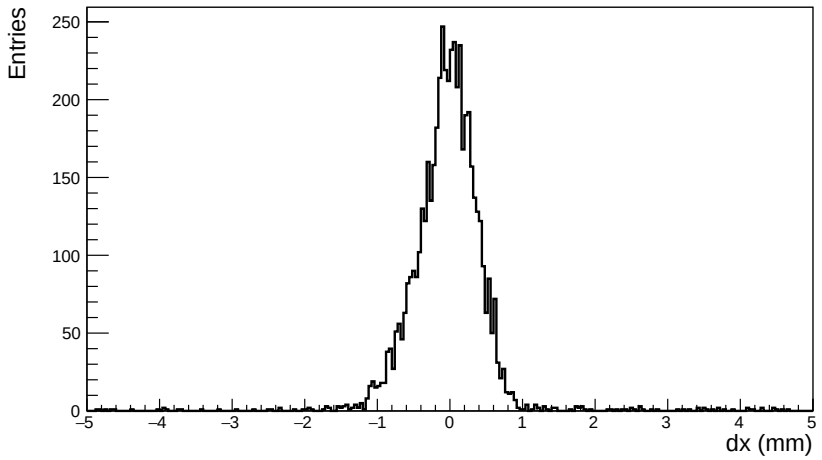

Figure 6.5: Distribution of difference of cluster positions in each projection between MM 3 and 4 after selecting parallel tracks within the beam spot with MM 1 and 2 with energy 100 GeV/c $\pm$ σ_{ECAL} selected with the ECAL

In the following sections we present the Micromegas tracking results obtained during the July and October' 2016 beam time of the NA64 experiment. During the beam run it was possible to check the performance of these multiplexed modules for different beam intensities and establish its efficiency in such high flux environment.

6.2.2 MM Efficiency

The efficiency of the detectors is directly proportional to the gain of the detector but the gain also should not be so high that the detectors start discharging. It was checked that the detectors start to discharge for amplification voltages > 560 V in the beam. To optimize the performance of the detectors the efficiency was checked as a function of the amplification voltage (gain) in the beam. The Micromegas detectors were placed in the maximal beam intensity of 3.3 $\times 10^5$ e^-/sec/cm^2 and their efficiency was checked for different amplification voltages and a fixed drift voltage of -300 V. Figure:6.6 shows the efficiency of MM modules as a function of the amplification voltage for the four modules. The efficiency for all four modules increases with increasing voltage, as expected with the increase of the gain which saturates at around 545 V. The Micromegas efficiency was also checked for different beam fluxes after fixing the amplification voltage at ~ 555 V for MM 2, 3 and 4 and ~ 545 V for

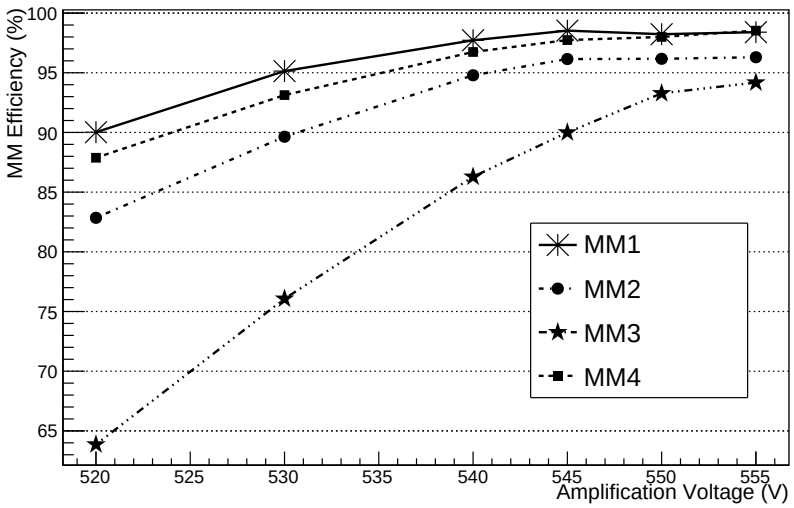

Figure 6.6: Efficiency of the four MM modules as a function of the amplification voltage

MM 1, those being the voltage with the highest efficiency for the respective modules. Figure:6.7 shows the efficiency of MM modules as a function of the beam flux. As seen from the plot for a rate of 3.3 $\times 10^5$ e^-/sec/cm^2 which was the maximum flux achieved during the beam time, the average hit efficiency of the four MM modules is $\sim$ 96 % with MM3 being the least efficient. It was found to be the most noisy detector from the pedestal distribution of its electronic channels. Figure 6.8 (left) shows the distribution of the cluster size on one plane

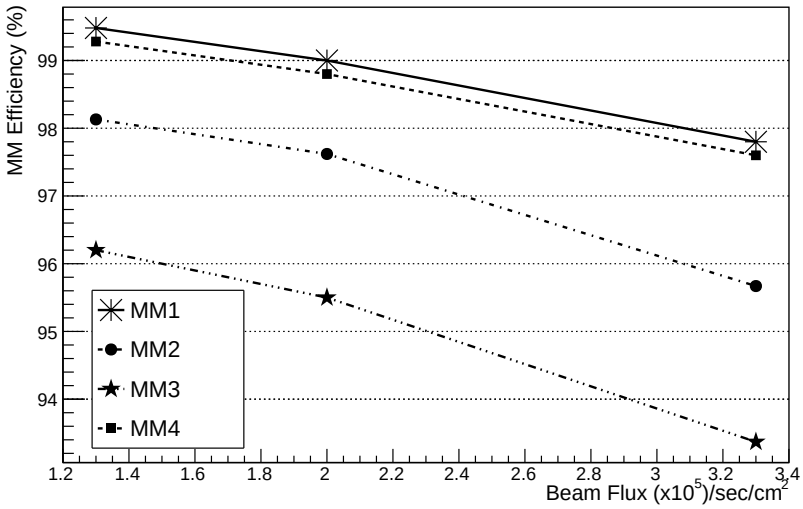

Figure 6.7: Efficiency of hit of the four MM module as a function of the beam flux

(X) and (right) the number of clusters per event as a function of the beam flux. As seen, the cluster size distribution barely changes indicating that the multiplexing is not responsible for the efficiency drop observed at higher fluxes. This effect is related to the increase of pileup events and detector discharges as was observed during the particle spill with increasing flux.

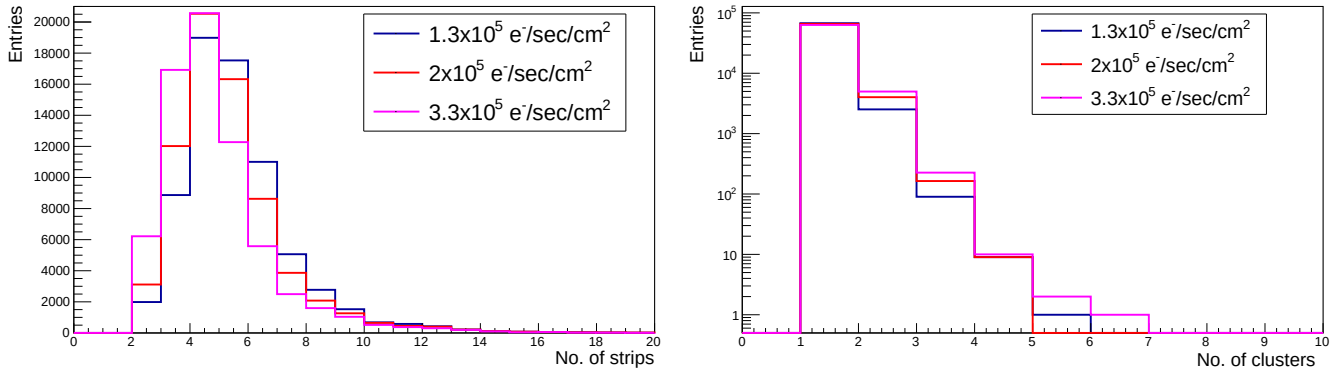

Figure 6.8: Size of clusters (left) and No. of clusters per event (right) as a function of the beam flux

6.2.3 Hit Resolution and Tracking

The performance and accuracy of tracking with these modules were also checked in the beam at the maximal beam intensity. Figure:6.9 shows the beam spot on the MM modules. The observed beam diameter matched the expected value of $\sim$ 2 cm given by Ilias Efthymiopoulos at the CERN SPS. The distribution of the difference between the hit positions of an undeflected beam (without the magnetic field) on the MM modules is shown in Figure:6.10. The sigma of the distribution is a convolution of the spatial resolution of the two chambers. If we assume the spatial resolution for the two chambers to be equal the resulting spatial resolution of each chamber comes out to be $\sim \sigma/\sqrt{2} \sim 100$ μm. No cuts were made on this distribution and a parallel beam was assumed. Uncertainties due to the beam divergence and relative misalignment between detector modules and rotation of the modules with respect to the beam axis was not taken into account for this estimation. In order to establish that the multiplexing does not limit the resolution of the modules, the resolution of non-multiplexed Micromegas modules of same strip pitch was also checked similar to the multiplexed modules. Figure 6.11 shows the distribution of the difference between the signal cluster positions between two non-multiplexed modules. The resolution obtained $\sim$100 μm is comparable to that of the multiplexed detectors. This shows the modules not only are efficient but also has good hit resolution under such high intensities with the multiplexed strips using the clustering algorithm written for such multiplexed detectors. Figure:6.12 shows the distribution of time of each plane with respect to the time of scintillator S1. The timing resolution obtained from the time calculation explained in Section 5.1.5 is $\sim$ 15 ns. The MAMMA collaboration tested Micromegas modules for the ATLAS New Small Wheel with APV chips sampling the entire signal shape instead of just three time samples and reported a timing resolution $<$ 10 ns in their test beam [125]. So it is possible to improve our obtained timing resolution, sampling the entire signal shape instead of just three samples which was not tuned for the chip during the beam time. The size of clusters/ plane is shown in Figure:6.13 in units of number of strips. The difference in the cluster size in the X and Y plane is expected due to the fact that the charge spreading along the R-strips crosses several Y strips. All plots presented show that the detectors are quite efficient $\sim$ 96 % at high rates without considerable ambiguity due to the multiplexing even in a high flux beam.

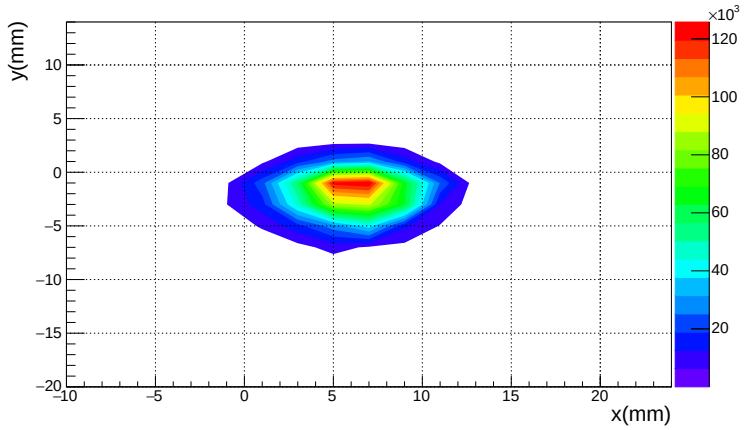

Figure 6.9: Typical Beam spot on the four Micromegas modules.

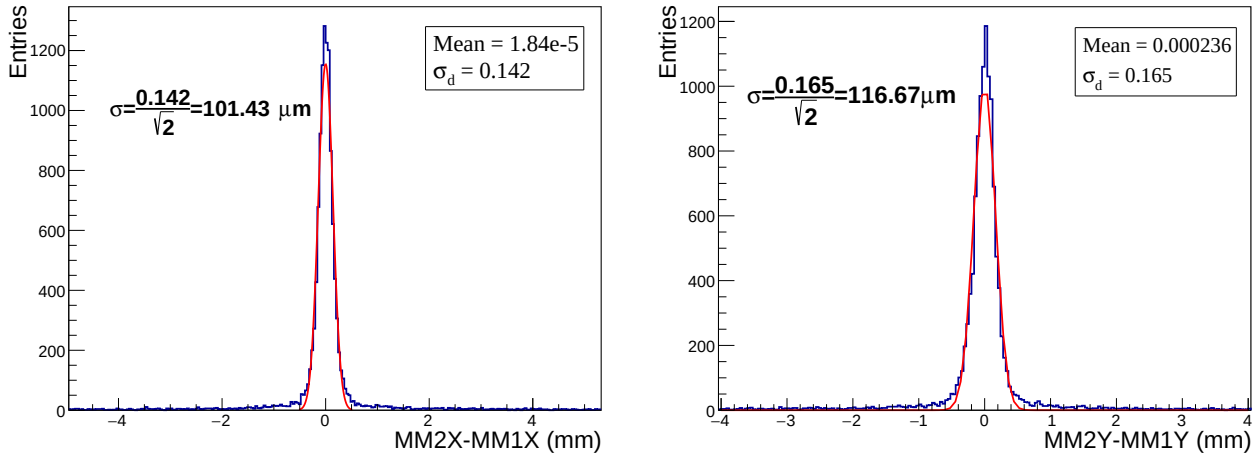

Figure 6.10: Distribution of difference of the hit positions on two MM modules. Position resolution for each module ∼ 100 μm assuming same spatial resolution of each module

6.2.4 Tracking in NA64 and suppression of low energy electron tail

The multiplexed modules were built for tracking in the NA64 experiment to suppress the low energy electron tail as mentioned above. Tracking of the incoming particles with the four modules was done under an integrated magnetic field of 7 T.m over two 2 m magnets. Fig.6.14 shows the reconstructed momentum for a 100 GeV/c electron beam as obtained with the Genfit software. The resolution of the central peak is ∼ 1.1 % as shown in the plot with an efficiency of 85%. The resolution obtained agrees well with the simulation results presented before of 1 % resolution for a 100 GeV/c beam. To improve the tracking efficiency, the number of MM stations that will be used in the next NA64 beam time will be doubled, i.e. 4 Micromegas will be placed before and 4 after the bending magnets. This upgrade will result in an increased overall efficiency of 92%. The preparation of a collinear beam is a key point in NA64. The modules were used to precisely measure the incoming angle of the particles in order to tune and optimize the beam collinearity. The angle was determined with an accuracy better than 1 mrad allowing to reject large angle tracks and keeping the beam divergence within 1 mrad as shown in Fig. 6.15. This accuracy allows to use the Micromegas also for the

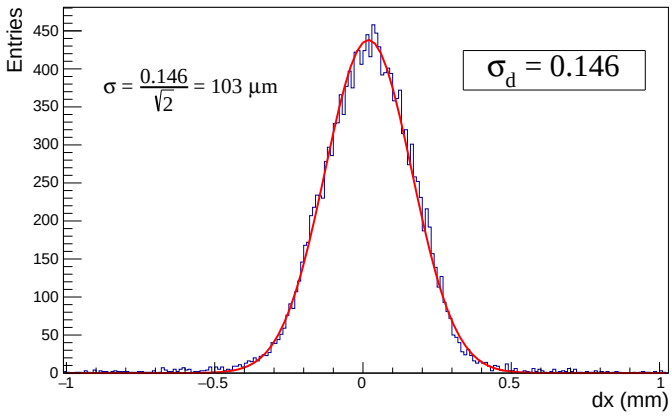

Figure 6.11: Distribution of difference of cluster positions for one projection between two non-multiplexed MM modules. The blue histogram is the data and the red line is a fitted Gaussian function with parameters "σ_d". Position resolution $\sim$ 100 μm obtained assuming same spatial resolution of each module

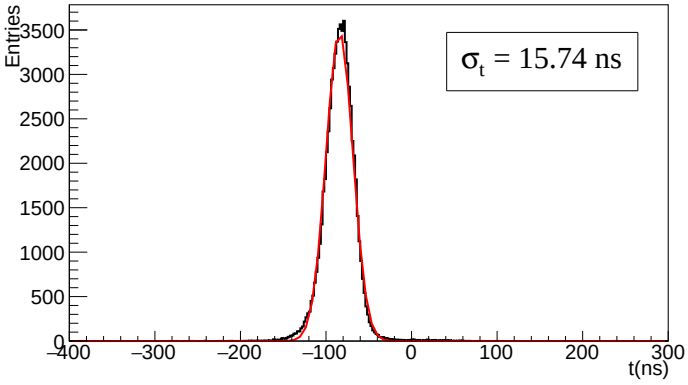

Figure 6.12: Timing distribution of the Micromegas modules with respect to scintillator S1 time.

transverse scan of the ECAL hermeticity in order to look for non-uniformity. In principle higher and lower momentum particles should not be within the acceptance of the geometry unless they enter with large incident angles with respect to the primary beam direction. The reconstructed momentum was also checked as a function of the incoming beam angle. Fig.6.16 shows a sketch of the incoming beam. The angle of the incoming beam with respect to the z-axis was calculated from the MM1 and 2 hit positions and the reconstructed momentum was plotted as a function of the angle as shown in Fig.6.17. As expected when the initial deflection is in the negative x direction the reconstructed momentum is larger with increasing angle and when the initial deflection is in the positive x direction the reconstructed momentum tends to be smaller with increasing angle. Therefore, the incoming angle measured by the 2 MMs (MM1, MM2 in Fig.5.2) upstream the magnet is a powerful tool to reject low energy electrons that are a dangerous background for the experiment [26]. In order to perform precise data analysis and obtain results from the NA64 beam time it is crucial to establish the ECAL response to signal and background events and establish its background suppression and signal selection efficiency from the energy measurements. The results from simulation and data analysis with the ECAL are presented below which was an important part that helped in publishing the results from the July 2016 beam time.

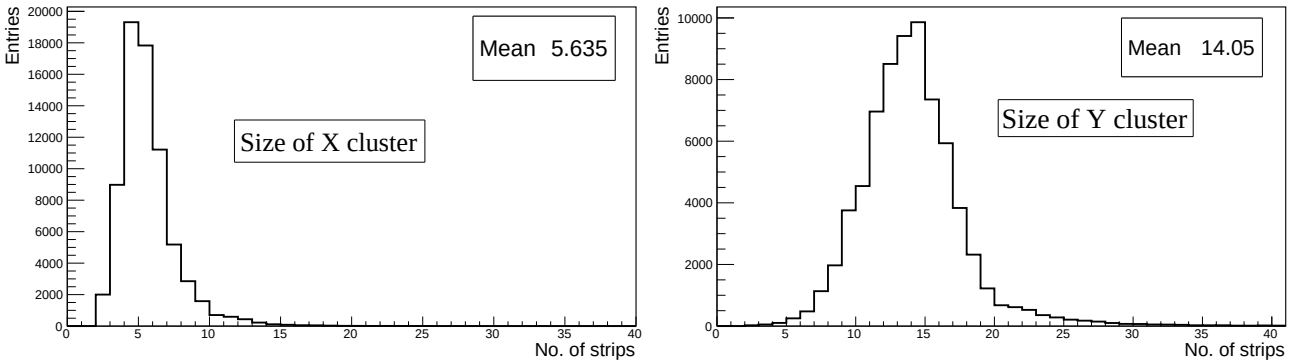

Figure 6.13: Size of clusters/plane in the Micromegas modules

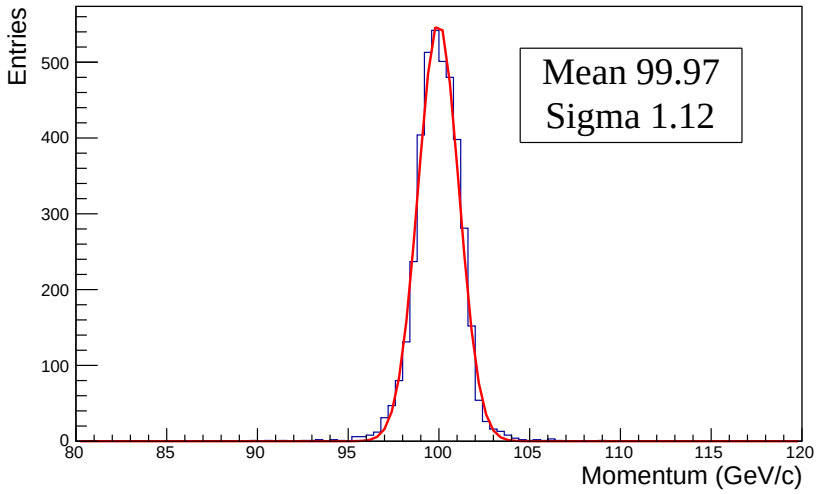

Figure 6.14: Reconstructed momentum with the four Micromegas modules for a 100 GeV/c beam. The black histogram is data and the red line is a fitted Gaussian function with parameters "Sigma" and "Mean"

6.3 ECAL Shower Development

One of the requirements for the signal selection is the consistency of the lateral and longitudinal shower development with that expected for a signal shower. The ECAL modules, having lateral and longitudinal granularity, serves not only as an active target but also help suppress hadronic background from the shower shape obtained from it. The suppression of hadrons was established with Geant4 simulations, studying electromagnetic and hadronic shower shapes and the suppression factor was found to improve by a factor 5-10. As is mentioned before the longitudinal segmentation of the ECAL is classified into two parts, preshower having $4X_0$ and absorption having $36X_0$. The preshower plays an important role in suppressing the hadronic background with the ECAL shower shape. Charge exchange processes like $\pi^{\pm} + N \rightarrow n\pi^0 + N'$ where one or more neutral pions in the final state receive most of the energy of the charged pion are ultimately the main limitations for hadron rejection. A cascade shower induced by the π^0 decaying into photons near the front of the ECAL array is indistinguishable from an electron-initiated shower and this accompanied by poor detection of the rest of the final state cannot be separated from a signal signature.

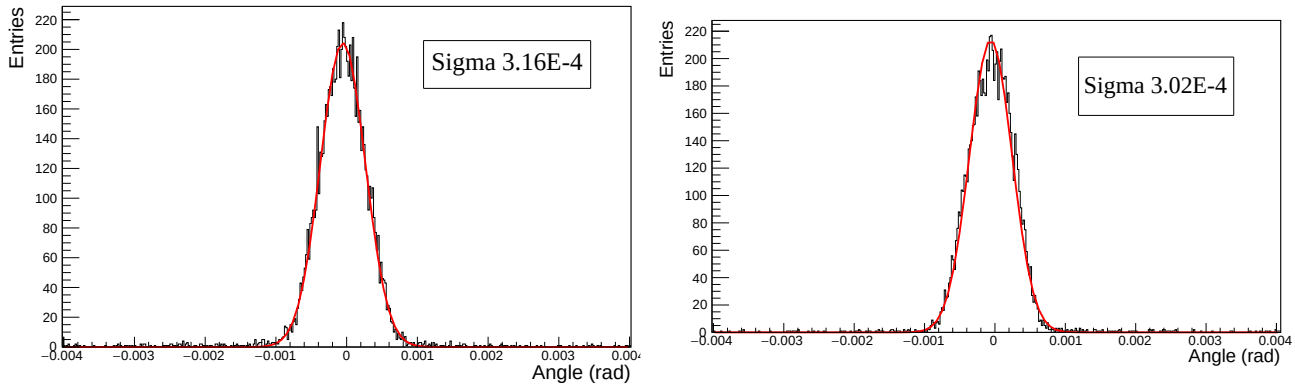

Figure 6.15: Left: incoming azimuthal angle of particle before the spectrometer measured with MM1 and MM2 with respect to the average beam axis.. Right: outgoing azimuthal angle of particle measured after the magnets with MM3 and MM4 with respect to the average deflected beam axis.

However such processes can be further suppressed by using the lead as the calorimeter passive material (it has a smaller number of interaction lengths per radiation length) and the requirement of an early development of the shower. Since the electron-hadron separation is enhanced by using the electromagnetic shower development in the early stage at the preshower section of the ECAL and the A' events are expected to be reconstructed as electromagnetic showers in the ECAL as well, it is important to establish a comparison in the properties of the shower due to the A' event and an ordinary electron shower with the same energy deposition in the ECAL. To answer this question a Geant4 simulation was performed to compare the lateral and longitudinal electromagnetic shower profiles in the ECAL due to an ordinary and a signal shower. The ECAL geometry used for the simulation was same as the real ECAL used during the beam time with a matrix of 6 $\times$ 6 cells, each with dimensions 38.2 $\times$ 38.2 $\times$ 490 mm^3. Each cell had 150 layers of 1.5 mm Pb + 1.5 mm Sc plates, totaling to $40X_0$. The cells were segmented longitudinally into the preshower part with $4X_0$ and the main ECAL with $36X_0$. The simulated energy resolution was as explained before, $\Delta E/E \sim 15\%/\sqrt{E}$ +0.7. In order to qualitatively compare the shower shapes the variable r = E_{PS}/E_{ECAL} of the ratio of E_{PS}, energy deposited in the preshower section and E_{ECAL}, total energy deposited, is compared for showers induced by electrons, pions and signal events. Figure 6.18 shows the preshower energy spectrum (left) and the signal efficiency as a function of the threshold set on the preshower energy, E_{PS}, for 100 GeV/c showers, induced by pions, electrons and signal events. Figure 6.19 shows the ratio r (left) and the signal efficiency as a function of the threshold cut on the r values for 100 GeV/c showers, induced by pions, electrons and signal events. The signal events were calculated using $E_{miss} > 0.5E_0$. As seen the fluctuations of the r value for the signal events are significantly larger than for the electron case. The r values range between 0 and 0.6 for signal events while for electrons the range is limited between 0-0.1. The spectra also show weak dependence on the A' mass. The interesting feature of the distribution is that the for the same preshower energy threshold E^{th}_{PS} the electron efficiency $\epsilon_e(E^{th}_{PS})$ is greater than the signal efficiency $\epsilon_{A'}(E^{th}_{PS})$ as shown in Figure 6.18 (right). The threshold for the preshower energy should be set $<$ 1 GeV/c to keep $\epsilon_{A'}(E^{th}_{PS}) > 0.9$. However the situation is inverse for the rth values, where for the same r value threshold $\epsilon_{A'}(E^{th}_{PS}) > \epsilon_e(E^{th}_{PS})$ as shown in Figure 6.19 (right). The reason for this is because the A' emission with energy $E_{A'} > 0.5E_0$ typically occurs in the early stages of the electromagnetic shower following which the remaining shower has much lower energy than the

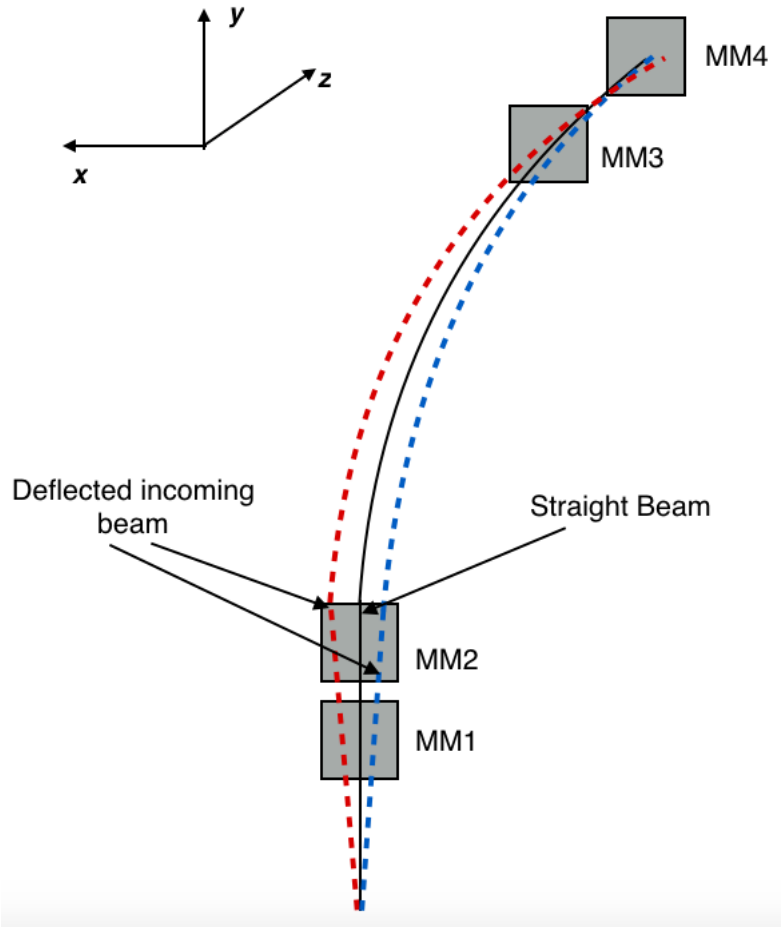

Figure 6.16: Example of incoming beam deflection. Incoming angle is calculated with respect to the Z-axis

primary electron energy and thus is shorter in length. Therefore, the majority of its energy is deposited in the preshower part of the ECAL. To compare the lateral shower development the variable E_i/E_{i+1} of the ratio of energies deposited on two adjacent cells along the X-coordinate (which is the co-ordinate of deflection of the beam under the field) as a function of the hit position X_e on the ECAL is compared for electron and signal showers as shown in Figure 6.20. The position $X_e = 19.1$ mm corresponds to the centre of the (i+1)-th cell, while $X_e = 0$ mm is the boundary between the cells. The dependence between the ratio E_i/E_{i+1} on the hit position X_e help define the shower profile, $E(X_e)$, as the energy release as a function of the distance from the shower axis. The shower profile function is well defined by the superposition of two exponential functions as

$$E(X_e) = a_1 exp(-|X_e|/b_1) + a_2 exp(-|X_e|/b_2) \tag{6.2}$$

The fit shown in Figure 6.20 results in the fit parameters of $b_1 = 2.1 \pm 0.3$ mm, $b_2 = 12.3 \pm 1.3$ mm and $a_1/a_2 = 0.14 \pm 0.03$ for electrons and $b_1 = 2.1 \pm 0.3$ mm, $b_2 = 12.3 \pm 1.3$ mm ($b_1 = 2.15 \pm 0.3$ mm, $b_2 = 11.9 \pm 1.4$ mm) and $a_1/a_2 = 0.14 \pm 0.03$ ($a_1/a_2 = 0.13 \pm 0.04$) for signal events with $M_{A'} = 50$ (500) MeV which match each other for both mass values. Determining the center of gravity, X_0, of the electromagnetic shower [108] using the equation

$$X_0 = 2\Delta\Sigma_i i E_i/\Sigma_i E_i \tag{6.3}$$

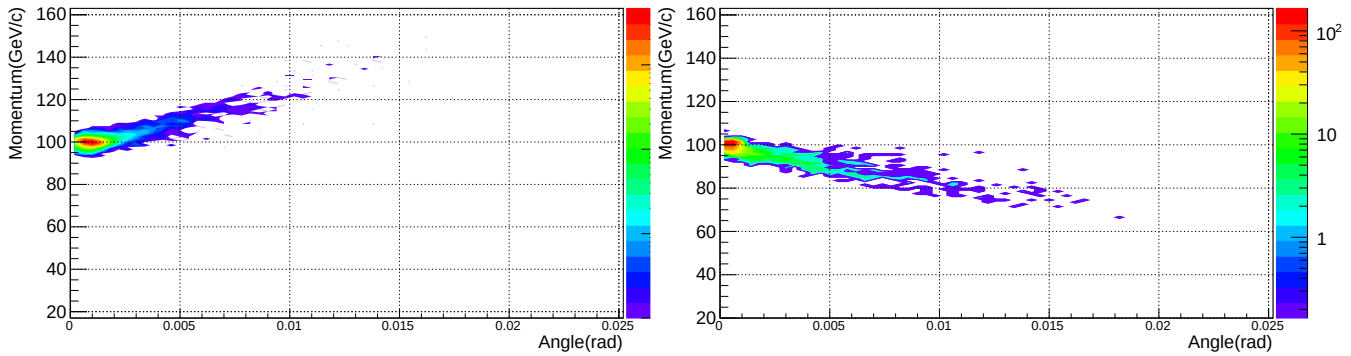

Figure 6.17: Momentum reconstructed as a function of the incoming angle for incoming particle deflected towards the negative x axis (left) and positive x axis (right).

from the energy distribution in the cells, where Δ is the half-width of the ECAL cell is the simplest method to determine the co-ordinates of high energy photons and electrons in a granular calorimeter. The reconstructed X_0 with Equations 6.2 and 6.3 as a function of the true hit co-ordinate X_e of the incoming electron beam is shown in Figure 6.21 (dots). The error bars represent the uncertainties (σ_x) in the co-ordinate reconstruction. The reconstructed X- coordinate for signal electromagnetic showers are also shown and the distributions are found to be very similar, especially for beam positioned at the boundary between cells corresponding to $X_e = 0$, where the difference due to transverse shower fluctuations should be most significant. As seen the reconstructed value X_0 is also shifted with respect to the true co-ordinate X_e of the primary beam. The non-linearity is due to the exponential nature of the function 6.2 [108] [109]. Thus it can be concluded that there's no significant difference between the signal efficiency for a given X,Y (position) cut and the pure electron efficiency for the same cut and energy deposition in the ECAL. As mentioned before since there is a probability to misidentify a hadron energy deposition as a electron event, the lateral shower shape can be used for further suppression of such events. The width of the shower is described by the dispersion [109]

$$D = \Sigma_i E_i[(X_i - X_e)^2 + (Y_i - Y_e)^2]^{1/2}/\Sigma_i E_i \tag{6.4}$$

where X_i and Y_i are the position co-ordinates of the i-th cell. As seen from Figure 6.22 that shows the distribution of the simulated $D^{1/2}$, representing the radius of the shower induced by 100 GeV/c electrons, pions and A' with mass 200 MeV in the ECAL, the signal shower is practically identical to that of an electron but differ from hadronic showers. Thus selecting the showers based on their dispersion allows one to suppress the hadron contamination further by an additional factor of 3. This selection weakly depends on the A' mass. From this study it is clear that even though the lateral shower properties are practically identical for pure electron and signal events, selection cuts on the longitudinal shower shape helps significant corrections for the signal efficiency and was used for analyzing the July' 2016 data as presented in the following sections.

6.4 HCAL and Veto Response

Precise calculation of the missing energy is essential to define the sensitivity of the experiment. Fluctuations in the longitudinal shower development and admixture of pile up

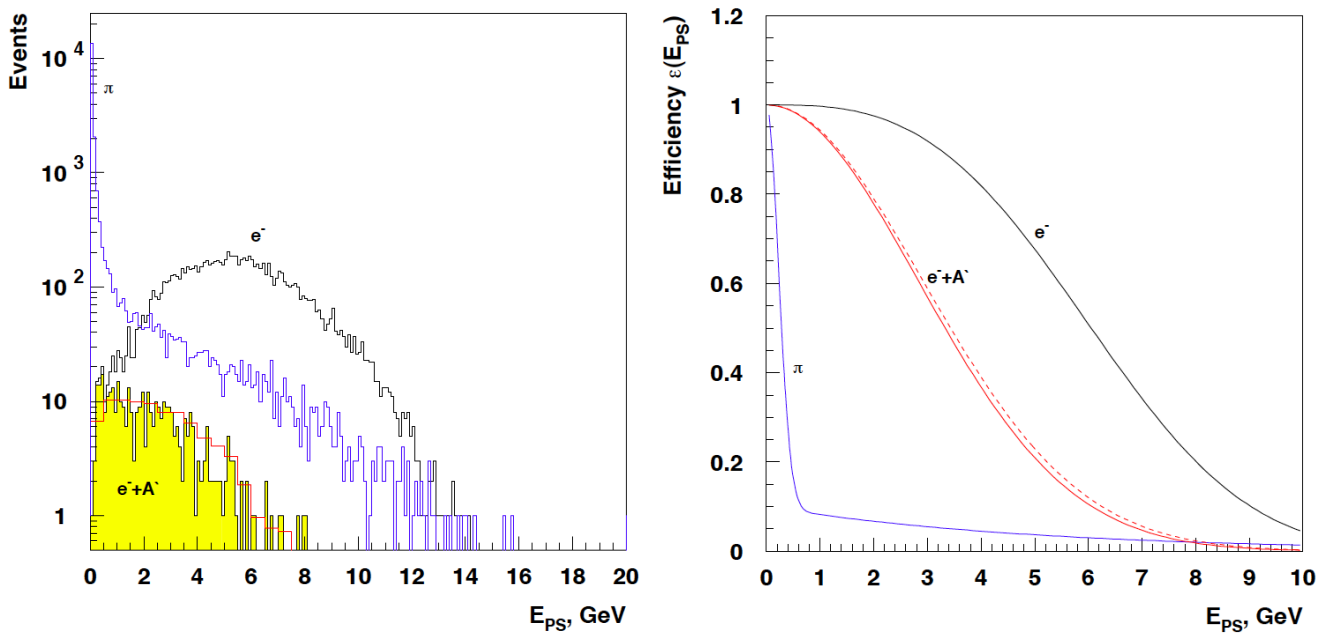

Figure 6.18: Expected distributions of the preshower energy deposit in the ECAL from 100 GeV/c pions (blue), electrons (black) and signal events for $M_{A'} = 50$ (shaded) and $= 200$ MeV (red) (left). The energy spectrum of the signal is calculated for the mixing strength $\epsilon \leqslant 1$ and $E_{miss} \geqslant 0.5E_0$. Right: Pion, electron and signal effciency for $M_{A'} = 50$ (red) and 200 (red dashed) MeV, as a function of the threshold on the E_{PS} value. [23]

events define the spread in the deposited energy of signal events in the HCAL. As described previously, the HCAL is composed of four modules arranged in a matrix of 3 × 3 cells, each cell being $7\lambda_{int}$. The leak of energy from the ECAL to HCAL is a function of the primary beam energy and in the design of the ECAL the thickness was chosen using the full shower simulation to minimize the leak into Veto and HCAL to a level $\leqslant$ 100 MeV, which is the pedestal fluctuation level in the HCAL from the electronics. Figure 6.23 shows the spectrum of the energy leak to the Veto and HCAL. Thus the design meets the requirement of having $\leqslant$ 100 MeV of energy leak. The HCAL and Veto zero energy threshold was also checked with data as explained in Section 5.1. After optimizing the selection criteria and establishing the detector performances with simulation and data, the July' 2016 run was analyzed and the results finalized for publication as described in the following Section.

6.5 Results from July' 2016 Beam time

During the July'2016 beam time NA64 operated with a beam intensity $\sim 1 \times 10^5$ e$^-$/sec/cm^2 with the full setup described in Section 5.1 including scintillators S1-S3, Micromegas trackers M1-M4, Pb-Sc ECAL, HCAL 0-3, veto V2 and Pb-Sc calorimeter as the synchrotron radiation detector collecting $n_{eot} \sim 1.88 \times 10^9$, while a smaller sample of $n_{eot} = 0.87 \times 10^9$ with a beam intensity of 2×10^4 e$^-$/sec/cm^2 was collected with the BGOs. The events were collected with the co-incidence of scintillators S1-S3 and a hardware trigger requiring an in-time cluster in the ECAL with $E_{ECAL} < 80$ GeV/c. Since the signature of A' signal is a fraction of energy, f < 0.5E$_0$ in the ECAL and missing energy $E_{miss} > 0.5$E$_0$ thereafter, the hardware trigger ensures no potential signal event is rejected since the required energy in the ECAL for a signal event given the threshold is $E_{ECAL} < 50$ GeV/c. Since the maximum DAQ

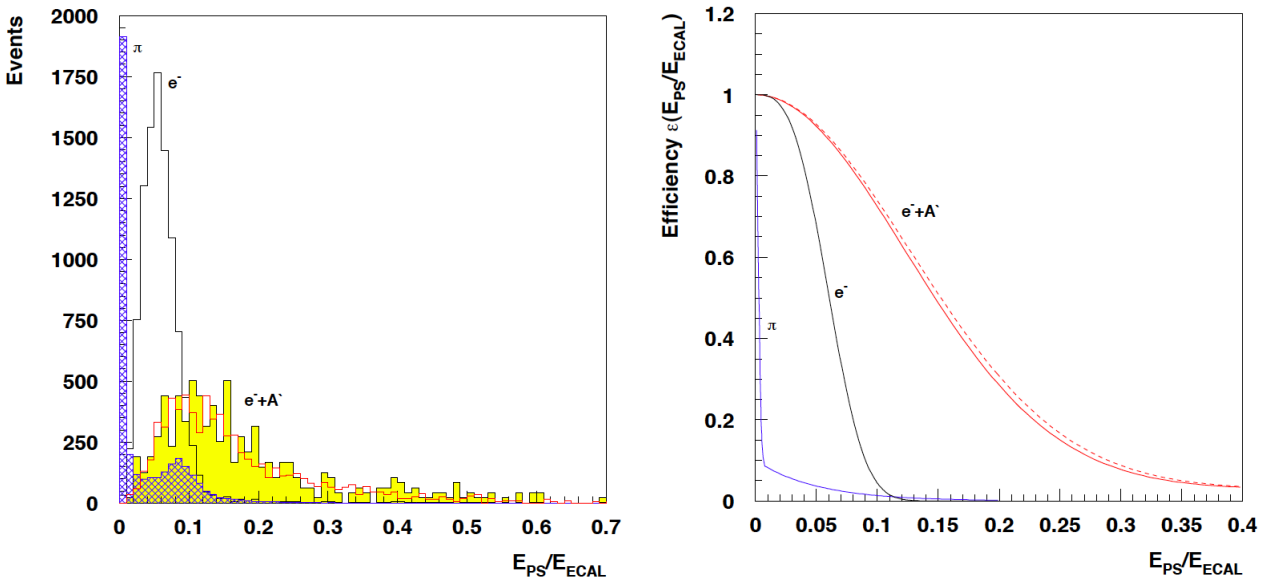

Figure 6.19: Expected distributions of the r value = E_{PS}/E_{ECAL} from 100 GeV/c pions (blue), electrons (black) and signal events for $M_{A'}$ = 50 (shaded) and = 200 MeV (red) (left). Right: Pion, electron and signal effciency for $M_{A'}$ = 50 (red) and 200 (red dashed) MeV, as a function of the threshold on the r value. [23]

rate could only reach $\sim$ 10 kHz the hardware trigger was set to reduce the acquisition rate since the energy deposition of the incoming electron follows the bremmstrahlung spectrum which falls steeply with energy. The BGO and PbSc runs were analyzed with similar selection criteria and summed up taking into account the corresponding normalization factors.

For the selection criteria optimization 10 % of the data set was used to avoid any biases while the full sample was used for background estimation. The aim of the analysis of the data set to optimize the selection cuts was to exclude all events in the signal box with $E_{ECAL} < 50$ GeV/c and $E_{HCAL} < 1$ GeV/c, until the background estimate in this region was established. As described in the previous sections detailed Geant4 Monte Carlo simulations were used to establish the detector performance, acceptance, estimate background events and suppression and eventually select cuts with the corresponding signal efficiency. A total of 2.75×10^9 n_{eot} of data set was analysed and Figure 6.24 (left) shows the distribution of E_{HCAL} vs E_{ECAL} for all events, i.e., $e^-Z \rightarrow$ anything. In order to loosely select only electron events and suppress hadron contamination, a cut on the in-time deposited energy in the SRD within the synchrotron radiation range as explained in Section 6.1 was used. This cut selected $\sim 5 \times 10^4$ events. The area labeled I in Figure 6.24 (left) originate from the rare QED dimuon production in the reaction $e^-Z \rightarrow e^-Z\gamma$, $\gamma \rightarrow \mu^+\mu^-$, wherein a hard bremmstrahlung photon converts to a dimuon pair on a target nuclei and is characterized by the energy $\sim$ 10 GeV/c deposited by the pair in the HCAL. This process helped validate the MC simulations and estimate the systematic uncertainties in the signal reconstruction efficiency in the energy range predicted by simulations. The uncertainties were also cross-checked by applying the same selection cuts on both signal and reference channels. The dimuon channel was also used as a reference for background predictions.

The area labeled II in Figure 6.24 (left) are the expected Standard Model events from the hadron electroproductions in the target. These events conserve energy with $E_{ECAL} + E_{HCAL}$

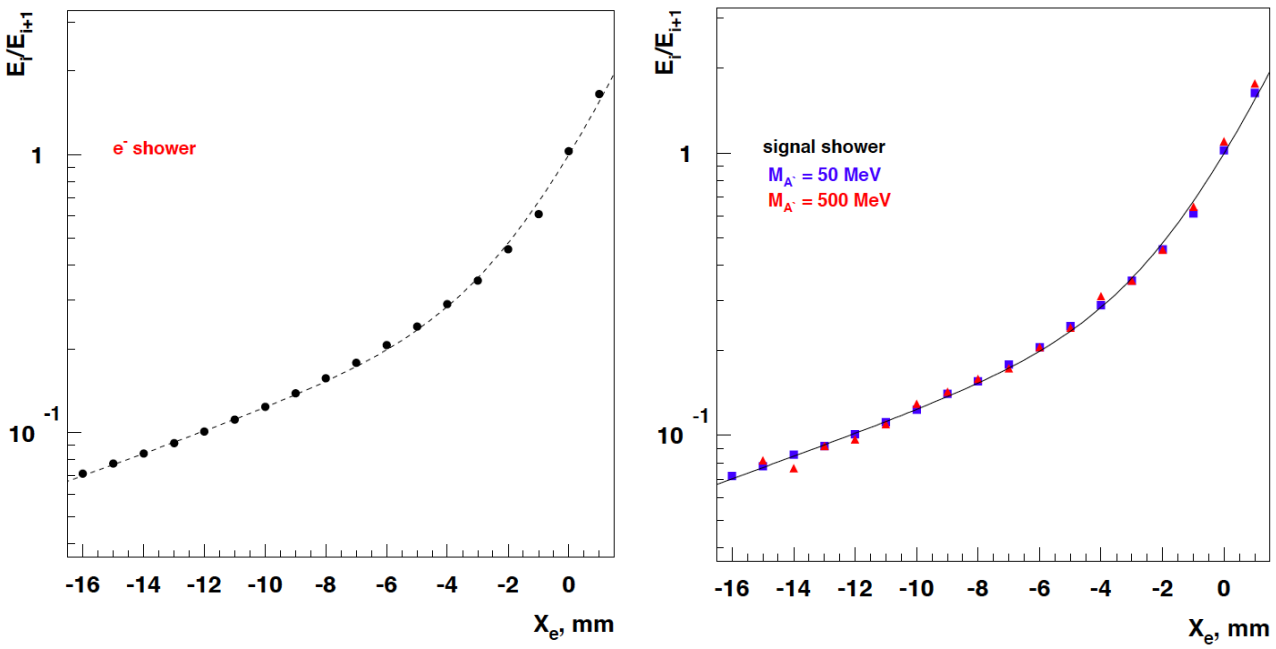

Figure 6.20: Expected dependence of the ratio E_i/E_{i+1} of the average deposited energy on two adjacent cells on the electron coordinate X_e for the electromagnetic shower induced by beam electrons without (left plot) and with (right plot) the A' emission. Shown are the simulated values fitted with a curve calculated for the lateral shower profile from Eq 2.7. [23]

$\sim$ 100 GeV/c within the energy resolution of the detectors. The area labeled III are mostly due to pile-up of e^- and hadrons and was at a level of a few 10^{-2}.

The selection criteria was chosen to maximize acceptance of MC signal events and minimize background events as is explained in the previous Sections. After optimization of the cuts the following criteria were set for the candidate events:

- Small angle of incoming track with respect to the primary beam axis to ensure collinearity of the incoming beam and reject lower energy tail, due to upstream interactions of the primary particle
- SRD energy consistent with the synchrotron radiation range of an e^- and in-time with the trigger
- Lateral and longitudinal shower shape consistent with that expected from a signal shower
- No activity in V2 and HCAL above set threshold

From the combined runs of BGO and PbSc $\sim$ 300 events passed these selection criteria. As mentioned the search is not free of background and the estimation of the probability of a fake signature needs special attention. The selection cuts were chosen to suppress all sources of background without affecting the shape of the true E_{miss} spectrum. In order to estimate the background in the signal region two methods were employed: 1) Based on the MC simulation, 2) Extracting the estimate directly from the data.

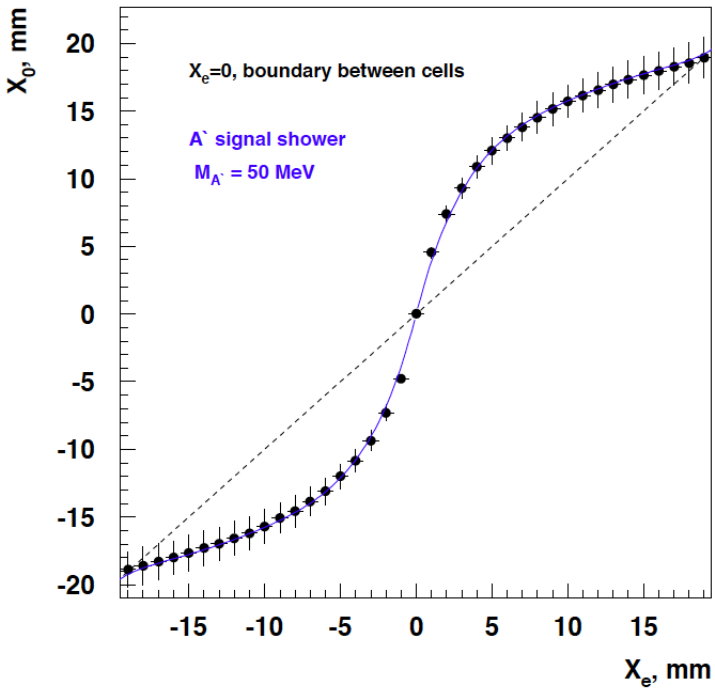

Figure 6.21: The reconstructed centre-of-gravity X_0 as a function of the true coordinate X_e of incoming electrons. The position $X_e = 0$ corresponds to the cell centre. Dots show the reconstructed values for X_0, the error bars represents uncertainties (σ_x) in the coordinate reconstruction. The curve has been calculated with Eq 6.2 for $M_{A'} = 50$ MeV. [23]

As already mentioned due to the small coupling strength of A', the signal reaction typically occurs with a rate $\leqslant 10^{-9}$/incoming electron and studying all sources of background at this level requires huge computing time and is not practically feasible. Hence, all known backgrounds were evaluated to the extent possible with MC simulations. Particle interactions or decays in the beam line, pile-up due to them, hadron punch-through from the target and the HCAL were all included in the simulation of background events. Small event-number backgrounds such as the decays of the beam μ, π, K or μ from the dimuon production were also simulated with the full statistics of the data. Large event-number processes, e.g. upstream beam interactions, punch-through of secondary hadrons were also studied extensively, although it was not feasible for the simulation statistic to be similar to the data. The uniformity scan of the ECAL target was also performed using MM3 and MM4 with an electron beam to eliminate any instrumental effects which is not present in the MC.

All background sources have been explained in 5.2 and Table 6.1 shows the estimation from MC simulations. The uncertainties in the amount of passive material in the upstream interactions and in the cross sections of the of π, K charge-exchange reactions on lead (30%) are included in the systematic error. To estimate the background directly from the data, MC signal events and extrapolated background from the sidebands A and C shown in Figure 6.24 (right) were used. Electrons in the ECAL target producing pure neutral hadronic secondaries are represented in the band A while the electron interactions in the downstream part of the beamline accompanied with bremmstrahlung photons that are absorbed in the HCAL are represented in the band C. Extrapolating the observed events to the signal region and assessing the systematic uncertainties by varying the fit models the background yield can be estimated. This method resulted in a background estimate of 0.4 ± 0.3 which, within the

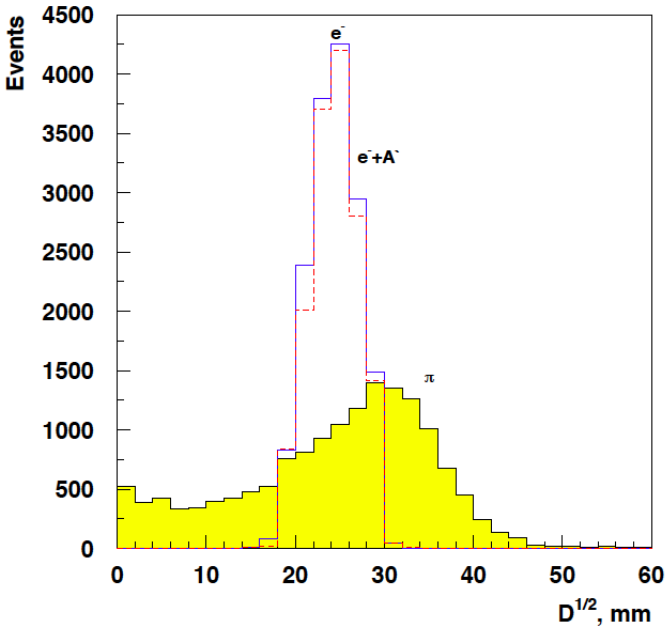

Figure 6.22: The simulated distribution of $D^{1/2}$ for showers produced in the ECAL by 100 GeV/c electron (blue), pions (yellow shaded) and signal events with $M_{A'}$ = 200 MeV (red dashed). [23]

Background Source	Events
loss of e^- energy due to punch-through γs	< 0.001
loss of hadrons from $e^-Z \rightarrow e^- +$ hadrons	< 0.01
loss of $\mu \rightarrow e\nu\nu$ decays from $e^-Z \rightarrow e^-Z\gamma$; $\gamma \rightarrow \mu^+\mu^-$	< 0.01
e^- interactions in the beamline materials	0.03
$\mu \rightarrow e\nu\nu$, π, K $\rightarrow e\nu$, K_{e3} decays	0.03
pile up of low E e^- and μ, π, K followed by their decays	0.05
μ, π, K interactions in the target	0.02
Total	0.15

Table 6.1: Expected numbers of events in the signal box from different background sources estimated for 2.75 × 10^9 eot.

errors, are in agreement with the previous estimate using MC simulations. Thus estimating the background levels and determining the selection criteria the analyzed data set was free of events in the signal box as seen and that the level of background is small is confirmed by the data.

The analysis results showed non-observation of signal events and thus a limit can be put on the ϵ, $M_{A'}$ parameter space based on the search. The number of expected signal events $N_{A'}$ for a given n_{eot} and $M_{A'}$ is:

$$N_{A'} = n_{eot}.n_{A'}(\epsilon, M_{A'}, \Delta E_{A'}).\epsilon_{A'}(M_{A'}, \Delta E_{A'}) \tag{6.5}$$

where $n_{A'}$ is the A' yield with the coupling ϵ, mass $M_{A'}$ and energy in the range $\Delta E_{A'}$, $0.5\mathrm{E}_0 < \mathrm{E}_{A'} < \mathrm{E}_0$ per electromagnetic shower generated by a 100 GeV/c electron in the ECAL corresponding to $0.5\mathrm{E}_0 < E_{miss} < \mathrm{E}_0$. The overall signal efficiency $\epsilon_{A'}$ is weakly dependent on $M_{A'}$ and $E_{A'}$ and is calculated by the product of efficiencies taking into account the geometric

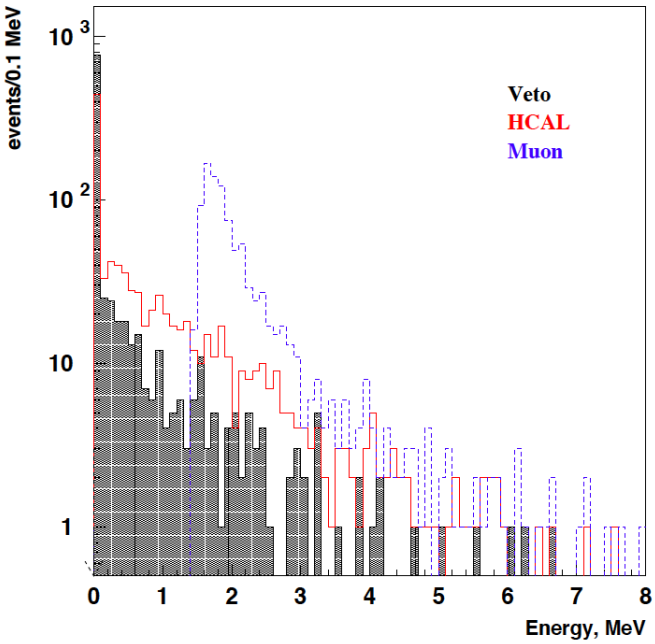

Figure 6.23: The spectrum of energy leak to the Veto and HCAL from signal events. The distribution of the energy in the Veto due to a Muon is also shown for comparison. [23]

acceptance (0.97), analysis efficiency ($\sim$ 0.8), V2 (0.96) and HCAL signal efficiency (0.94) and the acceptance losses due to pile-up ($\sim$ 8 % for BGO and $\sim$ 7 % for PbSc runs). The recorded number of reference events from the electron interactions in the target taking into account the dead time was the basis of the estimation for n_{eot}. All relevant momentum and angular distributions was taken into account to estimate the acceptance of signal events. The sensitivity of the experiment was calculated using the method described in Section 2.3.2. To estimate any additional uncertainty in the A' yield prediction a cross-check was performed between a clean sample of $\sim 5 \times 10^3$ observed and MC dimuon events with $E_{ECAL} \leqslant 60$ GeV/c which resulted in $\sim$ 15 % difference in the dimuon yield. The square of the Pb nuclear form factor $F(q^2)$ and its shape effects both the dimoun and A' yield. The accuracy of the dimuon yield for heavy nuclei can be considered the reason for the difference in the yield estimation and as the masses and q^2 ($q \sim M^2_{A'}/E_{A'} \sim m^2_{\mu}/E_{\mu}$) are similar for μ and A' this can be conservatively accounted as an additional systematic uncertainty in $n_{A'}(\epsilon,\, M_{A'},\, \Delta E_{A'})$. About 3 % uncertainty was estimated in the V2 and HCAL efficiency due to mainly pile-up effects from penetrating hadron in the the high intensity PbSc runs. About 2 % (3 %) uncertainty was estimated in the trigger (SRD) efficiency which was measured unbiased in random samples of events that bypass the trigger (SRD) selections. About 3 % (2%) uncertainty was estimated for other effects such as e^- loss due to $e^-\gamma$ pair in the upstream material. Finally, the dominant source of systematic errors on the expected number of signal events come from the uncertainty in the $n_{A'}(\epsilon, M_{A'},\, E_{A'})$ estimation (19%) resulting in $\epsilon_{A'}$ from 0.69 $\pm$ 0.09 to 0.55 $\pm$ 0.07 decreasing for higher A' masses.

Figure 6.25 shows the obtained exclusion plot with 90 % C.L. Thus the results from the July' 2016 beam run set new limits on the γ-A' mixing strength for sub-GeV A' and was able to exclude a large region of the A' favored space for the $(g\text{-}2)_\mu$ anomaly. The results were published in [26] and 10 times more statistics were also accumulated during the October' 2016 run. Detailed analysis of this data is ongoing and the results are expected to be published by

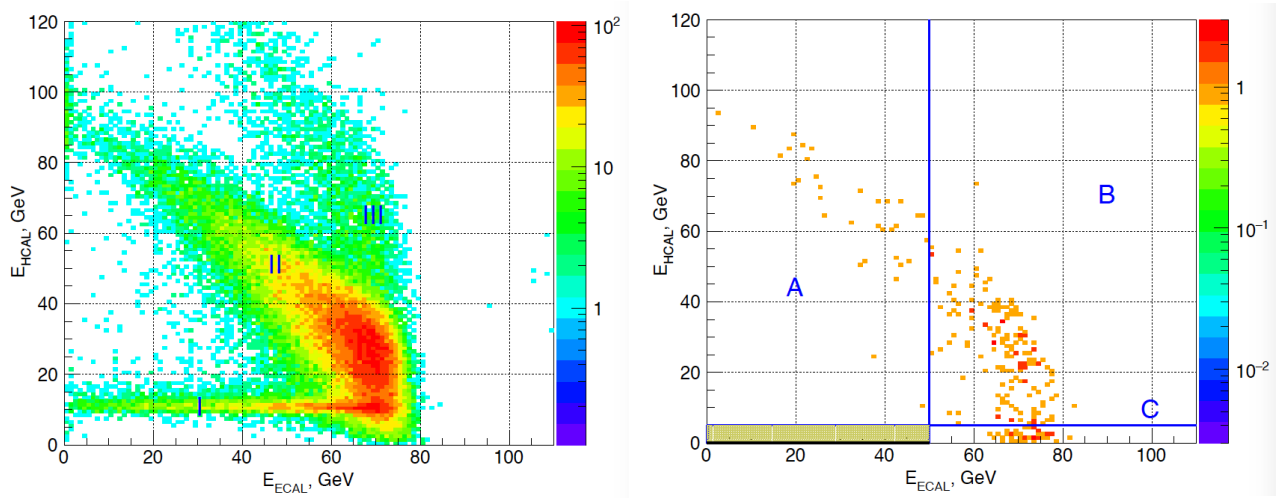

Figure 6.24: Left: E_{HCAL} vs E_{ECAL} for $e^- \rightarrow$ anything chosen loosely with the synchrotron radiation cut combining BGO and PbSc data. Right: E_{HCAL} vs E_{ECAL} after applying all selection criteria. The dashed area is the signal box region which is open. The side bands A and C are the one used for the background estimate inside the signal box. For illustration purposes the size of the signal box along E_{HCAL}-axis is increased by a factor five.

the end of 2017.

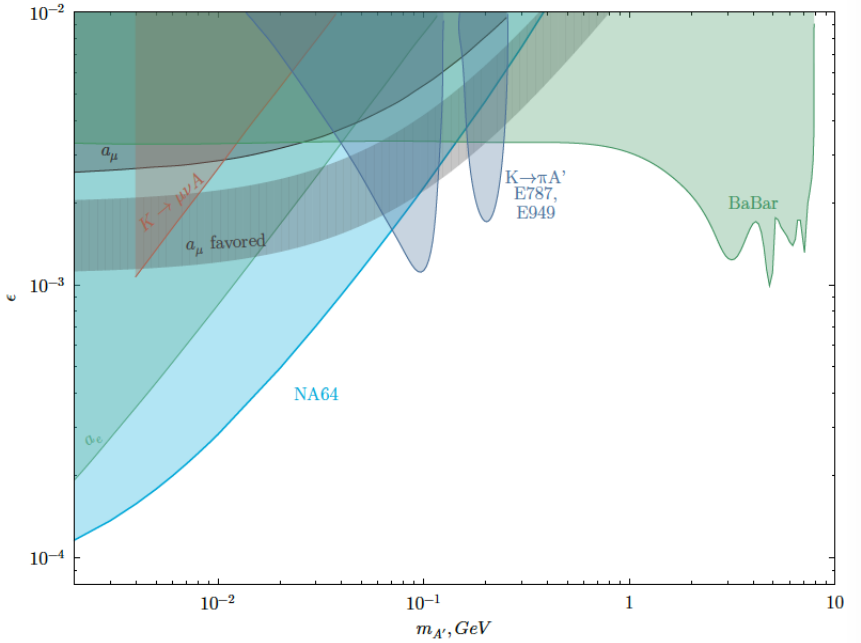

Figure 6.25: The NA64 90 % C.L. exclusion region in the ($M_{A'}$, ϵ) plane. Here, a_μ = (g_μ-2)/2

Chapter 7

GBAR setup

The GBAR experiment aims to perform a direct test of the Weak Equivalence Principle with antimatter measuring the free-fall of anti-hydrogen atoms in the gravitational field. To perform a direct measurement of the free-fall of anti-hydrogen it is necessary to achieve very low initial temperature (velocity) since its the main source of systematic uncertainty. To be able to achieve cold anti-hydrogen, GBAR aims to produce $\overline{\mathrm{H}}^+$ ions first, since ions have the advantage of being trapped in Paul traps and thus can be cooled to reach much lower temperatures, $\sim$ few tens of μK, not limited by the photon recoil (1.3 mK) as in the case of laser cooling of $\overline{\mathrm{H}}$ atoms. The $\overline{\mathrm{H}}^+$ ions are produced from the interaction of Positronium (Ps) with anti-protons from the ELENA beam at CERN as:

$$\mathrm{Ps} + \overline{\mathrm{p}} \rightarrow \overline{\mathrm{H}} + \mathrm{e}^- \tag{7.1}$$

$$\mathrm{Ps} + \overline{\mathrm{H}} \rightarrow \overline{\mathrm{H}}^+ + \mathrm{e}^- \tag{7.2}$$

Most anti-hydrogen experiments efficiently produce anti-hydrogen atoms using the three-body interaction of antiproton with two positrons, although in a highly excited state [127] [128]. For GBAR the above interaction to be exploited is also a three-body process, but because of the bound state of Ps, the cross-section is much higher. From measurements (only of Eq 7.1) or calculations of the cross-sections for these two reactions (Merrison et al [53], Mitroy [54]), one expects, e.g., for 10^7 antiprotons interacting with a 10^{12} cm^3 density positronium cloud, the production of one $\overline{\mathrm{H}}^+$ ion, together with 10^4 $\overline{\mathrm{H}}$ atoms. The number of $\overline{\mathrm{H}}^+$ may be enhanced if the positronium cloud is excited to $\mathrm{n}_{Ps} = 3$ states, where its binding energy of 0.76 eV is almost degenerate with that of $\overline{\mathrm{H}}^+$. The model then predicts gains of ~ 100 in the number of ions. The detailed description of the GBAR setup is presented below.

7.1 ELENA beam

The Extra Low ENergy Antiproton ring (ELENA) that has been built at CERN to produce low energy antiprotons is a small machine decelerating low intensity beams ($< 4 \times 10^7$ per burst) at a repetition rate of 0.01 Hz from 5.3 MeV to 100 keV. The ring was approved in June 2011 and is scheduled to start operation by August' 2017 [130]. The ring, shown in Figure 7.1, will operate with a dynamic vacuum $< 2 \times 10^{-12}$ Torr. The antiprotons will be focused and tuned using dipoles and quadrupoles comprising the electrostatic beam lines of total length > 100 m within the acceptance of the experiments. In order to optimize production of $\overline{\mathrm{H}}^+$, the anti-protons need to be further decelerated down to 1-10 keV with a decelerator placed following the ELENA beam entrance to the GBAR zone.

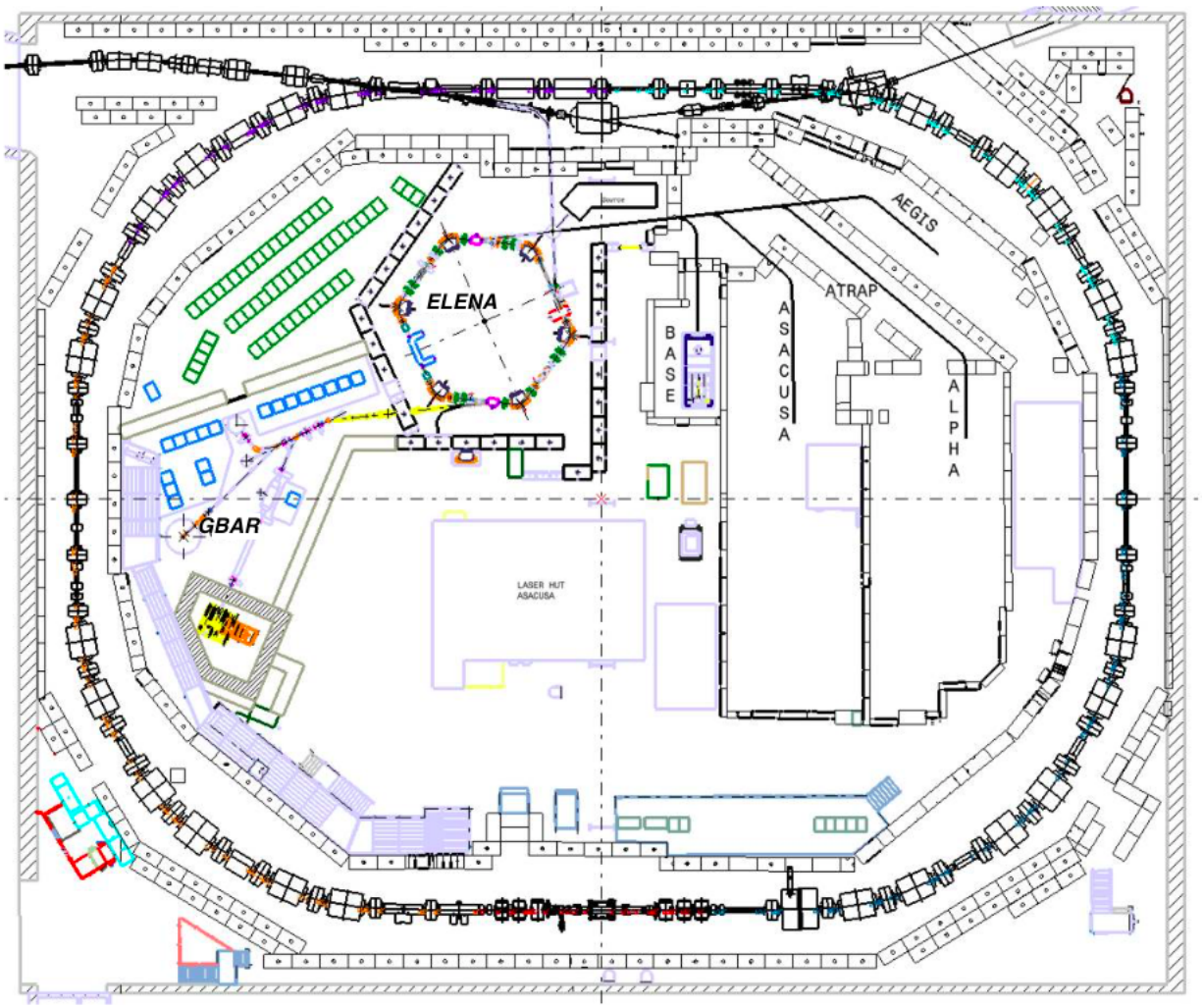

Figure 7.1: Schematic of the ELENA ring in the AD Hall at CERN

7.2 Antiproton decelerator

The CSNSM (Centre de Sciences Nuclèires et de Sciences de la Matière) team in Orsay, in collaboration with GBAR, prepared the anti-proton decelerator as shown in Figure 7.2. Such electrostatic decelerators are routinely used with heavy-ion beams at the CERN-ISOLDE facility [132]. The technique is to rapidly pulse up a beam-tube cavity from -99 kV to 0 kV while the antiproton bunch is inside it, so that the antiprotons will have 1 kV energy. However the emittance of the beam increases as the ratio of the square root of the input to the output energy. According to simulations performed, a set of electrostatic lenses allow to reach a beam efficiency of $\sim$ 30 % to pass through a 1 mm $\times$ 1 mm $\times$ 2 cm tube corresponding to the Ps target geometry [133] placed following the decelerator.

7.3 Positron-Positronium Converter

The 1 keV antiproton beam will be transported to the positronium converter to produce $\overline{\mathrm{H}}^{+}$ ions. The positronium (Ps) target is a square tube of 1 mm $\times$ 1 mm cross-section and 2 cm long as shown in Figure 7.3 internally coated with porous silica film. The porous film have been developed in collaboration with ETH, Zurich and CEA, Saclay and is expected to

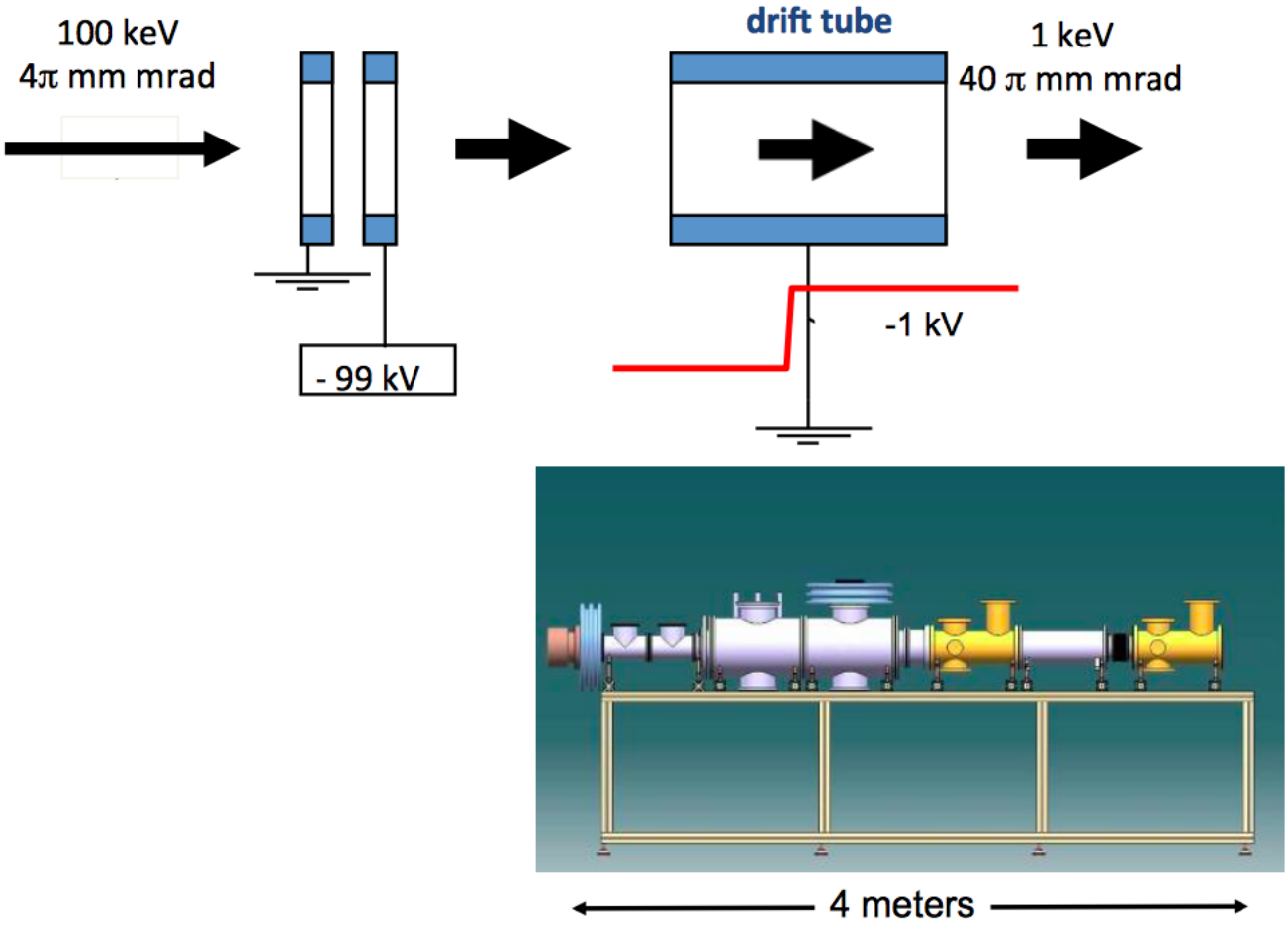

Figure 7.2: Drift tube for antiproton deceleration [133]

convert 30-40 % of the incident positrons into ortho-positronium (oPs) that returns from the surface into the vacuum [134]. As shown in [135] it would be possible to impinge the positrons through a 30 nm Si_3N_4 window inserted into one of the plates of the cylinder without any loss given the energy is above a few keV, i.e., in the efficient range of Ps conversion. The Ps, once produced inside the tube, will bounce without being annihilated due to the negative work function of the coating for Ps, thus forming a dense cloud as demonstrated at ETHZ for the Ps spectroscopy experiment [137]. The LKB laboratory in Paris has developed a 410 nm two-photon laser to excite this cloud to the 3D level of oPs [136] and a 243 nm one photon laser to excite it to the 2P level.

7.4 LINAC

The aim of the GBAR experiment is to produce at least one $\overline{H}^+$ ion per ELENA pulse (every 110 sec). This requires a slow positron flux $\sim 3 \times 10^8$/sec, which can be achieved with a standard radioactive source, for which the NCBJ (Narodowe Centrum Badań Jdrowych) group in Swierck (Poland) built the 10 MeV electron LINAC with 0.2 mA average current and a repetition rate $\sim$ 300 Hz. A tungsten target helps production of positrons via pair production which are then moderated in a tungsten mesh moderator placed close to the primary target. A demonstrator setup at Saclay to test positron production and accumulation

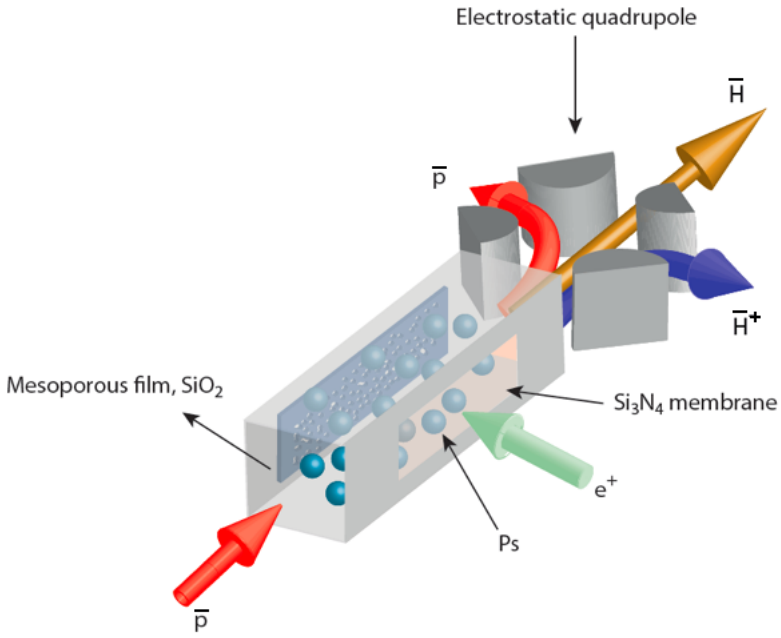

Figure 7.3: Schematic of Ps target [133]

consists of a small 4.3 MeV, 0.12 mA accelerator as shown in Figure 7.4 producing 3×10^6 e^+/sec. The positrons are transported to a Penning-Malmberg trap via positron beam lines where they are trapped using a buffer gas trap, based on electron cooling. Results of accumulation and tests are presented in [139].

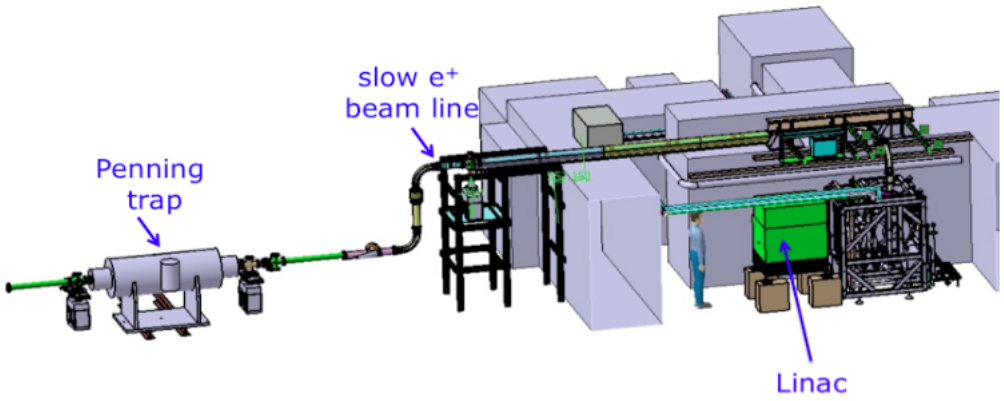

Figure 7.4: LINAC demonstrator at Saclay producing 3×10^6 e^+/sec. The final version is expected to produce 3×10^8 e^+/sec and accumulate 3×10^{10} e^+ in 110 sec

7.5 $\overline{H}^+$ trapping and cooling

After being produced the $\overline{H}^+$ will be guided and trapped in a Paul trap. Cooling of the $\overline{H}^+$ ions will then proceed in two steps: i) Doppler cooling at the mK level, and ii) Raman side band cooling to reach ~ 10 μK [140]. For the first step, the keV $\overline{H}^+$ ions are captured in a linear Paul trap, where four trap bars form a linear dynamical potential, inside which 10000 Be^+ ions are preloaded and laser cooled. This leads to the sympathetic cooling of the

anti-ions by Coulomb interactions. A short cooling time, $\sim$ to a few ms, is required to avoid photo-detachment by the cooling laser near 313 nm. From simulations [140] the mechanical coupling between Be^+ and $\overline{H}^+$ does not seem optimal with mass ratio of 9:1. However, adding HD^+ to Be^+ will result in a better coupling leading to cooling times of the order of 1 ms to reach 1 mK temperature. For the second step, a Be^+/ $\overline{H}^+$ ion pair must be transferred to a precision trap to undergo ground state Raman side band cooling [129] in order to reach the 10 μK level necessary for the free fall experiment. Mainz University (QUANTUM) is preparing the precision trap where the first tests with $40Ca^+$ and Be^+ with a mass ratio of 4.4:1 were performed. The first cooling trap is being prepared at LKB, Paris.

Once the ions are cooled and localized in the precision trap, a laser pulse will be applied to detach the excess positron (photo-detachment) as illustrated in Figure:7.5, so that the free-fall time measurement for the neutral atom can start and the atom annihilates on the vacuum cylinder bottom plate wherein the pion tracks from the annihilation are tracked with the trackers placed around the free-fall chamber.

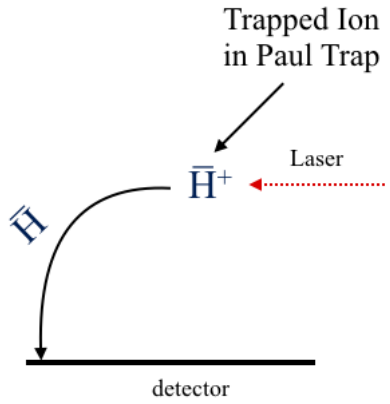

Figure 7.5: Schematic demonstrating the photo-detachment of the excess positron of $\overline{H}^+$ ion trapped in the Paul trap to start the free fall of $\overline{H}$

7.6 Micromegas Tracker

The Multiplexed XY Resistive Micromegas modules used for the GBAR experiment to track the pions from annihilation are produced at the CERN EP-DT-EF workshop. Each module is 50 cm $\times$ 50 cm with a strip pitch of 500 μm for each layer as shown in Figure 7.6 based on the MCube Detectors from CEA, Saclay [86]. The Micromegas detectors were chosen for its excellent spatial accuracy $\sim$ to a few hundred microns ($\frac{strip_{pitch}}{\sqrt{12}}$), good timing resolution $\sim$ to few tens of ns (as shown for the NA64 modules), and low material budget. Procurement and establishing the performance of these modules with simulation were the main contribution of this thesis. 50 cm prototype modules were produced for first tests. The modules are resistive same as the ones used for the NA64 experiment as described above. A way to create the optimal mapping of channel to strip was found when the number of channels, p, is a prime number [86]. The number of channels chosen for testing the prototype was 61/layer. The Micromegas module has $\sim$ 1000 strips/layer. The maximum number of strips that could be read with 61 channels is 1831, which means that only 55 % of all the available doublets were effectively used in the prototype. The repetition of k uplets, where k>2, was checked in the

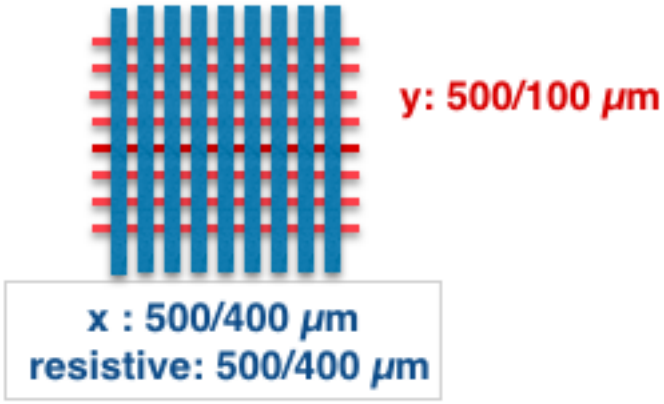

Figure 7.6: Schematic to show the strip dimensions of the GBAR Micromegas modules

sequence of channels and a careful study of the sequences proved that the smallest repeated k-uplet after optimal reordering of the map corresponds to k = 15. Thus, ambiguities in this configuration can only arise for cluster sizes above 14, which is very unlikely. A 128 channel APV chip (similar to the one used for the NA64 modules) per detector is sufficient to read all strips in both layers. Figure 7.7 shows the tentative design of the free-fall geometry with the tracker modules placed around the free-fall chamber. However, gaps due to entrance windows of the laser, entrance of the $\overline{H}^+$ ions etc are not included. Due to the low rate of the signal for the experiment of ~ 0.01 Hz the main background is expected from cosmic rays. The tracker modules placed around the free-fall geometry are meant to help suppress this background as well. In order to have a first estimate of the geometry of the free-fall chamber, the expected resolution of tracking and the subsequent calculation of $\overline{g}$ with efficient suppression of the cosmic background, the free-fall of the anti-hydrogen was simulated taking into account the geometric acceptances of tracking (without considering the laser windows, $\overline{H}^+$ entrance gaps, Paul trap acceptances etc), initial temperature of the atom, recoil from the laser, precision on the free-fall time and vertex reconstruction. Cosmic background was also simulated to track the cosmic events and check the suppression factor. Developing the simulation package and helping guide the finalization of the free-fall geometry with the results from simulation was one of the tasks of this thesis. The simulation and the results are presented in the following chapter.

7.7 Cosmic Test Bench

A prototype of a 50 cm × 50 cm triplet of MM modules, as shown in Figure 7.8, is produced and being set up at the GBAR experimental zone in the AD Hall. Following that the triplet will be characterized with a radioactive source following the method described in Section 5.1.5.1 and its performance will be checked for tracking cosmic events. The Micromegas detectors will be read by the APV25 chips, recieving the trigger, which should be a NIM signal, from the scintillators surrounding the detector. A latency of 1 μs will be sufficient.

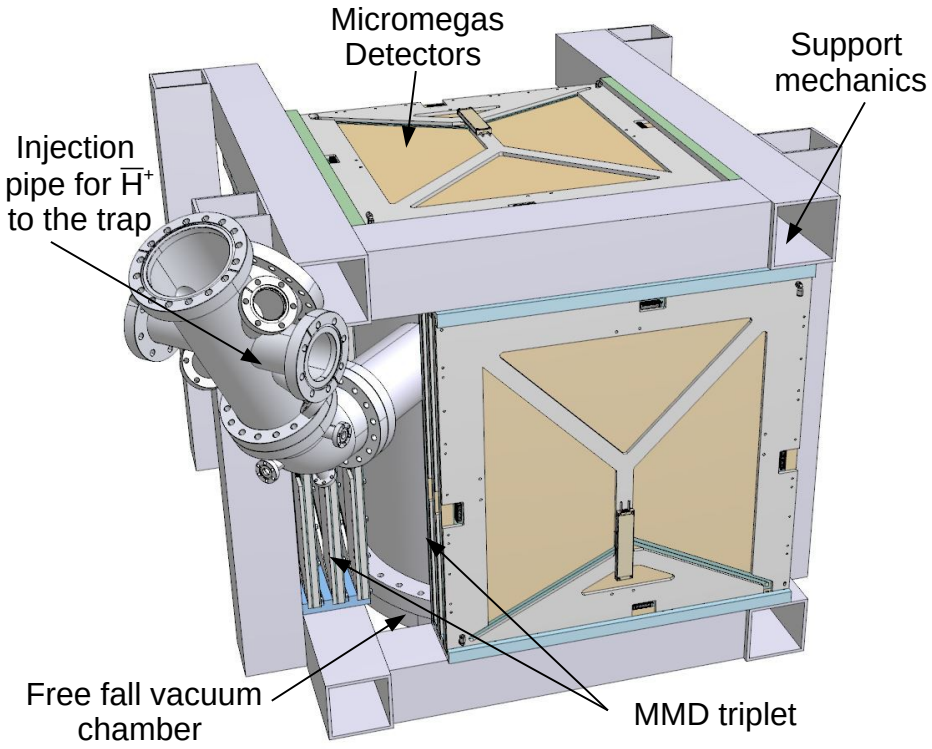

Figure 7.7: Tentative scheme of the GBAR free-fall geometry with triplets of MM modules around the vacuum vessel

The chip will be read by the DAQ system of scalable architecture, the so-called Scalable Readout System (SRS), developed by the RD51 collaboration at CERN [146]. The details of the readout is presented in the following section.

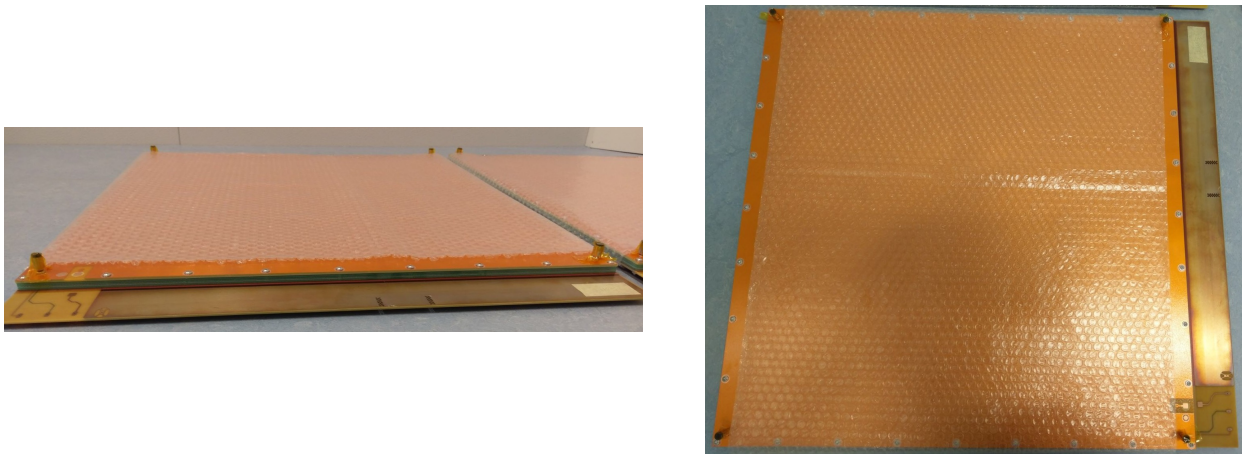

Figure 7.8: Prototype of 50 cm × 50 cm Micromegas modules

7.8 Readout Electronics

The SRS architecture is a table-top electronics readout composed of a front-end ASIC (APV25) interfaced to an adapter card via HDMI link, which digitizes the data stream for

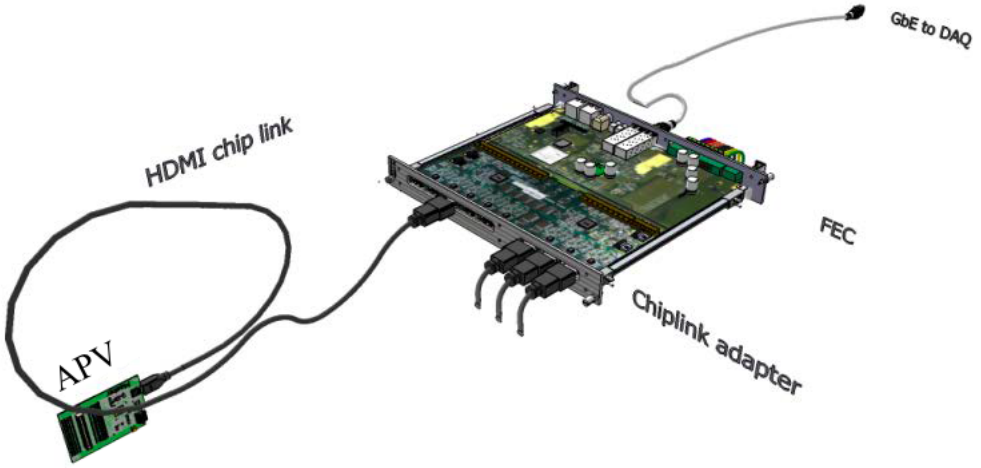

Figure 7.9: Schematic of the DAQ with SRS taken from [146]

FPGA processing on the common front-end concentrator (FEC) card [148] - [150]. The FEC communicates with DAQ PC via a Gigabit Ethernet cable as shown in Figure 7.9. For small systems consisting upto 4k readout channels the SRS is powered by a 5 kg Mini-Crate as shown in Figure 7.10. One ATX (Advanced Technology Extended) power supply and an ATX adapter is integrated in the Mini-Crate with one FEC/ADC combination by default which has 8 HDMI links. Each Mini-Crate can be upgraded to hold up to 2 FEC/ADC combination however. The zero suppression algorithm is also added to the firmware allowing high data

Figure 7.10: The 5 kg Mini-Crate to power the SRS Frontend. [146]

acquisition rates $\sim$ to a few kHz. The zero suppression algorithm ensures all unimportant data is suppressed thus improving the DAQ rate. The selection is done comparing the integral of the pedestal corrected signal from the given channel with the pedestal variation (σ) of each channel. The pedestal therefore need to be recorded earlier and stored in the FEC. The pedestal can be accessed for READ/WRITE processes via slow control and the threshold, x, for the selection, where the signal is over $x\sigma$, is programmable via slow control as well.

Chapter 8

Simulation of the GBAR tracker and optimization of the free fall geometry

The statistical uncertainty on $\overline{g}$ is a function of the initial parameter of the anti-atom as described in Chapter 4. The optimal design of the free-fall geometry is the one that would require the least number of atoms to reach a relative precision of 1 % on $\overline{g}$ (as is the aim in the first phase) and that would efficiently reject background from cosmic rays. Before simulating the anti-hydrogen free-fall and tracking of the pions from annihilation to estimate the required dimensions of the geometry and tracking resolution, the material of the free-fall cylinder was studied with ANSYS to comply with the CERN safety rules.

8.1 ANSYS study of free-fall cylinder

The free-fall chamber is meant to be under vacuum pressure to minimize all interactions of the anti-hydrogen atom during the free-fall. Therefore, one should ensure that the thickness and material of the vessel comply with the safety rules of CERN. The safety rules of CERN states that stresses generated by the applied load shall remain below the elastic range and the equipment shall be checked to demonstrate that no buckling occurs [141]. In addition to the safety standards the thickness of the vacuum chamber is desired to be as thin as possible to reduce interaction of the pion tracks which worsens the resolution on the vertex reconstruction.

Since the prototype tracker modules produced is $\sim$ 50 cm $\times$ 50 cm, to start, the thickness and material of a 50 cm height and 50 cm diameter vacuum cylinder was simulated under vacuum pressure to estimate the minimum required thickness that will withstand the pressure. These feasibility studies were performed with ANSYS. The required thickness was determined by evaluating the deformation of the chamber under vacuum pressure. The results of the simulation are presented in Table:8.1.

The results show that we have two options for the free-fall cylinder, requiring the least deformation and that the maximum stress do not exceed the elastic limit of stress $\sim$ 200 MPa [142] to prevent plastic deformation. The two choices thus are a 3 mm round-bottom or a 4 mm flat-bottom Stainless Steel cylinder. With the 3 mm round-bottom, however, the geometry will add a maximum of 4 cm gap between the cylinder bottom plane and the tracking chambers placed below the cylinder, due to the curvature of the bottom plane. To reduce the effect of the longer lever arm as a result of this gap and keep the tracker planes as

	Stainless Steel			Titanium		
	3mm Round-Bottom	3mm Flat-Bottom	4mm Flat-Bottom	3mm Round-Bottom	3mm Flat-Bottom	4mm Flat-Bottom
Maximum Stress (MPa)	37.564	307.96	144.97	24.845	303.26	144.24
Maximum Deformation (mm)	0.068	4.350	1.934	0.090	8.417	3.746

Table 8.1: Summary of ANSYS simulation

close as possible to the bottom plane the 4 mm flat-bottom stainless steel detector with a 2 mm deformation seems the preferred solution. Figure:8.1 shows the result of the ANSYS study for a 4 mm Flat-Bottomed vacuum cylinder with the maximum deformation $\sim$ 2 mm at the centre of the bottom plane. Based on the results of the ANSYS simulation a Stainless

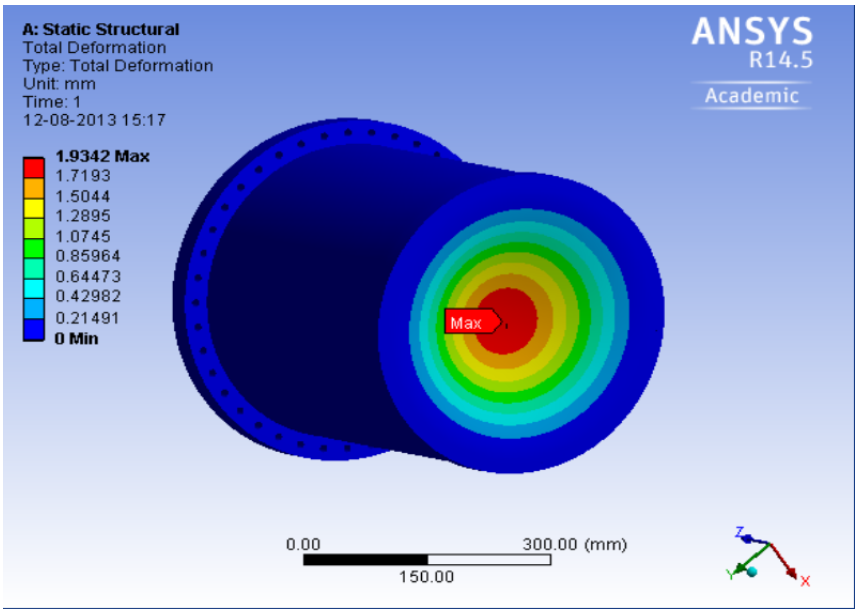

Figure 8.1: ANSYS study of a 4mm Flat-Bottomed Vacuum cylinder showing the deformation under vacuum

Steel vacuum cylinder with 50 cm height and 4 mm thick walls was used for the presented Geant4 simulations. The free-fall geometry included in the simulation did not include losses due to the Paul trap acceptances and laser windows and entrance valves for $\overline{\mathrm{H}}^{+}$. All other parameters including the initial state of the antihydrogen atom, recoil from the photo-detachment laser, tracking acceptances was included. The anti-hydrogen free-fall including the shaper scheme was also performed to cross-check the theoretical calculations of statistical precision presented before. The Cosmic background suppression was checked with tracking using the CRY package linked to the Geant4 simulation.

8.2 Simulation of $\overline{\mathrm{H}}$ annihilation

The free-fall and the subsequent annihilation of $\overline{\mathrm{H}}$ atoms was simulated with Geant4 taking all effects into consideration except the Paul trap acceptances. The initial parameters used for the $\overline{\mathrm{H}}$ atom was T = 10 μK, ΔE= 15 μeV above the photo-detachment threshold, Δt = 100 μs (time resolution from laser). Figure 8.2 shows the distribution of the horizontal velocity

after photo-detachment from simulation. The mean of the distribution $\sim$ 1 m/s matches the theoretical calculation presented before. Figure:8.3 shows the spread of the vertical velocity of the atom and the $\sigma \sim 0.3$ m/sec gives the velocity dispersion for the vertical velocity. From Eq 3.6 it is clear that the error on $\overline{g}$ is inversely proportional to the free-fall height and will improve for higher free-fall height. However, higher the free-fall height more atoms are expected to hit the side walls, depending on the radius of the cylinder, which may limit the resolution on the free-fall height reconstruction due to the longer lever arm which is an effect of the curved surface of the cylinder wall. An optimum setup is the one that requires the least number of $\overline{\mathrm{H}}^{+}$ ions, i.e., a minimum sample size, to reach a relative precision of 1 % on $\overline{g}$. Therefore, in order to optimize the free-fall height and radius of the free-fall chamber the figure of merit that should be minimized for this study is given by:

$$\text{No. of events req.} = \frac{1}{(10^{-2})^2} \times \frac{1}{\text{Acceptance}} \times (\frac{\Delta\overline{g}}{\overline{g}})^2 \tag{8.1}$$

This figure was checked for different geometric configurations taking into account all acceptance losses due to the geometry, tracking resolution and initial parameters of the atoms. Figure 8.4 shows the Geant4 geometry used for the simulation of the free-fall of anti-hydrogen

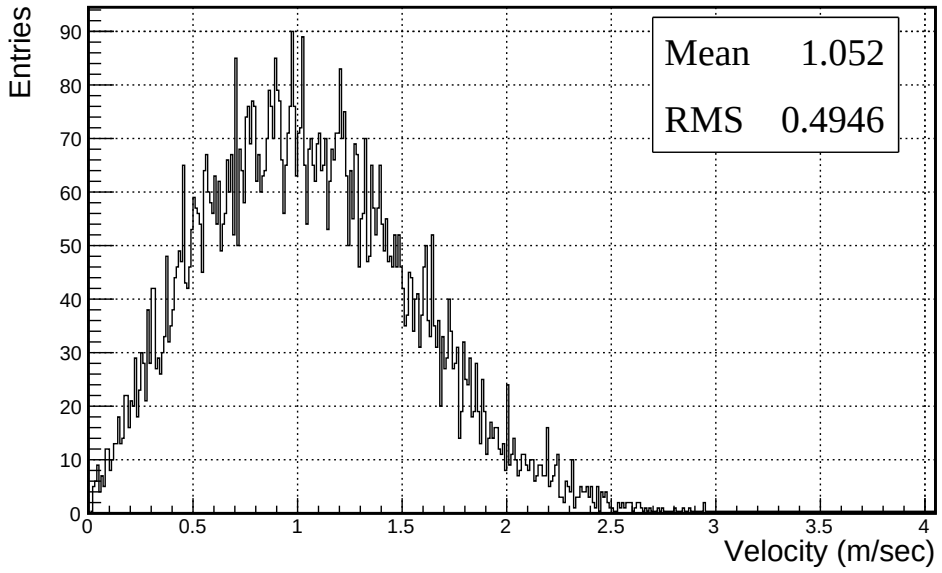

Figure 8.2: Horizontal velocity with mean = 1.05 m/s from simulation for initial temperature T = 10 μK and laser energy 15 μeV above photo-detachment threshold.

in a 50 cm height vacuum cylinder. Figure 8.5, 8.6 8.7 shows the top view of the geometry for 20 cm, 25 cm and 30 cm radius free-fall cylinder with 50 cm $\times$ 50 cm Micromegas placed around the cylinder (the figures do not show the top and bottom triplets to show the top cross-section). The Micromegas modules in each triplet were placed 5 cm from each other. The multiplicity of charged pion tracks obtained from the Geant4 simulation for anti-proton annihilation at rest on the Stainless Steel cylinder is as shown in Table:8.2. Nuclear fragmetation due to the produced pions from annihilation being absorbed by the nucleus of the target material has been studied extensively [143] [144]. This will cause a decrease in the number of produced pions. To validate the simulation antiproton annihilation was simulated on a Hydrogen Target that produced a double track efficiency of 86.61 % which matched the

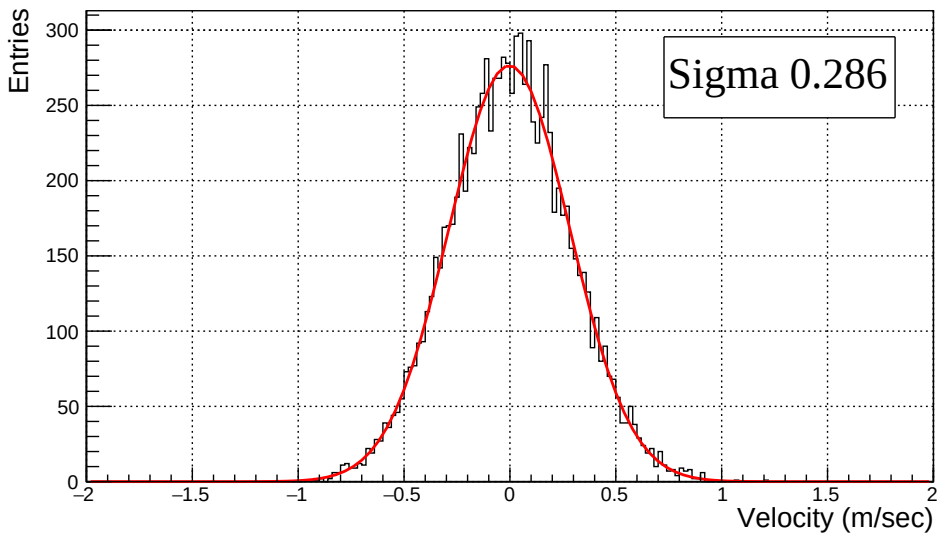

Figure 8.3: Vertical velocity dispersion from simulation for initial temperature $T = 10\ \mu K$ and laser energy 15 μeV above photo-detachment threshold. The black histogram is the simulated data and the red line is the fitted histogram with parameter "Sigma". "Sigma" = 0.286 m/s gives the vertical velocity dispersion

Table 8.2: Charged Pion multiplicity with the Geant4 simulation

>= 1 track	94 %
>= 2 tracks	85 %
>= 3 tracks	63 %
>= 4 tracks	30 %

results of 86 % from the Crystal Barrel experiment [145]. There were no available data for heavier targets but the agreement of the Hydrogen data helped validate the simulation channels. To form a track a hit on at least two of the modules in a triplet is necessary. The hits on the triplet modules are recorded from Geant4 and fitted with a 3D track. The tracks are then extrapolated to the cylinder volume to get the average vertex position calculated from at least two or more tracks. The efficiency of track fitting, i.e., the efficiency of fitting the track and reconstructing a vertex on the cylinder walls or the bottom plates was checked to be $\sim$ 97 %. The resolution of vertex reconstruction from the pion tracks through the triplets thus obtained was checked as a function of the cylinder thickness as shown in Figure:8.8. As expected the resolution worsens for thicker cylinders due to more multiple scattering. The resolution of reconstruction $\sim$ 0.4 mm was obtained for the 4 mm thick case which was used for the following presented Geant4 simulations. The geometric acceptance of tracking at least two pion tracks/$\overline{\mathrm{H}}$ annihilation was checked for different cylinder radii and free-fall height as shown in Figure 8.9. As expected the acceptance is better for smaller radius and height of free-fall due to better coverage by the tracker modules. For 20 cm radius cylinder the geometric acceptance does not change much for different free-fall heights as expected with 50 cm $\times$ 50 cm MM modules. However, as the radius increases to 25 cm and 30 cm the acceptance drops a little with increasing height. The error on the reconstructed $\overline{g}$ was also checked taking into account the initial parameters of the atom and the vertex height reconstruction resolution. 10000 $\overline{\mathrm{H}}$ atom annihilation was simulated and Figure 8.10 shows the standard error, $\sigma_{d\overline{g}/\overline{g}}$ for the different cylinder radii and free-fall height obtained from the

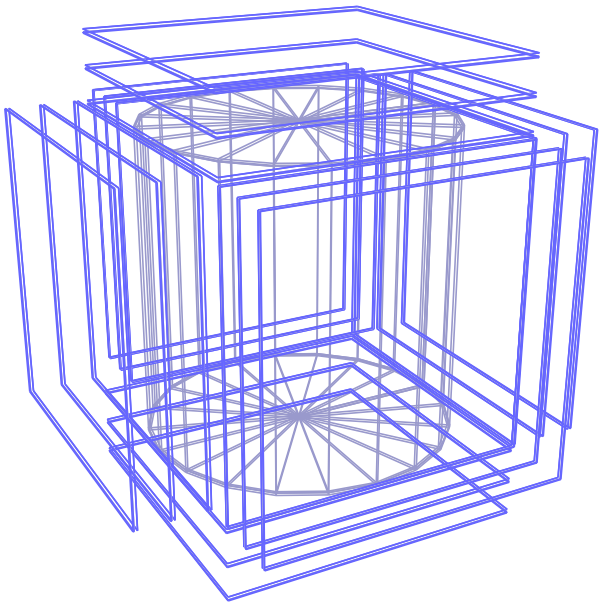

Figure 8.4: Geant4 Geometry used for simulation with Micromegas modules placed around the free-fall cylinder

reconstructed free-fall height and time where $d\overline{g}$ = True $\overline{g}$ - Reconstructed $\overline{g}$. The relative precision is given by $\sigma_{d\overline{g}/\overline{g}}/\sqrt{N}$ where N is the sample size (detected events depending on the acceptance). As expected from the uncertainty calculation the standard error improves with higher free-fall height for all radii and is not limited by the vertex reconstruction resolution. Taking into account the geometric acceptance and the standard error on $\overline{g}$ reconstruction obtained from the reconstructed free-fall height for different cylinder radii and free-fall heights, the required number of events to reach a relative precision of 1 % was calculated from Eq 8.1. Figure 8.11 shows the required number of events for the different free-fall configurations. As seen, the optimum setup seems to be a 25 cm radius cylinder and a 25 cm free-fall height since the gain in the number of required events with a 30 cm radius cylinder is only $\sim$ 1 %. Figure 8.12 shows the annihilation position on the 25 cm radius cylinder on the XY (left) and XZ (right) plane. In the simulation geometry the centre of the co-ordinate system was the center of the bottom plate of the free-fall cylinder. As seen there are few events that hit the side walls (z>0) and the annihilation position is biased towards the positive X direction due to the photo-detachment and recoil due to the laser, as is expected. Figure 8.13 shows the distribution of free-fall time of the $\overline{\mathrm{H}}$ atom for the 25 cm free-fall case in a 25 cm radius cylinder. Figure 8.14 shows the distribution of the reconstructed $\overline{g}$ with a mean of -9.84 m/s^2 for the fitted gaussian. For completeness the case of 30 cm radius cylinder with 60 cm $\times$ 60 cm Micromegas modules was also checked. Figure 8.15 shows the comparison of acceptance (left) and relative precision (right) obtained for 1500 detected events as a function of the free-fall height for a 25 cm radius cylinder with 50 cm $\times$ 50 cm Micromegas modules and a 30 cm radius cylinder with 60 cm $\times$ 60 cm Micromegas modules. The improvement in the geometric acceptance with 60 cm Micromegas modules for 30 cm radius free-fall cylinder is

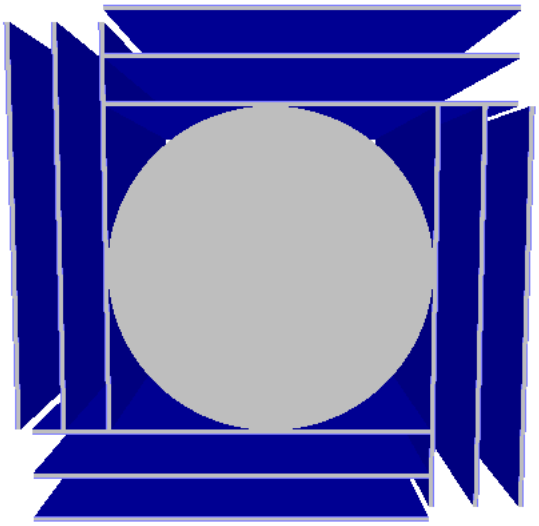

Figure 8.5: Top view of 40 cm free-fall cylinder Geant4 Geometry used for simulation with Micromegas modules placed around it

only $\sim$ 3 % and the improvement in the relative precision for the same number of detected events is $\sim$ 6 % compared to a 50 cm cylinder with 50 cm Micromegas modules.

8.3 Background Rejection with Micromegas tracking

The main source of background in the GBar experiment are cosmic events. In order to estimate the background rejection, cosmic events were simulated with the CRY package [147] for the 25 cm radius cylinder and 50 cm $\times$ 50 cm Micromegas modules geometry. The cosmic tracks were tracked with the Micromegas modules and the angle between the tracks through the different triplets was reconstructed. In case of more than two tracks, the pair of tracks with the closest reconstructed vertices to each other on the cylinder volume was selected and the angle between them was selected for that event. For cosmic events the tracks should be predominantly straight through the different triplets unlike pion tracks from signal events. Therefore, the angle between the tracks is a good tool to reject cosmic rays. Figure 8.16 shows the distribution of angle between tracks through different triplets for cosmic (left) and pion events (right) with a peak at 180° for cosmic tracks and pion tracks having a flat distribution of angles. Figure 8.17 and Figure 8.18 shows the background rejection and signal efficiency respectively as a function of the angle cut, *Angle cut*, where events with the reconstructed angle $<$ *Angle cut* are accepted. Figure 8.19 (left) shows the ROC curve (receiver operating characteristic curve) of the true positive rate as a function of the false positive rate for different angle cuts. The rate of events for cosmic rays with a track passing through two triplets is $\sim$ 20/sec from simulation. In the 200 ms window, which is the average free-fall time of the anti-hydrogen atom for 25 cm free-fall, the number of expected cosmic events is $\sim$ 4. Figure 8.19 (right) shows the Signal efficiency as a function of the S/B (Signal/Background) ratio for different angle cuts. For example for an angle cut of $<$ 170° the S/B ratio is $\sim$ 45 in the time window with a Signal Efficiency $\sim$ 97 %. The double track efficiency for pions for this geometric configuration as shown before is $\sim$ 68.5 % and taking into account the signal efficiency for the given cut the resulting detection efficiency comes out to be $\sim$ 67 %. The final number of trapped $\overline{\mathrm{H}}^{+}$ ions that will be required for the aimed

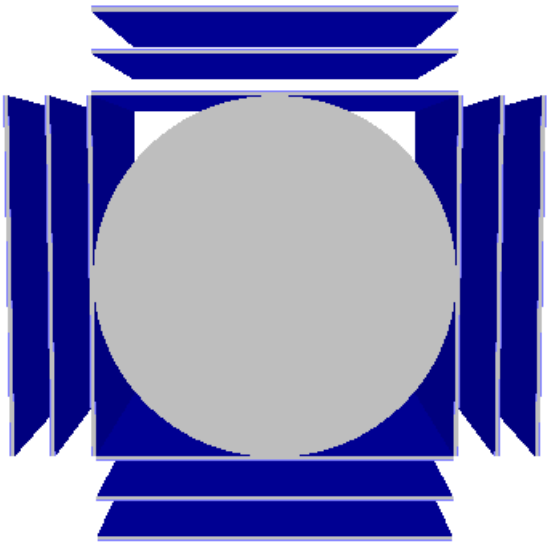

Figure 8.6: Top view of 50 cm free-fall cylinder Geant4 Geometry used for simulation with Micromegas modules placed around it

precision after this angle cut is $\sim$ 1445.

8.4 Shaper Simulation

Since the relative precision is limited predominantly by the initial velocity dispersion of the atom, a scheme has been proposed to shape the vertical velocity as mentioned. A shaper with a mirror surface on the bottom and a rough top surface as shown in Fig. 3.4 is proposed to be used which help reduce the initial velocity dispersion due to the high efficiency of quantum reflection at small energies because of the Casimir interaction. Using this scheme requires a knowledge of the time spent in the shaper by the anti-atom which is derived from the calculation of the horizontal velocity that sets a limit on the vertex reconstruction resolution as presented in Chapter 3. 10000 anti-hydrogen ions was simulated following the photo-detachment and the motion of the anti-atom through the shaper was simulated taking into account all initial parameters of the atom as before as well as the probability of loss on the mirror surface with the shaper scheme. The reflection probability corresponding to reflection on a silica mirror corresponding to the Figure 3.6 as presented before was used for the simulation. The r_{in} was fixed at 1 mm and r_{out} was fixed at 25 mm as starting values, with the free-fall height, H = 25 cm and detector radius, R = 25 cm. Figure 8.20 shows the acceptance of events through the shaper as a function of the height h. As expected thinner the shaper lesser events survive, as most annihilate on the absorber before passing the shaper. However, as seen from Figure 8.21 thinner the plate the relative error, $\sigma_{dg/g}$, improves due to smaller dispersion in the initial velocity. Thus, even though using a very thin shaper reduces the acceptance of events, the improvement in the resolution on the reconstructed $\overline{g}$ results in much less required events to reach a relative precision of 1 %, thus improving the figure of merit as shown below. A very thin shaper of h = 50 μm was simulated for different r_{in} and r_{out} to estimate the optimum case minimizing the figure of merit. The figure of merit was also checked for different resolution on the vertex reconstruction to estimate the required resolution. Figure 8.22 shows the Figure of merit as a function of r_{in}. r_{out} was fixed at 25

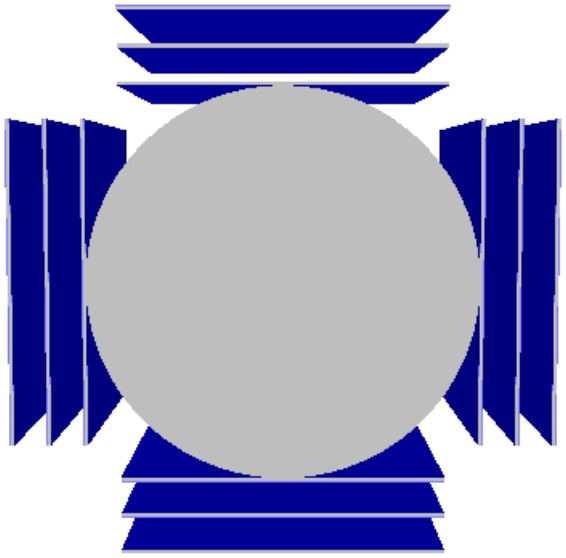

Figure 8.7: Top view of 60 cm free-fall cylinder Geant4 Geometry used for simulation with Micromegas modules placed around it

mm. As seen the shaper needs to be as close as possible to the Paul trap for optimum operation. Figure 8.23 shows the Figure of merit as a function of r_{out} keeping $r_{in} = 1$ mm. As seen the optimum setup is when $r_{out} \sim 6$ mm, i.e., for a thin and short shaper a simple solid angle limitation can do most of the selection to reduce the dispersion on the initial velocity. As an example the r_{in} was fixed at 1 mm with r_{out} at 6 mm and the Figure of merit was also checked for different vertex reconstruction resolution. Figure 8.24 shows the Figure of merit as a function of the vertex reconstruction resolution. As seen a few mm resolution is sufficient for the shaper. As presented before the resolution of vertex reconstruction obtained from simulation with the Micromegas trackers is ~ 0.4 mm which is more than enough for the shaper scheme.The results show with a thin and short shaper the statistics needed is quite low to reach the aimed relative precision. The plots presented takes into account the double track efficiency presented before. Figure 8.25 shows the distribution of the reconstructed $\overline{g}$ with the above scheme. The required number of trapped $\overline{\mathrm{H}}^{+}$ ions to reach a relative precision of 1 % using a thin and short shaper thus reduces to ~ 103 from ~ 1445 without shaper, taking into account the 97 % signal efficiency for the quoted angle cut to reject cosmic background.

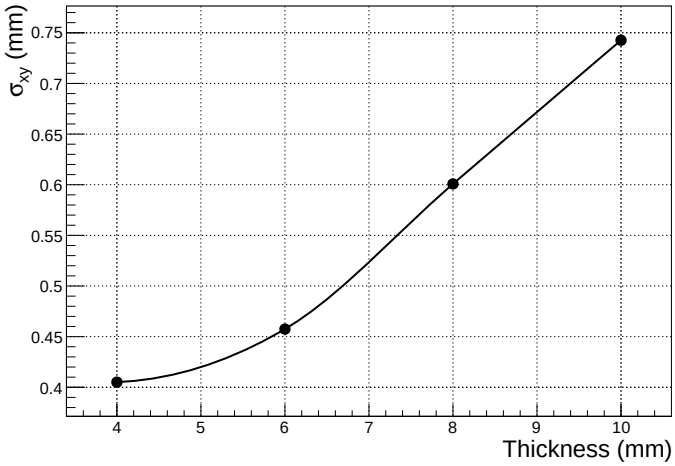

Figure 8.8: Resolution of vertex reconstruction in X and Y co-ordinates as a function of the cylinder thickness.

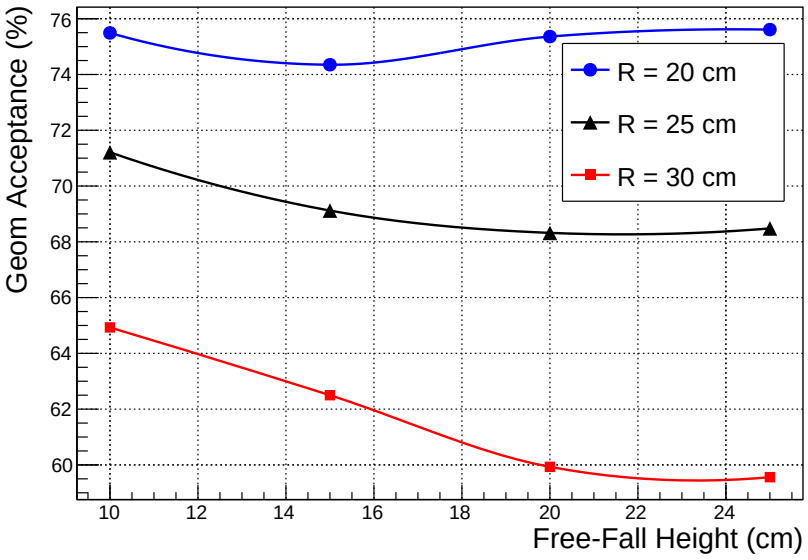

Figure 8.9: Acceptance of tracking at least two pion tracks for different cylinder radii and free-fall height

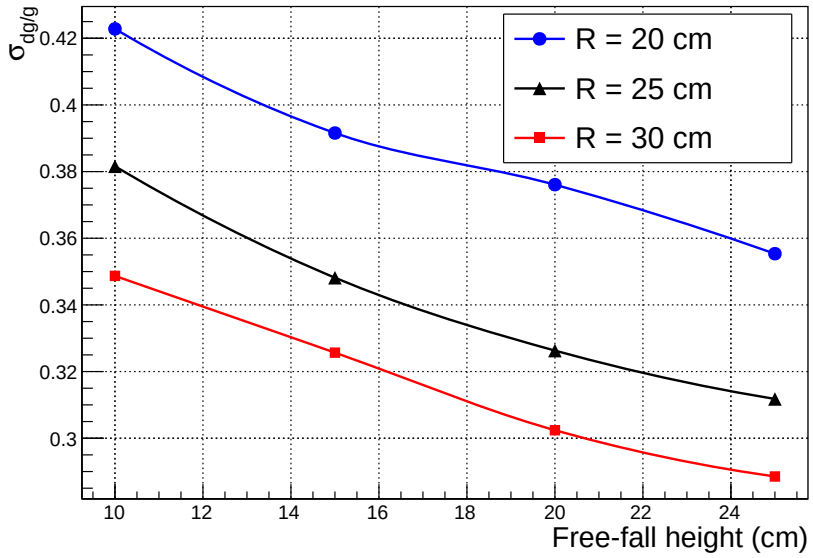

Figure 8.10: $\sigma_{d\bar{g}/\bar{g}}$ as a function of the free-fall height for different cylinder radii

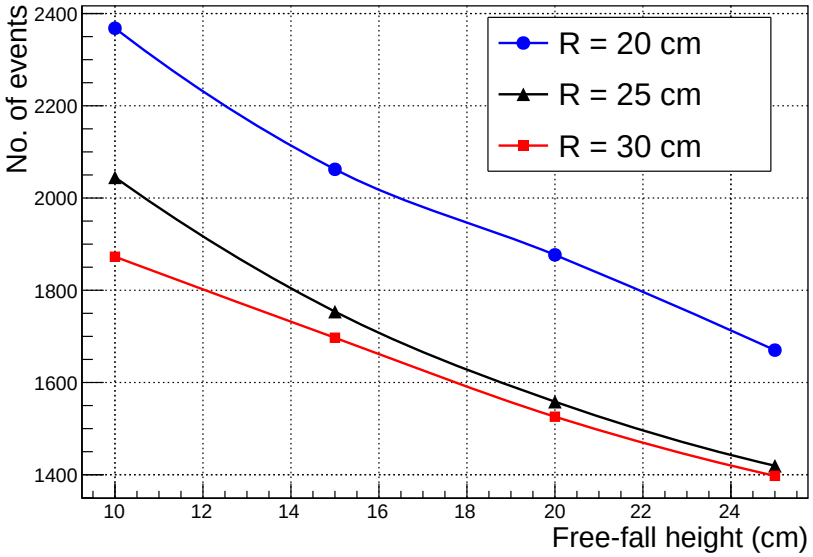

Figure 8.11: Required number of events to reach a relative precision of 1 % for different cylinder radii and free-fall height from simulation

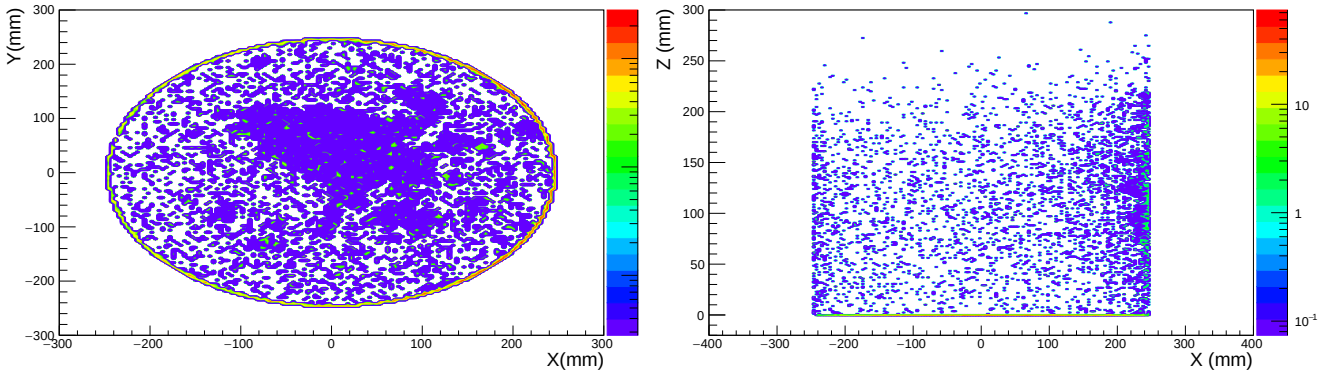

Figure 8.12: Annihilation position on the cylinder in the XY (left) and XZ (right) plane for 25 cm radius and 25 cm free-fall height

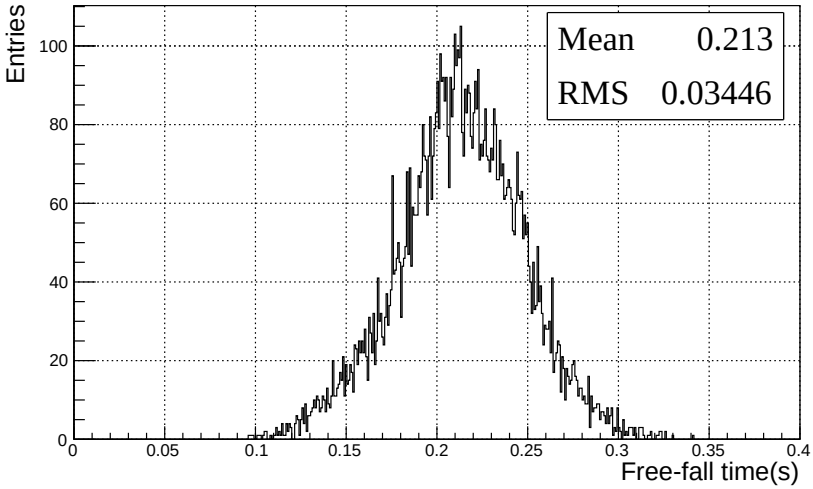

Figure 8.13: Distribution of time of free-fall for a free-fall height of 25 cm, $T = 10\ \mu K$ and $\Delta E = 15\ \mu eV$ for 25 cm radius cylinder

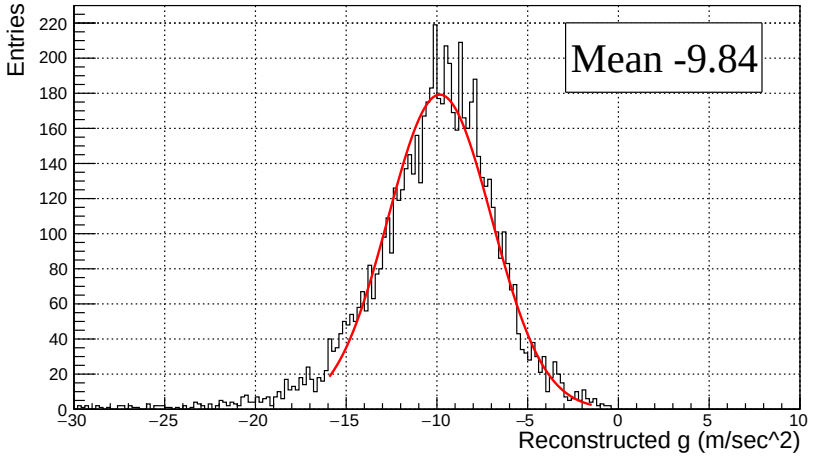

Figure 8.14: Reconstructed $\overline{g}$ for 25 cm radius cylinder and 25 cm free-fall height

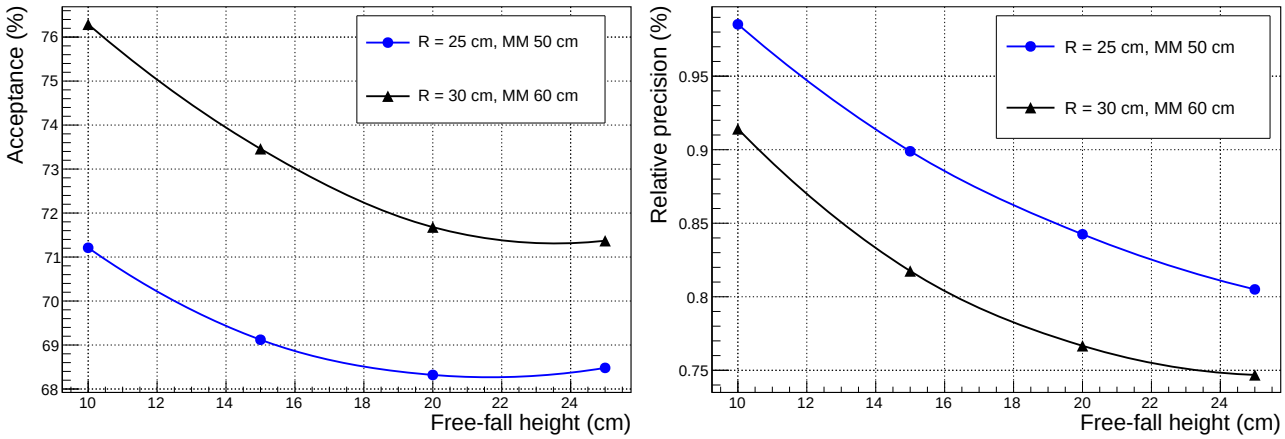

Figure 8.15: Comparison of Acceptance (left) and Relative precision for 1500 detected events (right) as a function of the free-fall height for 30 cm radius cylinder with 60 cm × 60 cm and 25 cm radius cylinder with 50 cm × 50 cm Micromegas modules

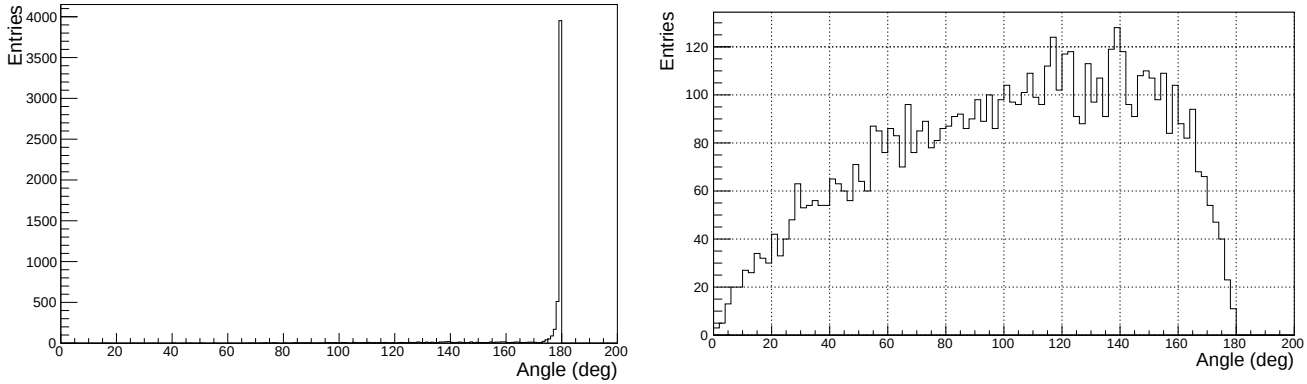

Figure 8.16: Distribution of angle between tracks through different triplets for cosmic events (left) and pion (right) events

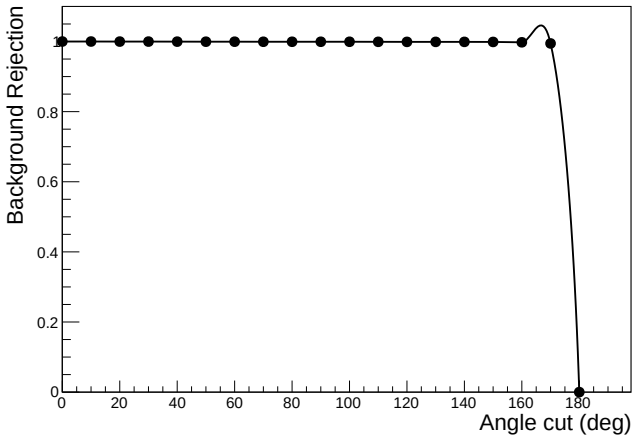

Figure 8.17: Background Rejection as a function of the angle cut

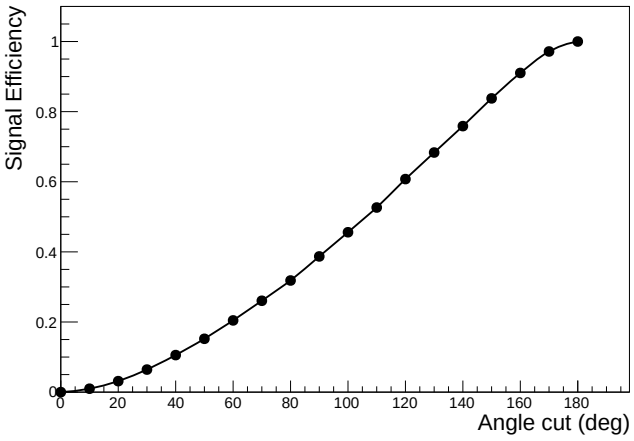

Figure 8.18: Signal efficiency as a function of the angle cut

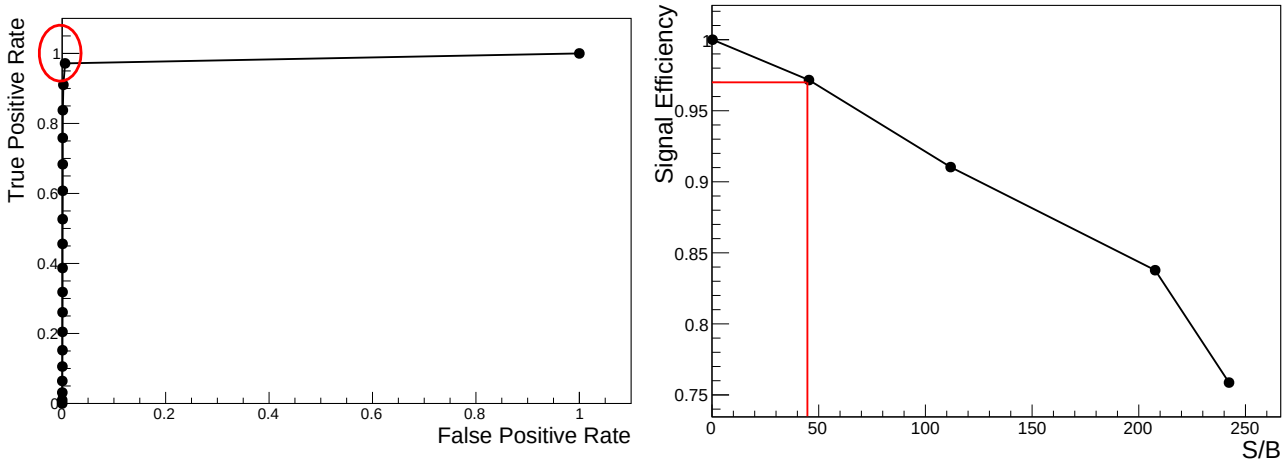

Figure 8.19: ROC curve (left) and Signal Efficiency as a function of the S/B ratio (Right) for different angle cuts. The red circle and lines indicate the case with S/B ∼ 45 for a Signal Efficiency ∼ 97 % for an angle cut < 170° as an example.

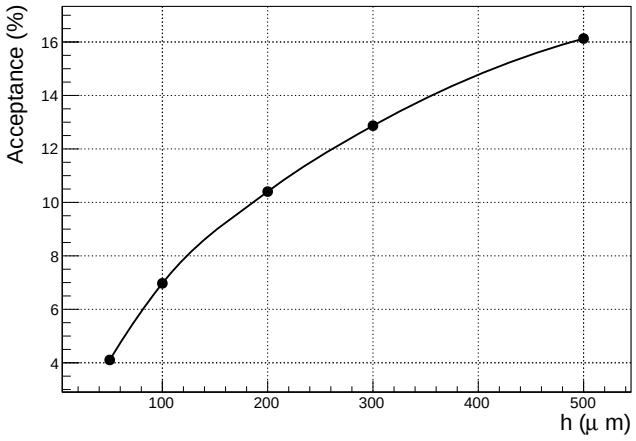

Figure 8.20: Acceptance of events through the shaper as a function of the shaper height h

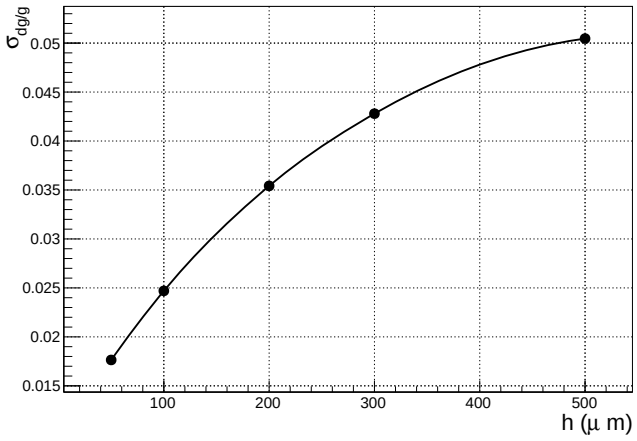

Figure 8.21: $\sigma_{dg/g}$ of atoms through the shaper as a function of the shaper height h

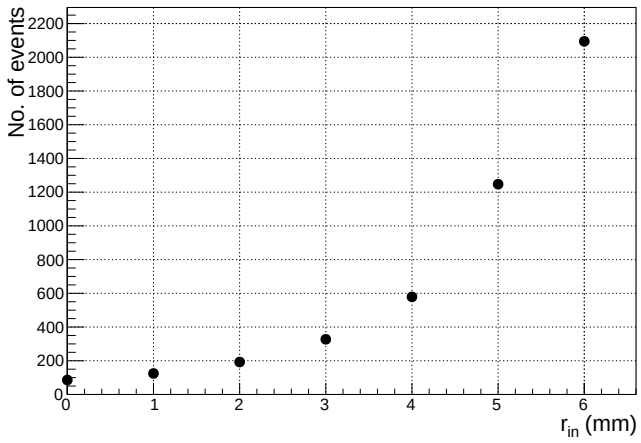

Figure 8.22: No. of events required to reach a relative precision of 1 % as a function of r_{in} with h = 50 μm and r_{out}=25 mm

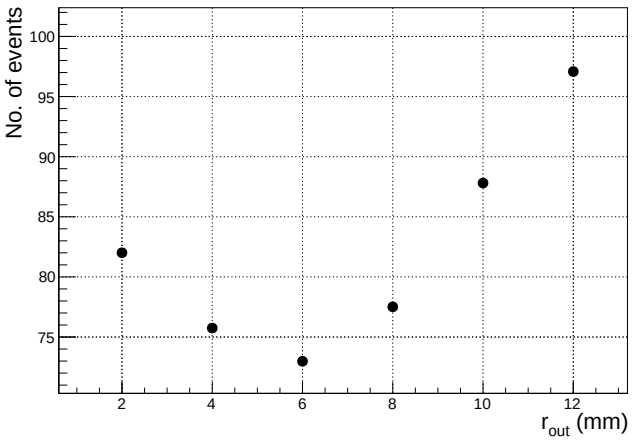

Figure 8.23: No. of events required to reach a relative precision of 1 % as a function of r_{out} with h = 50 μm and r_{in}=1 mm

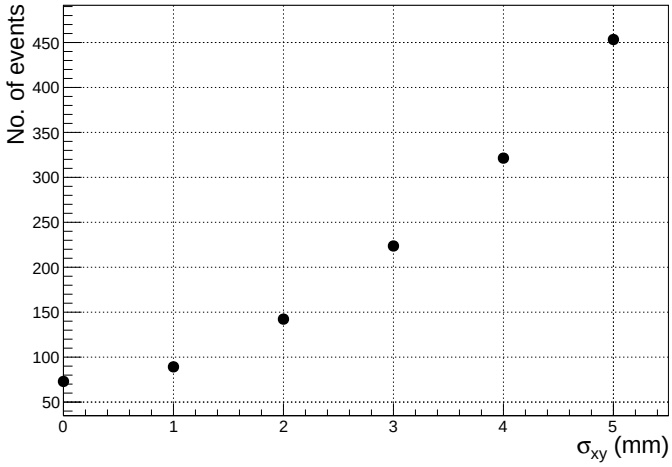

Figure 8.24: No. of events required to reach a relative precision of 1 % as a function of σ_{xy} with h = 50 μm, r_{in}=1 mm and r_{out} = 6 mm

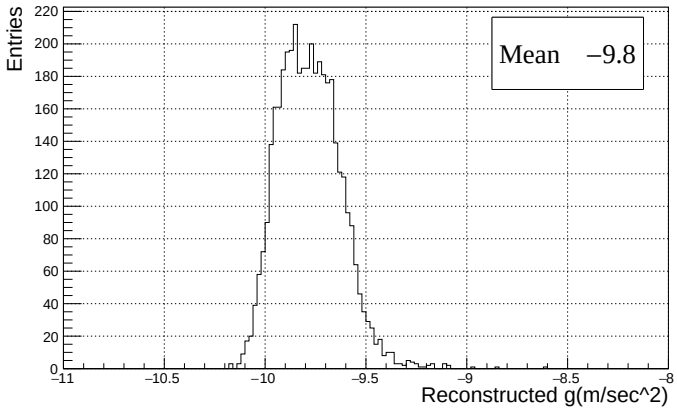

Figure 8.25: Distribution of reconstructed $\overline{g}$ with the shaper

Chapter 9

Summary and Outlook

This thesis presents the NA64 experiment looking for $A' \rightarrow invisible$ decay and the GBAR experiment aiming to measure the gravitational acceleration of anti-hydrogen atoms at rest. Those experiments are setup at the CERN SPS H4 beamline and the CERN AD Hall respectively.

9.1 NA64

The main contribution of the thesis was on the spectrometer that included particle identification with synchrotron radiation detection and incoming momentum reconstruction with the Micromegas modules for NA64. Results of the Geant4 simulation done in the scope of this thesis for Synchrotron Radiation Detection helped establish the possibility of very good e^- identification with the method but it was also proved to be insufficient for energy definition. This led to the proposal of using a spectrometer with Micromegas detectors establishing its performance with Geant4 simulation. Analyzing the synchrotron radiation detection from data and validating the results with Geant4 simulation a suppression factor $< 10^{-3}$ was obtained for pions with the signal efficiency ~ 97 % for electrons. Exploiting the granularity of the BGO SRDs it is also shown that the suppression factor for pions can be improved to $< 10^{-5}$ with the subsequent signal efficiency ~ 95 %. Increasing the granularity of the PbSc SRDs to 6 as opposed to the present case of 3 is under discussion for the next beam time in September' 2017.

Four Multiplexed Resistive XY Micromegas modules used for reconstructing the incoming momentum of the beam showed excellent performance with a momentum resolution ~ 1 % for a 100 GeV/c beam with a combined tracking efficiency ~ 85 %. The first results of such multiplexed modules in a high flux beam performing with an average hit efficiency of 96 % per module for a multiplexing factor of 5 is also presented. Genetically multiplexed detectors are a novel idea to reduce the number of readout channels which prove to be very useful for the present need of particle physics experiments to cover large areas without compromising single hit resolution to perform precise tracking with reduced cost. So far the Multiplexed Resistive XY Micromegas modules have only been tested experimentally using Cosmic ray [151] for muon tomography studies with Micromegas based telescopes. The work of this thesis includes the first report on the performance of these detectors in a high flux beam environment. However, with multiplexing any grouping implies a certain loss of information. This is the reason why ambiguities can occur due to "ghost" signals from fake combinations. Measurements showed that it is indeed possible to limit the ambiguities using information

from cluster size, integrated charge and channel information with < 2 % chance of wrong cluster identification, thus allowing for an efficient and reduced cost tracking detector for high rates in NA64. For further improvement of the tracking efficiency the number of MM stations was doubled for the beam time in September' 2017, i.e. 4 Micromegas was placed before and 4 after the bending magnets. This upgrade should result in an improvement in the overall efficiency to 92 %. Optimizing the collinearity of the beam, which is crucial for NA64, has also been shown to be possible with the Micromegas modules with an angular resolution $\sim$ 0.3 mrad.

The thesis also included participating in the July' 2016 beam run of NA64 and the analysis of the data which is presented. The results set new limits on the A' mixing strength for sub-GeV A' and was able to exclude a large region of the A' favored space for the $(\text{g-2})_\mu$ anomaly with 90 % CL. In the meantime the experiment BABAR also completely excluded the A' favoured parameter space for $(g-2)_\mu$ anomaly [152]. The results also constrain other models favoring interaction of light particles with electrons and decaying predominantly to invisible modes, such as for the light scalar particle, s, with interaction $L_{es} = s\bar{e}(h_s + h_{as}i\gamma_5)e$, the bound on ϵ_s ($\epsilon_s^2\alpha = \frac{h_s^2+h_{as}^2}{4\pi}$), where h_s and h_{as} are, respectively, the scalar and pseudoscalar Yukawa coupling constants of s with e, is approximately 1.5 times weaker than the one obtained on ϵ [123]. In addition to continuing with exploring the parameter space of the $A' \to$ *invisible* decay, in order to exploit the potential of NA64, it also aims to exploit other channels to search for new physics as presented below.

- Electron beam $\to \text{e}^-\text{Z} \to \text{e}^-\text{Z} + A'$, $A' \to \text{e}^+\text{e}^-$, Visible Channel Dark Photon Search. This search probes the visible decay channel of the Dark Matter candidate, A', wherein the produced A' from the scattering of the incoming electron in the target decays predominantly into the e^+ e^- pair as shown in Figure 9.1. The parameter space expected to be covered by this search includes the still unexplored area of mixing strength $10^{-5} < \epsilon < 10^{-3}$ and masses $M_{A'} < 100$ MeV. The signal signature comprises of S1 $\times$ Target $\times$ S2 $\times$ ECAL $\times$ $\overline{\text{V2} \times \text{V3} \times \text{HCAL}}$ with two separated showers in the ECAL of the e^+ e^- pair tracked with trackers.

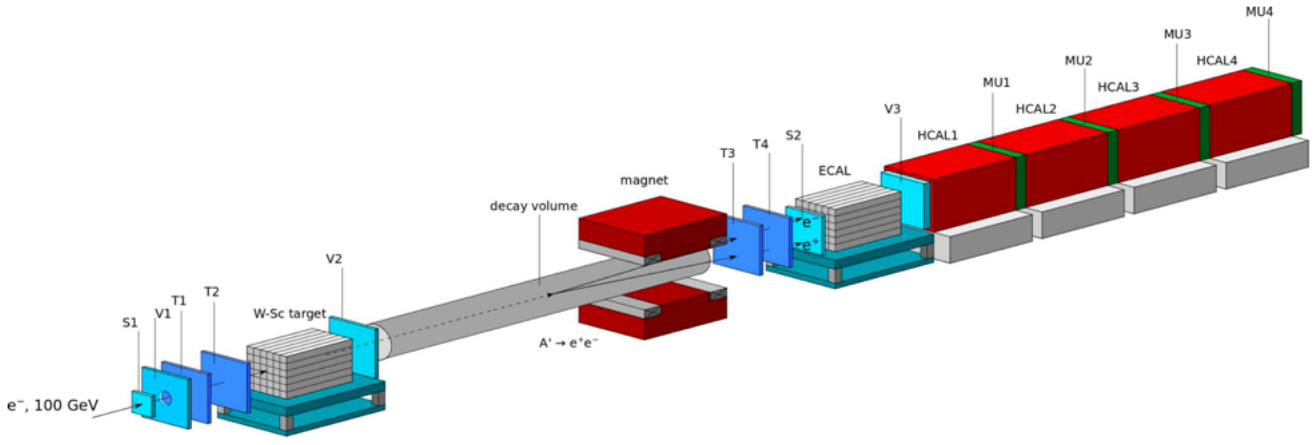

Figure 9.1: Experimental Setup for the A' visible decay channel

- Muon beam $\to \mu^-\text{Z} \to \mu^-\text{Z} + \text{Z}_\mu$, $\text{Z}_\mu \to \nu\nu$, $\mu^+\mu^-$, Leptophobic sub-GeV dark boson. The existence of a new dark boson, Z_μ, with a sub-GeV mass, can explain the $(g-2)_\mu$ anomaly with the 3.6σ discrepancy between its predicted and measured value. This

boson could be searched by NA64 using a high-energy and high-intensity muon beam which is available at the CERN SPS as shown in Figure 9.2. The achievable sensitivity on the coupling constant lies in the range $a_\mu > 10^{-11}$ which is 3 orders of magnitude higher than the required value for the explanation of the discrepancy. The signal signature comprises of an incoming 150 GeV muon beam and a < 100 GeV outgoing muon beam both tracked with trackers with no energy in the ECAL, Veto and HCAL.

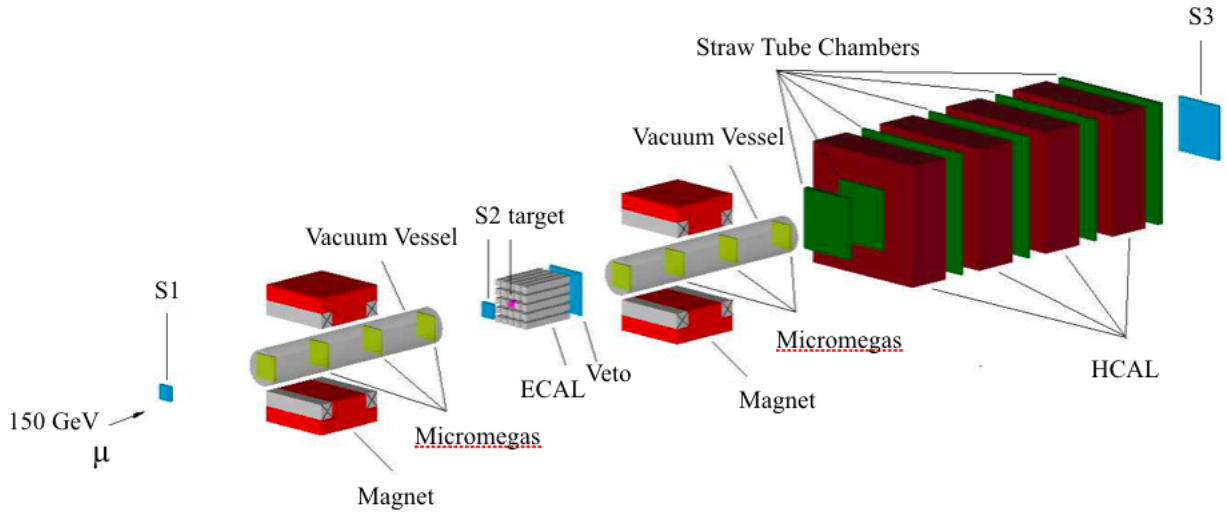

Figure 9.2: Experimental Setup for the Z_μ search with a muon beam.

- Hadron beam $\rightarrow \pi^-$,K^- + p $\rightarrow$ M^0 + n (charge exchange), $M^0 = \pi^0$, η, η', K_L, $K_S \rightarrow$ invisible, Probe of New Physics
  The rate of the above reactions being extremely small as predicted by the Standard Model, its observation would point to new physics. The search aims to use a high energy hadron beam from the CERN SPS as a source of the well tagged M^0 as shown in the reaction with the experimental setup shown in Figure 9.3. The sensitivity achievable on the branching ratio is given by $Br(K_S(K_L) \rightarrow invisible) > 10^{-8}$ (10^{-6}) and that for π^0, η, $\eta' \rightarrow invisible$ decays a few orders of magnitude beyond the present experimental limits. The signal signature comprises of an incoming $\sim$ 50 GeV $K^\pm$ beam tagged with trackers with no energy in the ECAL, Veto and HCAL.

Detailed description of these searches can be found in [153]. The efficient and excellent performance of the Micromegas trackers as presented in this work, which is a requirement for all prospective NA64 measurements present an optimistic step for the future.

9.2 GBAR

The only direct bound obtained on the ratio of the gravitational to inertial mass of antihydrogen was set by ALPHA which constrained it between -65 and 110 [154]. The GBAR experiment aims to reach a 1 % precision on the measurement of $\overline{g}$ in the first phase and potentially improve the precision to $< 10^{-3}$ in a second phase.

One of the contribution of the thesis was studying the tracking of the pion tracks from the $\overline{H}$ annihilation and the subsequent measurement of $\overline{g}$ for GBAR with simulation as well as

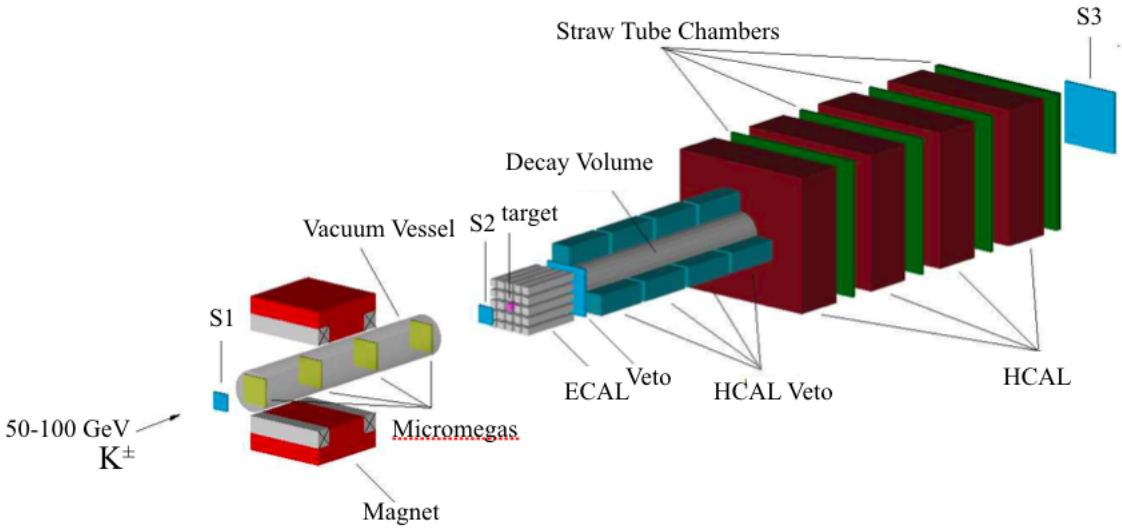

Figure 9.3: Experimental Setup for the $M^0 \rightarrow$ invisible search with a hadron beam, where $M^0 = \pi^0$, η, η', K_L, K_S.

design of the tracker modules. The $\overline{\mathrm{H}}$ annihilation taking into account the initial parameters was simulated with Geant4 to estimate the tracking resolution of the pion tracks with the Micromegas modules and serve as a guide to finalize the free-fall geometry for GBAR. An efficient way to reject cosmic background applying a cut on the reconstructed angle requiring at least two tracks through different triplets/event is also presented. As an example it is shown, for a S/B ratio of 45 the final detection efficiency obtained for an angular cut of $<$ 170° is $\sim$ 67 % with respect to the trapped $\overline{\mathrm{H}}^+$ ions, requiring $\sim$ 1445 trapped $\overline{\mathrm{H}}^+$ ions to reach the aimed relative precision of 1 % on $\overline{g}$ without shaper. Using a thin and short shaper the required number of events can reduce to $\sim$ 103. The required vertex reconstruction resolution for the shaper scheme is $\sigma_{xy} \sim$ a few mm and the obtained resolution on vertex reconstruction is $\sim$ 0.4 mm from simulation. A prototype of a 50 cm $\times$ 50 cm triplet of Micromegas modules is produced and being set up at the GBAR experimental zone in the AD Hall. The triplet will be characterized with radioactive source and its performance will be checked for tracking cosmic events with APV-SRS DAQ. Plans to improve the tracking software by integrating Genfit tracking and vertex reconstruction with the already existing Geant4 simulation package for GBAR is also foreseen. The GBAR is expected to recieve its first $\overline{p}$ in 2018, leading to $\overline{H}$ production and after Long Shut Down 2 in 2018 the free fall experiment is expected to commence.

Acknowledgments

First and foremost I would like to thank Prof. Rubbia for giving me the opportunity to join his group and be a part of such interesting and dynamic experiments. The experience and knowledge I gained in the course of my thesis was extremely valuable and would not have been possible without his support. It motivated me to continue in research and contribute in any way I can. The biggest support during my PhD was Dr. Paolo Crivelli who was always available for any question and discussion no matter how trivial. I was able to take advantage of his experience and knowledge to learn a lot. His constant involvement in the smallest aspects of my research definitely kept me on my toes and helped achieve any results that I did. Another huge contribution in my thesis was from Dr. Sergei Gninenko who was also available for every discussion and never ceased to motivate me for various tasks. His passion for physics and work ethic was inspirational. I would also like to thank Dr. Balint Radics and Dr. David Cooke who never refused to answer my queries and participate in discussions that definitely helped improve my work and skill. Also to my colleague, Emilio Depero, who helped translate my abstract and participated in some interesting conversations. I would like to thank my parents who always encouraged my every endeavor and supported me in everything. This PhD was as much their dream as it was mine. Finally I would like to thank my partner who has been my release during every frustration and stress I faced during this course of time. This definitely would have been much harder without his patience.

Bibliography

[1] R. Oerter (2006) "The Theory of Almost Everything: The Standard Model, the Unsung Triumph of Modern Physics" ISBN 0-13-236678-9.

[2] A. Borriello and P. Salucci, Mon. Not. Roy. Astron. Soc. 323, 285 (2001) astro-ph/0001082.

[3] H. Hoekstra, H. Yee and M. Gladders, New Astron. Rev. 46, 767 (2002) astro-ph/0205205

[4] R. B. Metcalf, L. A. Moustakas, A. J. Bunker and I. R. Parry, Astrophys. J. 607, 43 (2004)

[5] Tracy R. Slatyer, Chih-Liang Wu, General Constraints on Dark Matter Decay from the Cosmic Microwave Background (2016) arXiv:1610.06933

[6] G. Bertone, D. Hooper and J. Silk, Phys. Rept. 405, 279 (2005) hep-ph/0404175.

[7] L Canetti, M Drewes, M Shaposhnikov, Matter and Antimatter in the Universe (2012) arXiv:1204.4186

[8] A Einstein, The Meaning of Relativity (2003) Routledge. p. 59. ISBN 9781134449798.

[9] D Overbye, Cosmos Controversy: The Universe Is Expanding, but How Fast? (20 February 2017) New York Times. Retrieved 21 February 2017

[10] J. L. Feng, Ann. Rev. Astron. Astrophys. 48, 495 (2010) arXiv:1003.0904 astro-ph.CO.

[11] J. Jaeckel and A. Ringwald, Ann. Rev. Nucl. Part. Sci.60, 405 (2010).

[12] J. Alexander et al., arXiv:1608.08632.

[13] N. Arkani-Hamed, D. P. Finkbeiner, T. R. Slatyer, and N. Weiner, A Theory of Dark Matter, Phys.Rev. D79 (2009) 015014, [arXiv:0810.0713].

[14] B. Holdom, Phys. Lett. B 166, 196 (1986).

[15] L. B. Okun, Sov. Phys. JETP 56, 502 (1982) [Zh. Eksp. Teor. Fiz. 83, 892 (1982)].

[16] L. B. Okun, Sov. Phys. JETP 56, 502 (1982) [Zh. Eksp. Teor. Fiz. 83, 892 (1982).

[17] B. Holdom, Phys. Lett. B 166, 196 (1986).

[18] J. Jaeckel and A. Ringwald, Ann. Rev. Nucl. Part. Sci. 60, 405 (2010) arXiv:1002.0329 [hep-ph]

[19] J.L. Hewett et al., arXiv:1205.2671.

[20] J. D. Bjorken, R. Essig, P. Schuster and N. Toro, New Fixed-Target Experiments to Search for Dark Gauge Forces, Phys. Rev. D 80, 075018 (2009)

[21] Y. S. Tsai, Axion Bremsstrahlung By An Electron Beam, Phys. Rev. D 34, 1326 (1986)

[22] J. D. Bjorken, R. Essig, P. Schuster and N. Toro, Phys. Rev. D 80, 075018 (2009) arXiv: 0906.0580 (hep-ph).

[23] S.N. Gninenko, N.V. Krasnikov et al., Missing energy signature from invisible decays of dark photons at the CERN SPS (2016) arXiv:1604.08432

[24] D. Banerjee, V. E. Burtsev, A. G. Chumakov et al., Search for vector mediator of Dark Matter production in invisible decay mode (2017) arXiv:2024778

[25] Mikhail Kirsanov, Sergei Gninenko, NA64 Internal Note on Simulation.

[26] D. Banerjee et al. (NA64 Collaboration), Search for Invisible Decays of Sub-GeV Dark Photons in Missing-Energy Events at the CERN SPS (2017) Phys. Rev. Lett. 118, 011802

[27] G. F. Knoll, Radiation Detection and Measurement. Wyley, 2002. page 235.

[28] Yu. Musienko, private communication.

[29] C. Woody, S. Cheung, J. Haggerty, E. Kistenev and S. Stoll, IEEE Nucl. Sci. Symp. Conf. Rec. 2011, 1471 (2011).

[30] Sergei Gninenko, NA64 HCAL Internal Note

[31] Vladimir Samoylenko, NA64 VETO Internal Note

[32] M. Bodlak, V. Frolov, et al., New data acquisition system for the COMPASS experiment, JINST 8, C02009 (2013).

[33] The APV6 Readout Chip for CMS Microstrip Detectors, M.Raymond et al, Proceedings of 3rd workshop on electronics for LHC experiments, CERN/LHCC/97-60, 158-162.

[34] Performance of a CMOS Mixed Analogue-Digital Circuit (APVD) for the Silicon Tracker of CMS, F.Anstotz et al, Proceedings of 4th workshop on electronics for LHC experiments, CERN/LHCC/98-36, 180-184.

[35] `http://sba.web.cern.ch/sba/` and `http://nahandbook.web.cern.ch/`

[36] C. Berneta, A. Bravara, et al., The COMPASS trigger system for muon scattering (2005) Nuclear Instruments and Methods in Physics Research A 550 217240

[37] S. Andreas, D. Banerjee, S.V. Donskov, P. Crivelli, A. Gardikiotis, S.N. Gninenko, F. Guber et al., Proposal for an Experiment to Search for Light Dark Matter at the SPS (2013), arXiV:1312.3309

[38] E. Depero, D. Banerjee et al, High purity 100 GeV electron identification with synchrotron radiation (2017) arXiv:1703.05993

[39] D. Banerjee, P. Crivelli, and A. Rubbia, Beam Purity for Light Dark Matter Search in Beam Dump Experiment, Adv. High Energy Phys. (2015) 105730

[40] Scherk J Antigravity: a crazy idea? (1979) Phys. Lett. B 88 265

[41] Nieto M M and Goldman T, The arguments against antigravity and the gravitational acceleration of antimatter (1991) Phys. Rep. 205 221

[42] Gabrielse G et al 1999 Precision mass spectroscopy of the antiproton and proton using simultaneously trapped particles Phys. Rev. Lett. 82 3198

[43] Kostelecky V A and Tasson J D Matter-gravity couplings and Lorentz violation (2011) Phys. Rev. D 83 016013

[44] Benoit-Levy A and Chardin G, Introducing the DiracMilne universe Astron. Astrophys. 537 A78 (2012)

[45] CP LEAR Collaboration 1999 Tests of the equivalence principle with neutral kaons Phys. Lett. B 452 425

[46] Nieto M M and Goldman T, The arguments against antigravity and the gravitational acceleration of antimatter (1991) Phys. Rep. 205 221

[47] Mills A P and Leventhal M 2002 Can we measure the gravitational free fall of cold Rydberg state positronium? Nucl. Instrum. Methods Phys. Res. B 192 102

[48] GBAR collaboration, CERN-SPSC-2011-029. SPSC-P-342, CERN (2011).

[49] Laser cooling and trapping of neutral atoms Nobel Lecture by William D. Phillips (1997) RevModPhys.70.721

[50] A. Yu. Voronin, V.V. Nesvizhevsky, G. Dufour, P. Debu, A. Lambrecht, S. Reynaud, O.D. Dalkarov, E.A. Kupriyanova, P.Froelich, Int. J. Mod. Phys. Conf. Ser. 30, 1460266 (2014)

[51] Walz J and Hänsch T, A proposal to measure antimatter gravity using ultracold antihydrogen atoms Gen. Rel. Grav. 36 561 (2004)

[52] Pérez P and Rosowsky A, A new path toward gravity experiments with antihydrogen Nucl. Instrum. Methods Phys. Res. A 545 20 (2005)

[53] Merrison J P et al, Hydrogen formation by proton impact on positronium Phys. Rev. Lett. 78 2728 (1997)

[54] Mitroy J, Formation of antihydrogen by the charge-transfer reaction Phys. Rev. A 52 2859 (1995)

[55] P. Comini, P. Antoine-Hervieux, $\overline{H}^+$ production from collisions between positronium and keV antiprotons for GBAR. Hyperfine Int (2014) 228:159-165

[56] Nesvizhevsky V V et al, Quantum states of neutrons in the Earths gravitational field Nature 415 297 (2002)

[57] Voronin A Y, Froelich P and Nesvizhevsky V V, Gravitational quantum states of antihydrogen Phys. Rev. A 83 032903 (2011)

[58] N. Sillitoe, L. Hilico et al., $\overline{\mathrm{H}}^+$ Sympathetic Cooling Simulations with a Variable Time Step, arXiv:1705.03347v2 (2016)

[59] G. Dufour, P. Debu, A. Lambrecht, V.V. Nesvizhevsky, S. Reynaud, A. Yu. Voronin Eur. Phys. J. C74, 2731 (2014).

[60] V. V. Nesvizhevsky et al., Nature 415, 297 (2002); V. V. Nesvizhevsky, A. Y. Voronin. R. Cubitt, K. V. Protasov, Nature Physics 6(2), 114 (2010).

[61] G. Dufour, A. Grardin, et al., Phys. Rev. A 87(1), 012901 (2013).

[62] A.Walther, F. Ziesel, et al., Phys.Rev.Lett. 109(8), 080501 (2012).

[63] G. Dufour, A. Gerardin et al., Quantum reflection of antihydrogen from the Casimir potential above matter slabs. (2012) arXiv:1212.5676v1

[64] Berta Beltran et al, Search for solar axions: the CAST experiment at CERN, Nucl. Instr. and Meth. in Phys. Res. B 197 (2005) 62-65

[65] Y. Giomataris, Ph. Rebourgeard, J.P. Robert, G. Charpak, Nucl. Instr. and Meth. in Phys. Res. A 376 (1996) 29 - 35.

[66] COMPASS Collaboration, COMPASS Experiment at CERN, Nucl. Instr. and Meth. in Phys. Res. A 577 (2007) 455-518

[67] Charles, Gabriel, Development of Micromegas detectors for the CLAS12 experiment at Jefferson Laboratory, (Sep 2013) (FRCEA-TH–5915)

[68] F J Iguaz, D Attie, D Calvet et al, Micromegas detector developments for Dark Matter directional detection with MIMAC, Journal of Instrumentation, Volume 6 (July 2011)

[69] A. Peyaud, A. Angelopoulos, C. Chelmis et al, The ForFire photodetector, Nucl. Instr. and Meth. in Phys. Res A 787 (2015) 102 - 104

[70] Maxim Titov, Perspectives of Micro-Pattern Gaseous Detector Technologies for Future Physics Projects, (2013) arXiv:1308.3047

[71] F. Sauli, M. Titov et al., "Review of Particle Physics" (Particle Data Group), Chapters 28.7.1-28.7.3 "Gaseous Detectors" Phys. Lett. B 667, 292 (2008).

[72] W.B Jensen, Electronegativity from Avogadro to Pauling: Part 1: Origins of the Electronegativity Concept. (1996) Journal of Chemical Education. 73 (1): 1120.

[73] A. L. Hughes and J. H. McMillen, Inelastic and Elastic Electron Scattering in Argon (1932) Phys. Rev. 39, 585

[74] A.J.P.L. Policarpo, Physica Scripta 23 (1981) 539.

[75] Handbook of Chemistry and Physics, R.C.Weast (C.R.C. Press, Bica Raton, Fl. (1981) 205.

[76] M. Suzuki and S. Kubota, Nucl. Instr. and Meth. A 164 (1979) 197.

[77] R.I. Schoen, J. Chem. Phys. 17 (1962) 2032.

[78] Yu.N. Pestov et al., Nucl. Instr. and Meth. A 456 (2000) 11.

[79] B.D. Ramsey and P.C. Agrawal, Nucl. Instr. and Meth. A 273 (1988) 326.

[80] B.D. Ramsey and P.C. Agrawal, Nucl. Instr. and Meth. A 273 (1988) 331.

[81] Biagi SF (1999) Monte Carlo simulation of electron drift and diffusion in counting gases under the influence of electric and magnetic fields. Nucl Instrum Methods A 421(12): 234240.

[82] H. Raether, Z. Phys. 112 (1939) 464

[83] M.S. Dixit and A. Rankin, Simulating the charge dispersion phenomena in micro pattern gas detectors with a resistive anode, Nucl. Instrum. Meth. A566 (2006) 281

[84] J.Burnens et al., A sparkresistant bulkmicromegas chamber for highrate applications, CERNPH EP2010061 (2010)

[85] Guillaume Cauvin, A study of MicroMegas detectors with resistive anodes for muon reconstruction in HL -LHC, Master Thesis, Royal Institute of Technology, Sweden, 2012

[86] S. Procureur, R. Dupre, S. Aune, Genetic Multiplexing and first results with a 50 $\times$ 50 cm^2 Micromegas, Nucl. Instr. and Meth. in Phys. Res. A 729 (2013) 888-894

[87] P.Abbon, et al., Nuclear Instruments and Methods in Physics Research Section A 577(2007)455.

[88] Xiaoguang Yue, Ming Zeng, et al., Mathematical modelling and study of the encoding readout scheme for position sensitive detectors (2015) arXiv:1508.03704v2

[89] QI Bin-Xiang LIU Shu-Bin et al, A Novel Method of Encoded Multiplexing Readout for Micro-pattern Gas Detectors (2015) arXiv: 1509.02229

[90] M. Byszewski and J. Wotschack, Resistive-strips micromegas detectors with two-dimensional readout, (2012) JINST 7 C02060

[91] G. Iakovidis, The Micromegas project for the ATLAS upgrade, (2013) JINST 8 C12007.

[92] M. J. French, L. L. Jones et al, Design and results from the APV25, a deep sub-micron CMOS front-end chip for the CMS tracker, Nucl. Instr. and Meth. in Phys. Res. A- 466 (2001) 359-365

[93] B. Ketzer, S. Bachmann et al, GEM Detectors for COMPASS, (2001) IEEE TRANSACTIONS ON NUCLEAR SCIENCE, VOL. 48, NO. 4

[94] B. Grube, The Trigger Control System and the Common GEM and Silicon Readout for the COMPASS Experiment, Diploma thesis, Munchen, December 2001.

[95] H. Fischer et al., The COMPASS Online Data Format, COMPASS Note 2001-8, Freiburg, 2001.

[96] O. Bowle et al., The S-Link Interface Specifications, http://www.cern.ch/HSI/s-link/, ECP Division, CERN, 1997.

[97] M. Golubeva, F. Guber, et al., Nucl. Instrum. Meth. A 598, 268 (2009). A. Ivashkin, F. Akhmadov, et al., arXiv:1205.4864 [physics.ins-det].

[98] NA64 Collaboration. To be published

[99] H. Wiedemann, Synchrotron Radiation, Springer-Verlag Berlin Heidelberg, 2003.

[100] K. A. Olive et al. (PDG), Passage of particles through matter Chin. Phys. C38 (2014) .

[101] E. Depero, Synchrotron tagging using BGO detector for experiment NA64, Master Thesis, ETH Zurich, (2016)

[102] C. Höppner, S. Neubert, B. Ketzer et al., Nucl. Instr. and Meth. in Phys. Res. A 620 (2010) 518 - 525

[103] Methods of Experimental Physics Volume 5 Part A, Nuclear Physics, Page 93

[104] Maxim Titov, Gaseous Detectors: recent developments and applications (2010) arXiv: 1008.3736

[105] A. Bressan , M. Hoch , P. Pagano et al, High rate behavior and discharge limits in micro-pattern detectors, Nucl. Instr. and Meth. in Phys. Res. A 424 (1999) 321-342

[106] P Fonte, V Peskov, On the physics and technology of gaseous particle detectors, arxiv: 0909.2681

[107] `https://wwwcompass.cern.ch/compass/detector/daq/status/daqdoc.html`

[108] G. A. Akopdzhanov et al., Determination of Photon Coordinates in Hodoscope Cherenkov Spectrometer Nucl. Instrum. Meth. 140 (1977) 441.

[109] V. A. Davydov, A. V. Inyakin et al., Particle Identification in Hodoscope Cherenkov Spectrometer, Nucl. Instrum. Meth. 145 (1977) 267.

[110] D.Autiero et al. "A study of the transverse fluctuations of hadronic showers in the NOMAD electromagnetic calorimeter", Nucl. Instrum. Meth. A 411 (1998) 285

[111] S.N. Gninenko "A study of the transverse fluctuations of hadronic showers in the NOMAD electromagnetic calorimeter" Nucl. Instrum. Meth. A 409 (1998), 583.

[112] E. Izaguirre, G. Krnjaic, P. Schuster and N. Toro, Testing GeV-Scale Dark Matter with Fixed-Target Missing Momentum Experiments, Phys. Rev. D 91, no. 9, 094026 (2015).

[113] B. Aubert et al. (BaBar Collaboration), Search for Invisible Decays of a Light Scalar in Radiative Transitions $v_{3S} \to \gamma A0$ arXiv:0808.0017 (hep-ex)

[114] A. V. Artamonov et al. (BNL-E949 Collaboration), Study of the decay $K^+ \to \pi^+ \nu\overline{\nu}$ in the momentum region 140 ¡ P(π) ¡ 199 MeV/c, Phys. Rev. D 79 (2009) 092004.

[115] H. S. Lee, Muon g-2 anomaly and dark leptonic gauge boson, Phys. Rev. D 90 (2014) 9, 091702.

[116] H. Davoudiasl, H. S. Lee and W. J. Marciano, Muon (g-2), rare kaon decays, and parity violation from dark bosons, Phys. Rev. D 89 (2014) 9, 095006.

[117] B. Batell, M. Pospelov and A. Ritz, Exploring Portals to a Hidden Sector Through Fixed Targets, Phys. Rev. D 80 (2009) 095024.

[118] P. deNiverville, M. Pospelov and A. Ritz, Observing a light dark matter beam with neutrino experiments, Phys. Rev. D 84 (2011) 075020

[119] R. Essig et al., Working Group Report: New Light Weakly Coupled Particles, arXiv:1311.0029 (hep-ph).

[120] M. Raggi and V. Kozhuharov, Results and perspectives in dark photon physics, Riv. Nuovo Cim. 38 449, (2015).

[121] S. N. Gninenko, Search for MeV dark photons in a light-shining-through-walls experiment at CERN, Phys. Rev. D 89 (2014) 7, 075008

[122] S. Andreas et al., Proposal for an Experiment to Search for Light Dark Matter at the SPS, arXiv:1312.3309 (hep-ex)

[123] NA64 collaboration. Paper in preparation.

[124] Q. Weitzel. Triple GEM detectors in COMPASS - a performance study. Diploma thesis, Technische Universität München, November 2003.

[125] Y. Kataoka et al., Performance studies of a micromegas chamber in the ATLAS environment, 2014 JINST 9 C03016.

[126] S. Agostinelli et al. (GEANT4 Collaboration), Nucl. Instrum. Meth. A 506, 250 (2003). J. Allison, K. Amako, et al., IEEE Trans. Nucl. Sci. 53, 270 (2006).

[127] M Amoretti, et al. Production and detection of cold antihydrogen atoms. Nature. 419 (6906): 4569. (2002)

[128] G Gabrielse et al. Driven Production of Cold Antihydrogen and the First Measured Distribution of Antihydrogen States. Phys. Rev. Lett. 89 (23) 233401. (2002)

[129] L. Hilico, J.-P. Karr, A. Douillet, P. Indelicato, S. Wolf and F. Schmidt Kaler, International Journal of Modern Physics, Conference Series 30, 1460269 (2014).

[130] S. Maury W. Bartmann, P. Belochitskii, et al., Progress in ELENA Design, IPAC13, Shanghai, China, May 2013, p.2651.

[131] P. Comini and P-A. Hervieux, $\overline{\mathrm{H}}^{+}$ ion production from collisions between antiprotons and excited positronium Cross section calculations in the framework of the GBAR experiment, New J. Phys., 15, 095022 (2013)

[132] http://isolde.web.cern.ch

[133] P. Perez, D. Banerjee et al. The GBAR antimatter gravity experiment Hyperfine Interactions 233(1):21-27 April 2015

[134] D. B. Cassidy et al., Positronium Cooling in Porous Silica Measured via Doppler Spectroscopy, Phys. Rev. A, 81, 012715 (2010); P. Crivelli et al., Measurement of the orthopositronium confinement energy in mesoporous thin films, Phys. Rev. A, 81, 052703 (2010).

[135] P. Crivelli et al., Experimental considerations for testing antimatter antigravity using positronium 1S-2S spectroscopy, Int. J. Mod. Phys. Conf. Ser., 30, 1460257 (2014)

[136] Pauline Comini, PhD thesis, Universite Paris 6

[137] D.A. Cooke, P. Crivelli et al., Observation of positronium annihilation in the 2S state: towards a new measurement of the 1S-2S transition frequency, Hyperfine Interactions, 2015, Volume 233, Number 1-3, Page 67

[138] N. Oshima et al., New Scheme for Positron Accumulation in Ultrahigh Vacuum, Phys. Rev. Lett. 93, 195001 (2004)

[139] P. Grandemange et al., First results of a new positron-accumulation scheme using an electron linac and a Penning-Malmberg trap, J. Phys.: Conf. Ser., 505, 012035 (2014)

[140] L. Hilico et al., Preparing single ultra-cold antihydrogen atoms for the free-fall in GBAR, Int. J. Mod. Phys: Conf. Ser., 30, 1460269 (2014)

[141] https://edms.cern.ch/ui/file/1453950/

[142] Material Data Book (2003), Cambridge University Engineering Department

[143] T. von Egidy et al., Z. Phys. A 335, 451 (1990).

[144] P. Hofmann et al., Phys. Rev. C 49, 2555 (1994).

[145] C. Amsler et al., The CRYSTAL BARREL Collaboration, Antiproton - proton annihilation at rest into two-body final states. Zeit. f. Physik C58, 175, (1993), CERN-PPE/93-11

[146] http://atlas.physics.arizona.edu/kjohns/downloads/atlas-micromegas/srs-software-docs/

[147] C. Hagmann, D. Lange, J. Verbeke, and D. Wright, Cosmic-ray Shower Library (CRY), Tech. Rep. UCRL-TM-229453 (Lawrence Livermore National Laboratory, 2013)

[148] S. Martoiu et al., Front-end electronics for the scalable readout system of RD51, in 2011 IEEE Nucl. Sci. Symp. Conf. Record N43-5, 20362038, (2011).

[149] S. Martoiu et al., JINST 8, C03015 (2013).

[150] J. Toledo et al., JINST 6, C11028 (2011).

[151] S. Bouteille, D. Attie, P. Baron, D. Calvet, P. Magnier, et al., A Micromegas-based telescope for muon tomography, Nucl. Instr. and Meth. in Phys. Res. A: (2016) 834 223 - 228.

[152] BaBar Collaboration, Search for invisible decays of a dark photon produced in e^+ e^- collisions at BaBar, arXiv:1702.03327

[153] `http://na64.web.cern.ch/`

[154] C. Amole et al., Description And First Application Of A New Technique To Measure The Gravitational Mass Of Antihydrogen, Nature Communications 4, 1785 (2013)